

Sheffield Hallam University

A molecular dynamics study of liquid crystal mixtures.

BEMROSE, Richard Anthony.

Available from the Sheffield Hallam University Research Archive (SHURA) at:

<http://shura.shu.ac.uk/19339/>

A Sheffield Hallam University thesis

This thesis is protected by copyright which belongs to the author.

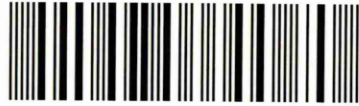
The content must not be changed in any way or sold commercially in any format or medium without the formal permission of the author.

When referring to this work, full bibliographic details including the author, title, awarding institution and date of the thesis must be given.

Please visit <http://shura.shu.ac.uk/19339/> and <http://shura.shu.ac.uk/information.html> for further details about copyright and re-use permissions.

LEARNERS' LIBRARY
CITY CAMPUS, POND STREET,
SHEFFIELD, S1 1WB.

101 617 345 8



REFERENCE

ProQuest Number: 10694220

All rights reserved

INFORMATION TO ALL USERS

The quality of this reproduction is dependent upon the quality of the copy submitted.

In the unlikely event that the author did not send a complete manuscript and there are missing pages, these will be noted. Also, if material had to be removed, a note will indicate the deletion.



ProQuest 10694220

Published by ProQuest LLC (2017). Copyright of the Dissertation is held by the Author.

All rights reserved.

This work is protected against unauthorized copying under Title 17, United States Code
Microform Edition © ProQuest LLC.

ProQuest LLC.
789 East Eisenhower Parkway
P.O. Box 1346
Ann Arbor, MI 48106 – 1346

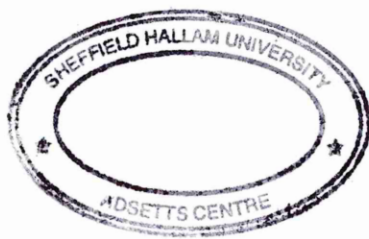
A MOLECULAR DYNAMICS STUDY OF LIQUID CRYSTAL MIXTURES

RICHARD ANTONY BEMROSE, BSc (Hons.), Grad. Inst. Phys.

A thesis submitted in partial fulfilment of the requirements
of Sheffield Hallam University for the degree of
Doctor of Philosophy

5 December, 1999

Materials Research Institute, Sheffield Hallam University
in collaboration with the
Defence Evaluation Research Agency, Malvern Laboratory.



Abstract

Results are presented from molecular dynamics simulations of binary liquid crystal mixtures using a generalisation of a well established Gay-Berne intermolecular potential. The simulations are undertaken in both the microcanonical (*NVE*) and the isoenthalpic-isobaric (*NPH*) ensembles.

Firstly a 50:50 mixed system is simulated in the *NVE* ensemble containing generalised Gay-Berne (GGB) rod-like molecules with length to breadth axial ratios of 3.5:1 (molecules *A*) and 3:1 (molecules *B*). The molecules in this system differs only slightly from the well-characterised Gay-Berne (GB) potential with length to breadth ratio of 3:1. It is shown that the system exhibits isotropic (*I*), nematic (*N*) and smectic-B (*SmB*) phases with both the *I-N* and *N-SmB* phase boundaries not clearly defined. Competition between two density waves parallel to the director of the same wavelength but different phase lead to a pre-smectic ordering preceding the *N-SmB* phase transition. The longer molecules are shown to have a consistently higher order parameter the difference being greatest in the nematic phase and decrease with lowering temperature. Although a degree of local ordering is shown within each smectic layer the smectic phase is fully commensurate.

Secondly, phase behaviour diagrams are presented from a series of constant-*NPH* simulations over a range of pressures and concentrations. The binary mixtures exhibit a rich phase behaviour, displaying isotropic, nematic, smectic-A (*SmA*), *induced SmA* and smectic-B phases depending on the choice of pressure and concentration. It is shown that the temperature range over which the nematic phase is stable can be extended greater than either homogeneous system by elevating the system pressure and/or by choice of concentration, agreeing with experimental results. The mixture exhibits a stable *SmA island* at a mole fraction of $\chi_A = 0.50$ depending on the choice of pressure and a narrow *induced SmA* phase at $\chi_A = 0.25$.

*To my family
and loving memory of my Nan*

If you can talk with crowds and keep your virtue,
Or walk with kings - nor lose the common touch;
If neither foes nor loving friends can hurt you;
If all men count with you, but none too much;
If you can fill the unforgiving minute
With sixty seconds' worth of distance run -
Yours is the Earth and everything that's in it,
And - which is more - you'll be a Man, my son!

Excerpt from “*If*” by Rudyard Kipling (1865–1936)

Acknowledgements

I would like to thank my supervisors, Prof. C.M. Care, Dr. M.P. Neal and Dr. D.J. Cleaver for their invaluable guidance and encouragement throughout my studies. Furthermore, I also wish to acknowledge EPSRC and DERA (Malvern Laboratory) for their financial support.

I would like to thank all those people past and present in and around MRI's modelling laboratory for their friendship and many enjoyable conversation (some of them heated). Thanks to Ade, Dom, Leila, Mike, JC, Declan, Martin, Steve, Stu, Daz, Tom, Ian, Alain and all the staff who had to put up with me.

I would like to thank Dr. J.R. Melrose of the Polymers and Colloids Group, Cavendish Laboratory, University of Cambridge for a great deal of understanding and extensive use of the groups computational resources while I was in limbo.

Finally, I want to especially thank my family for their unreserved and constant moral support without whom I would not have achieved all that I have today.

Advanced Studies

As part of the course of study a number of postgraduate courses held by the MRI at Sheffield Hallam University were attended. A number of external courses and conferences were attended, along with an invited talk.

- Introduction to Liquid Crystals, University of Leeds (Oct 1993)
- CCP5 Spring School, University of Southampton (March 1994)
- BLCS Annual Meeting, University of Hull (April 1994)
- BLCS Annual Meeting, University of Exeter (April 1995)
- MPI Parallel Programming Workshop, Edinburgh Parallel Computer Centre, University of Edinburgh (August 1995)
- BLCS Annual Meeting, University of Central Lancashire (April 1996)
- 16th International Liquid Crystal Conference, Ohio State University, Ohio, USA (June 1996)
- Invited Talk, Max Plank Institute for Polymer Research, Mainz, Germany (March 1997) – “Phase Behaviour and Structural Properties of Liquid Crystal Mixtures”

The following publications has also arisen as part of this work.

- Bemrose RA, Care CM, Neal MP, Cleaver DJ, “A Molecular Dynamics study of a Bi-disperse Liquid Crystal Mixture using a Generalized Gay-Berne Potential”, *Molecular Physics*, 90(4):625, 1997
- Bemrose RA, Care CM, Neal MP, Cleaver DJ, “Computer Simulation of Bi-disperse Liquid Crystals: The effect of Concentration on Phase Behaviour and Structural Properties”, *Molecular Crystals and Liquid Crystals*, 299:27, 1997

Contents

List of Figures	vii
List of Tables	xi
1 Introduction	1
1.1 A brief history	1
1.2 Classification of liquid crystals	2
1.3 Mixtures of Liquid Crystals	4
1.4 The Role of Computer Simulations	5
1.5 Aims	5
1.6 Layout of Thesis	7
2 Literature review	9
2.1 Experimental	9
2.2 Theoretical	14
2.3 Simulation	22
3 Modelling Liquid Crystals	27
3.1 Molecular Dynamics	27
3.1.1 Equation of motion	27
3.1.2 Verlet algorithm	30
3.1.3 Isoenthalpic-Isobaric ensemble, constant- <i>NPH</i>	34
3.2 Generalised Gay-Berne intermolecular potential	37
3.2.1 GGB parameterisation	39
3.2.2 Evaluating separations	41
3.2.3 Determination of L_A^{LJ} and L_B^{LJ}	43
3.2.4 Least squares fit.	44
3.3 Periodic boundary conditions	45
3.4 Order parameters and structural properties	47
3.4.1 Orientational order parameter	47
3.4.2 Pair distribution functions	48
3.4.3 Bond orientational order parameter	49
3.4.4 Orientational correlation function	51

4 Length dispersity study	52
4.1 Introduction	52
4.2 Simulation details	54
4.3 Results and analysis	55
4.4 Conclusions	69
5 Concentration and pressure study	71
5.1 Introduction	71
5.2 Influence of pressure	72
5.2.1 Simulation details	73
5.2.2 Onset of orientational order, T_{I-N}	74
5.2.3 Higher ordered phase and metastability, T_{N-Sm}	77
5.2.4 Phase behaviour diagrams	89
5.2.5 Summary	92
5.3 Influence of concentration	92
5.3.1 Simulation details	95
5.3.2 Results and analysis	95
5.3.3 Comparison of homogeneous 3:1 simulation to literature	98
5.3.4 Concentration dependency on T_{I-N}	99
5.3.5 Postponement of Smectic Phases and Layer Spacing	102
5.3.6 Induced <i>SmA</i> Phase for $\chi_A = 0.25$ simulation	106
5.3.7 Extended Nematic Range	108
5.3.8 Summary	110
5.4 Concluding Remarks	112
6 Conclusions and Future Work	114
6.1 Concluding remarks	114
6.2 Final Remarks and Future work	116
References	118
A Appendix of Section 5.2 of Chapter 5	128
A.1 $\langle P^* \rangle = 1.0$	129
A.2 $\langle P^* \rangle = 2.0$	130
A.3 $\langle P^* \rangle = 3.0$	131
A.4 $\langle P^* \rangle = 4.0$	132
A.5 $\langle P^* \rangle = 5.0$	133
B Appendix of Section 5.3 of Chapter 5	134
B.1 $\chi_A = 0.0$	135
B.2 $\chi_A = 0.25$	136
B.3 $\chi_A = 0.5$	137
B.4 $\chi_A = 0.75$	138
B.5 $\chi_A = 1.0$	139

List of Figures

1.1	Schematics of some calamitic and discotic liquid crystals: a) crystal, b) nematic, c) isotropic, d) smectic- <i>A</i> , e) smectic- <i>B</i> , f) smectic- <i>C</i> , g) cholesteric, h) discotic columnar and i) discotic nematic [10, 11].	3
1.2	The role of computer simulations as described by [15].	6
2.1	Phase diagram for binary mixture of <i>8OCB</i> and <i>ODOBAF</i> [30].	11
2.2	Phase diagram for binary mixture of DB8NO ₂ and DB10NO ₂ [31].	12
2.3	<i>a)</i> Phase diagram for binary mixture of a polar molecule and non-polar molecule. <i>b)</i> Layer spacing as a function of composition at constant temperature of slightly above T_C [43].	15
2.4	Predicted phase diagram for cylindrically symmetrical rod/disk-like mixture from Stroobants and Lekkerkerker [52] extension of Onsager theory.	18
2.5	Palffy-Muhoray <i>et al</i> [53] mean-field theory predicted <i>a)</i> phase diagram and <i>b)</i> free energy for rod/disk mixture.	19
2.6	Gaussian approximate (Onsager) predicted pressure (Π) <i>vs.</i> concentration phase diagram [55] of bi-disperse system for $L_A/L_B = 2$ (left) and $L_A/L_B = 5$ (right). Dotted line represents the difference in mole fractions.	21
2.7	Constant pressure phase diagrams of associating cylindrical molecules [39]. Pressure is reduced from top to bottom diagrams.	22
2.8	Phase behaviour of a binary mixture of hard parallel spherocylinders as a function of L_2/D	24
3.1	Simplification process of ethylbenzene: centre) electron cloud density representation, bottom) ethylbenzene model representation [79]	32
3.2	Interaction between two non-identical anisotropic particles.	38
3.3	Tee configuration of infinite Lennard-Jones and semi-infinite jellium lines.	41
3.4	Cross configuration of two infinite Lennard-Jones jellium lines.	42
3.5	Generalised Gay-Berne intermolecular potential between two non-identical anisotropic particles 3.5:1 (molecules <i>A</i>) and 3:1 (molecules <i>B</i>) for configuration arrangements <i>a)</i> side-side, <i>b)</i> end-end, <i>c)</i> tee and <i>d)</i> cross. Molecular species interaction key: <i>A</i> - <i>A</i> (long dash), <i>A</i> - <i>B</i> (dotted), <i>A</i> - <i>B</i> & <i>B</i> - <i>A</i> (dot dashed), <i>B</i> - <i>A</i> (dashed) and <i>B</i> - <i>B</i> (solid).	46

3.6	2D representation of periodic boundary conditions. As a molecules leave one face its periodic image enters the opposite face.	47
3.7	Hexagonal crystals at distances r apart within a) smectic-A and b) smectic-B. Both showing a loss of long range positional order but b) has bond orientational order. Note: hexagonal crystals are drawn oversimplified as the packing arrangements within smectic-A and smectic-B layers are only pseudo-hexagonal.	50
4.1	Molecular dynamics simulation results for a 50:50 mixture of GGB rods with axial ratios of 3.5:1 (molecules A) and 3:1 (molecules B). Order parameter over all molecules, $\langle S^{all} \rangle$ (○), with corresponding order parameters for $\langle S^A \rangle$ (△) and $\langle S^B \rangle$ (▽). Potential energy of all molecules, $\langle U^* \rangle$ (+). In addition, results are shown of subsequent heating cycle for order parameter over all molecules, $\langle S^{all} \rangle$ (---) and potential energy of all molecules, $\langle U^* \rangle$ (—). . .	56
4.2	Pair distribution functions over all molecules, $g^{all}(r^*)$, in the isotropic phase at $\langle T^* \rangle = 2.5 \pm 0.04$ (---), nematic phase at $\langle T^* \rangle = 1.65 \pm 0.04$ (—), smectic phase at $\langle T^* \rangle = 1.32 \pm 0.03$ (+) with corresponding pair distribution functions for $g^{A-A}(r^*)$ (△) and $g^{B-B}(r^*)$ (▽).	60
4.3	Pair distribution functions over all molecules resolved parallel to the director, $g_{\parallel}^{all}(r^*)$, in the isotropic phase at $\langle T^* \rangle = 2.5 \pm 0.04$ (---), nematic phase at $\langle T^* \rangle = 1.65 \pm 0.04$ (—), smectic phase at $\langle T^* \rangle = 1.32 \pm 0.03$ (+) with corresponding pair distribution functions resolved parallel to the director for $g_{\parallel}^{A-A}(r^*)$ (△) and $g_{\parallel}^{B-B}(r^*)$ (▽).	61
4.4	Pair distribution functions over all molecules resolved perpendicular to the director, $g_{\perp}^{all}(r^*)$, in the isotropic phase at $\langle T^* \rangle = 2.5 \pm 0.04$ (---), nematic phase at $\langle T^* \rangle = 1.65 \pm 0.04$ (—), smectic phase at $\langle T^* \rangle = 1.32 \pm 0.03$ (+) with corresponding pair distribution functions resolved perpendicular to the director for $g_{\perp}^{A-A}(r^*)$ (△) and $g_{\perp}^{B-B}(r^*)$ (▽).	61
4.5	Second-rank orientational correlation functions over all molecules, $\langle G_2^{all}(r^*) \rangle$, in the isotropic phase at $\langle T^* \rangle = 2.32 \pm 0.04$ (---), nematic phase at $\langle T^* \rangle = 2.25 \pm 0.06$ (—), smectic phase at $\langle T^* \rangle = 1.32 \pm 0.03$ (+) and pre-smectic region at $\langle T^* \rangle = 1.65 \pm 0.04$ (×) with corresponding second-rank orientational correlation functions for $\langle G_2^{A-A}(r^*) \rangle$ (△) and $\langle G_2^{B-B}(r^*) \rangle$ (▽).	62
4.6	Bond orientational correlation function over all molecules, $g_6^{all}(r^*)$ (+), with corresponding bond orientational correlation functions for $g_6^{A-A}(r^*)$ (△) and $g_6^{B-B}(r^*)$ (▽).	63
4.7	Pair distribution function over all molecules resolved parallel to the director, $g_{\parallel}^{all}(r^*)$ with corresponding amplitudes of the pair distribution functions resolved parallel to the director for $g_{\parallel}^{A-A}(r^*)$ (△) and $g_{\parallel}^{B-B}(r^*)$ (▽). Pre-smectic region extends over the reduced temperature range $1.5 \leq \langle T^* \rangle \leq 1.7$	64

4.8	Maximum and minimum amplitudes of the pair distribution function over all molecules resolved parallel to the director, $g_{ }^{all}(r^*)$ as a function of reduced temperature, $\langle T^* \rangle$ with corresponding amplitudes of the pair distribution functions resolved parallel to the director for $g_{ }^{A-A}(r^*)$ (Δ) and $g_{ }^{B-B}(r^*)$ (∇). Pre-smectic region extends over the reduced temperature range $1.5 \leq \langle T^* \rangle \leq 1.7$	65
4.9	Difference between $\langle S^A \rangle$ and $\langle S^B \rangle$ as a function of reduced temperature, $\langle T^* \rangle$.	66
4.10	Three dimensional visualisation at $\langle T^* \rangle = 1.21 \pm 0.03$ of a) the smectic phase and b) a single smectic layer viewed parallel to the director. Molecular species key: dark particles are 3.5:1 (molecules A) and light particles are 3:1 (molecules B). These show some local compositional ordering within the smectic layers but no evidence of demixing.	68
5.1	Order parameter evolution (left column) and normalised distribution functions (right column) for a 50:50 mixture of GGB rods with axial ratios of 3.5:1 (molecules A) and 3:1 (molecules B) and reduced pressure of $\langle P^* \rangle = 4.0$. Order parameter resolved over all molecules $\langle S \rangle$ (+), $\langle S^A \rangle$ (Δ) and $\langle S^B \rangle$ (∇).	76
5.2	Temperature dependencies of a) order parameters, $\langle S^{all} \rangle$ and b) reduced potential energy, $\langle U^* \rangle$ of constant-NPH molecular dynamics simulations for 50:50 mixtures of GGB rods with axial ratios of 3.5:1 (molecules A) and 3:1 (molecules B) over reduced pressure range $1.0 \leq \langle P^* \rangle \leq 5.0$. Approximate location of phase boundaries are shown.	80
5.3	Temperature dependencies of a) reduced densities, $\langle \rho^* \rangle$ for mole fraction $\chi_A = 0.5$ over reduced pressure range $1.0 \leq \langle P^* \rangle \leq 5.0$ and b) schematic representations of $\langle T^* \rangle$ vs. $\langle \rho^* \rangle$ phase diagram of GB fluid.	81
5.4	Temperature dependencies of a) reduced densities, $\langle \rho^* \rangle$ for mole fraction $\chi_A = 0.5$ over reduced pressure range $1.0 \leq \langle P^* \rangle \leq 5.0$ and b) schematic representations of $\langle P^* \rangle$ vs. $\langle T^* \rangle$ phase diagram of GB fluid and isobar of traced out by simulation.	82
5.5	Pressure dependencies of reduced densities, $\langle \rho^* \rangle$ for mole fraction $\chi_A = 0.5$ over reduced pressure range $1.0 \leq \langle P^* \rangle \leq 5.0$	83
5.6	Temperature and volume relationship and corresponding Gibbs free energy as a function of temperature for a first-order transition at constant pressure.	84
5.7	3D visualisation of a) isotropic, b) nematic, c) smectic-A and d) smectic-B of a 50:50 GGB rods mixture (represented as unit vectors) with axial ratios of 3.5:1 (thick lines) and 3:1 (thin lines) at a reduced pressure $\langle P^* \rangle = 2.0$	85
5.8	Identification of smectic-A and smectic-B phases. a) pair distribution functions, b) in-plane six-fold bond orientation functions, c) and d) pair distribution functions resolved parallel and perpendicular to the director respectively at reduced pressure $\langle P^* \rangle = 1.0$.	86
5.9	a) Temperature dependencies of reduced potential energy (+) and fluctuations analysis of reduced potential energy (\times) for $\langle P^* \rangle = 5.0$ b) Evolution of reduced potential energy for $\langle P^* \rangle = 4.0$ at the $T_{SmA-SmB}$ transition temperature and for $\langle P^* \rangle = 5.0$ in the vicinity of the $N-SmA-SmB$ triple point.	90

5.10 Temperature dependencies of a) order parameters, $\langle S^{all} \rangle$ and b) reduced potential energy, $\langle U^* \rangle$ of constant- <i>NPH</i> molecular dynamics simulations of GGB rods with axial ratios of 3.5:1 (molecules <i>A</i>) and 3:1 (molecules <i>B</i>) at mole fractions $\chi_A = 0, 0.25, \dots, 1$ and reduced pressure of $\langle P^* \rangle = 5.0$	96
5.11 Temperature dependency of reduced density, $\langle \rho^* \rangle$ at mole fractions $\chi_A = 0, 0.25, \dots, 1$ and reduced pressure of $\langle P^* \rangle = 5.0$. The range of the nematic phase is indicated by horizontal arrows.	97
5.12 a) Concentration dependencies of transition temperatures at mole fractions $\chi_A = 0, 0.25, \dots, 1$ and reduced pressure of $\langle P^* \rangle = 5.0$. b) General schematic phase diagram leading to eutectic point χ_{eu} between different crystal structures α and β	101
5.13 Temperature dependencies of reduced potential energy (+) and fluctuations analysis of reduced potential energy (x) for $\chi_A = 1.0$	104
5.14 Identification of smectic-A and smectic-B phases. a) pair distribution functions, b) in-plane six-fold bond orientation functions, c) and d) pair distribution functions resolved parallel and perpendicular to the director respectively at concentration $\chi_A = 1.0$	105
5.15 Two extreme models for the molecular arrangements in a mixed smectic phase [30] Model a) segregated into domains of like molecules. Model b) randomly mixed smectic layers.	106
5.16 Concentration dependencies of smectic layer spacing at mole fractions $\chi_A = 0, 0.25, \dots, 1$ and reduced pressure of $\langle P^* \rangle = 5.0$ immediately proceeding <i>SmB</i> transition.	107
5.17 Temperature dependencies of reduced potential energy (+) and fluctuations analysis of reduced potential energy (x) for $\chi_A = 0.25$	108
5.18 Identification of smectic-A and smectic-B phases. a) pair distribution functions, b) in-plane six-fold bond orientation functions, c) and d) pair distribution functions resolved parallel and perpendicular to the director respectively at concentration $\chi_A = 0.25$	109
5.19 Concentration dependence of nematic range defined at $T_{I-N} - T_{N-Sm}$. The nematic range at $\chi_A \simeq 0.75$ greater than that of the homogeneous system of either molecule.	110
5.20 Concentration dependence of the McMillan ratio.	111

List of Tables

3.1	Parameter values used for this investigation. Those marked FIT were obtained via parameterisation described in this section.	45
4.1	Molecular dynamics simulation results of <i>cooling</i> a 50:50 mixture of GGB rods with axial ratios of 3.5:1 (molecules <i>A</i>) and 3:1 (molecules <i>B</i>). Columns key: $\langle T^* \rangle$ reduced temperature, $\langle U^* \rangle$ reduced potential energy per molecule (no long range correction), $\langle P^* \rangle$ reduced pressure (no long range correction), $\langle S^{all} \rangle$ order parameter resolved over all molecules, $\langle S^A \rangle$ molecules <i>A</i> order parameter, $\langle S^B \rangle$ molecules <i>B</i> order parameter and $\langle S^A - S^B \rangle$ order parameter difference.	58
4.2	Molecular dynamics simulation results of <i>heating</i> a 50:50 mixture of GGB rods with axial ratios of 3.5:1 (molecules <i>A</i>) and 3:1 (molecules <i>B</i>). Columns key: as of Table 4.1	59
4.3	Numerical integration over the first coordination shell within the smectic phase, $\langle T^* \rangle = 1.32$, of the pair distribution function over all molecules, $g^{all}(r^*)$, with corresponding functions for $g^{A-A}(r^*)$ and $g^{B-B}(r^*)$	67
5.1	Histogram analysis of long time-scale orientational fluctuations close to the onset of orientational order for simulation at a reduced pressure of $\langle P^* \rangle = 4.0$ (Refer to Figure 5.1). Where the number of samples $N_S = 5000$ for $\langle T^* \rangle = 2.35 \pm 0.04$ and $N_S = 10,000$ for $\langle T^* \rangle = 2.26 \pm 0.05$, each sample equivalent to 100 MD steps.	78
5.2	Approximate location of T_{I-N} , T_{N-SmA} $T_{SmA-SmB}$ transition temperature and estimations of the nematic-smectic-A transition strength [98] over the reduced pressure range $1.0 \leq \langle P^* \rangle \leq 5.0$	79
5.3	Comparison between Luckhurst <i>et al</i> [85] constant- <i>NVE</i> simulation (displayed with the suffix “L”) and results obtained from the $\chi_A = 0$ constant- <i>NPH</i> simulation of this study.	99
5.4	Approximate location of T_{I-N} , T_{N-SmA} $T_{SmA-SmB}$ transition temperatures	100

LIST OF TABLES

A.1 Molecular dynamics simulation results of GGB rods with axial ratios of 3.5:1 (molecules <i>A</i>) and 3:1 (molecules <i>B</i>) at mole fraction $\chi_A = 0.5$ and reduced pressure $\langle P^* \rangle = 1.0$. Columns key: $\langle T^* \rangle$ reduced temperature, $\langle S^{all} \rangle$ order parameter resolved over all molecules, $\langle S^A \rangle$ molecules' <i>A</i> order parameter, $\langle S^B \rangle$ molecules' <i>B</i> order parameter and $\langle S^A \rangle - \langle S^B \rangle$ order parameter difference. $\langle P^* \rangle$ reduced pressure (no long range correction), $\langle \rho^* \rangle$ reduced density and $\langle U^* \rangle$ reduced potential energy per molecule (no long range correction),	129
A.2 Molecular dynamics simulation results of GGB rods with axial ratios of 3.5:1 (molecules <i>A</i>) and 3:1 (molecules <i>B</i>) at mole fraction $\chi_A = 0.5$ and reduced pressure $\langle P^* \rangle = 2.0$. Columns key: as of Table A.1	130
A.3 Molecular dynamics simulation results of GGB rods with axial ratios of 3.5:1 (molecules <i>A</i>) and 3:1 (molecules <i>B</i>) at mole fraction $\chi_A = 0.5$ and reduced pressure $\langle P^* \rangle = 3.0$. Columns key: as of Table A.1	131
A.4 Molecular dynamics simulation results of GGB rods with axial ratios of 3.5:1 (molecules <i>A</i>) and 3:1 (molecules <i>B</i>) at mole fraction $\chi_A = 0.5$ and reduced pressure $\langle P^* \rangle = 4.0$. Columns key: as of Table A.1	132
A.5 Molecular dynamics simulation results of GGB rods with axial ratios of 3.5:1 (molecules <i>A</i>) and 3:1 (molecules <i>B</i>) at mole fraction $\chi_A = 0.5$ and reduced pressure $\langle P^* \rangle = 5.0$. Columns key: as of Table A.1	133
B.1 Molecular dynamics simulation results of GGB rods with axial ratios of 3.5:1 (molecules <i>A</i>) and 3:1 (molecules <i>B</i>) at mole fraction $\chi_A = 0.0$ and reduced pressure $\langle P^* \rangle = 5.0$. Columns key: $\langle T^* \rangle$ reduced temperature, $\langle S^{all} \rangle$ order parameter resolved over all molecules, $\langle S^A \rangle$ molecules' <i>A</i> order parameter, $\langle S^B \rangle$ molecules' <i>B</i> order parameter and $\langle S^A \rangle - \langle S^B \rangle$ order parameter difference. $\langle P^* \rangle$ reduced pressure (no long range correction), $\langle \rho^* \rangle$ reduced density and $\langle U^* \rangle$ reduced potential energy per molecule (no long range correction),	135
B.2 Molecular dynamics simulation results of GGB rods with axial ratios of 3.5:1 (molecules <i>A</i>) and 3:1 (molecules <i>B</i>) at mole fraction $\chi_A = 0.25$ and reduced pressure $\langle P^* \rangle = 5.0$. Columns key: as Table B.1	136
B.3 Molecular dynamics simulation results of GGB rods with axial ratios of 3.5:1 (molecules <i>A</i>) and 3:1 (molecules <i>B</i>) at mole fraction $\chi_A = 0.75$ and reduced pressure $\langle P^* \rangle = 5.0$. Columns key: as Table B.1	138
B.4 Molecular dynamics simulation results of GGB rods with axial ratios of 3.5:1 (molecules <i>A</i>) and 3:1 (molecules <i>B</i>) at mole fraction $\chi_A = 1.0$ and reduced pressure $\langle P^* \rangle = 5.0$. Columns key: as Table B.1	139

Chapter 1

Introduction

1.1 A brief history

In a novel by Edgar Allan Poe [1], written in 1838, the first description of an anisotropic fluid arguably appears [2]. It was some 15 years later until the first scientific discovery of their existence was reported by R. Virchow [3]. During the examination of the outer covering of nerve fibres under polarised light, Virchow noted that the samples showed patterns which were typical of solids but which clearly were not.

One of the dominant figures in the early research was O. Lehmann. In 1889 he noted that some substances do not crystallise from clear liquids, rather they change first to an amorphous form [4]. Several chemists (P. Planar [5], O. Löbisch [6] and B. Raymann [7]) reported that cholesteric esters produce iridescent colours when cooled. However, the credit for discovering liquid crystals is usually given to F. Reinitzner [8]. In 1888, he reported

CHAPTER 1. INTRODUCTION

that cholesterol has two melting points; at 145.5°C (cloudy liquid) and at 178.5°C (clear).

Lehmann performed a series of experiments with samples provided by Reinitzner. Finally, Reinitzner was convinced that these samples displayed intermediate phases (or *mesogenic phases*¹) and invented the term *liquid crystals*.

The unique properties of mesogenic materials have been exploited in many devices, noticeably in condensed matter systems such as display systems. A lot of progress has been made in understanding the properties of liquid crystals but many outstanding properties are still not fully understood.

1.2 Classification of liquid crystals

Mesogenic materials can be classified in two distinct categories; disordered crystal mesophases and ordered fluid mesophases. Disordered crystal mesophases have their constituent molecules fixed at lattice sites, preventing translation, but have orientational freedom. These mesophases are termed plastic crystals as they are easily deformed under stress. Ordered fluid mesophases exhibit long range orientational order with or without some long range translational order and, hence, are termed liquid crystals. They are conventionally classified in two categories; thermotropic and lyotropic liquid crystals. Thermotropic materials form mesophases upon variation in temperature, whereas lyotropic do so by changes in concentration. Friedel [9] was the first to propose the mesophasic classes of nematic, cholesteric and smectic by their inherent symmetry (Figure 1.1). For example,

¹derived from mesomorphic meaning intermediate

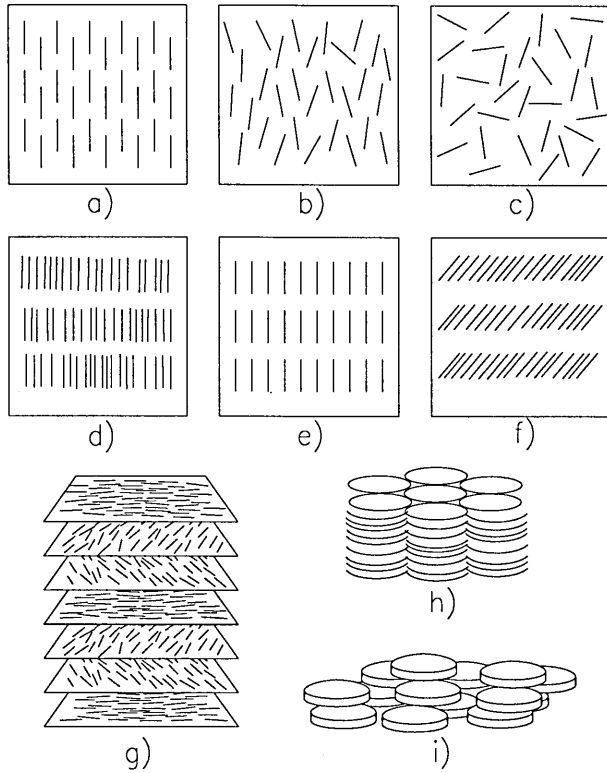


Figure 1.1: Schematics of some calamitic and discotic liquid crystals: a) crystal, b) nematic, c) isotropic, d) smectic-*A*, e) smectic-*B*, f) smectic-*C*, g) cholesteric, h) discotic columnar and i) discotic nematic [10, 11].

nematics and smectics consist of molecules which are mutually oriented along some preferred direction (or director) but differ regarding translational order among the molecular centres of mass; nematics have no long range translational order (Figure 1.1b), whereas, smectics (Figure 1.1d–f) possess quasi-long ranged layer ordering. Numerous classifications of smectics exist depending upon the degree of ordering within the layers, *i.e.* translational, orientational and tilt (see, for example, Chandrasekhar [10] and Luckhurst and Gray [11]).

Early investigations of Lehmann [4] and others [12] originated the principle that molecules had to be rod-like in shape (calamitic liquid crystals) in order to form mesophases.

CHAPTER 1. INTRODUCTION

In the late 1970's, Chandrasekhar [13] and coworkers (see [14] for review), showed that disk-like molecules (or discotic liquid crystals) may also exhibit mesophases, *e.g.* discotic nematic (Figure 1.1i) and discotic columnar (Figure 1.1h). Interest in discotic liquid crystals has grown since the discovery that derivatives of benzene and triphenylene form mesophases which possess unique properties which can be utilised in a variety of applications such as; low power display devices, optical data storage and molecular wires.

1.3 Mixtures of Liquid Crystals

It is far from hard to conceive that the combination of two or more molecules of varying chemical composition, geometric size and shape opens up the possibility of novel phases not attainable in either pure systems. Scientists with interests in liquid crystals have long since exploited this phenomenon and readily developed novel mesophases from the combination of two or more "off the shelf" mesogens. The use of mixtures in display devices is widely practised whereby, for example, the nematic can be shown to be stable over a wider range of temperatures thus increasing the utility of the device.

A problematic feature of mixtures is that they may not be stable. That is to say that not all components of a mixture are necessarily miscible with each other. Some systems will mix and others demix or phase separate into two phases if the constituent molecules are sufficiently unfavourable in some sense. Aggregation in other systems can be a further problem. Yet the physical explanation of many of these phenomena, although scientifically

fascinating, is generally unresolved.

1.4 The Role of Computer Simulations

Computer simulations are becoming increasingly important, as they essentially fill the gap between experimental and theoretical routes as illustrated by Allen and Tildesley [15] (Figure 1.2). The first computer simulations of liquids were performed in the early 1950's. This work lead to many advances in both theories of liquids and simulation techniques. Within statistical mechanics, computer simulations provide an essentially exact solution for the model system which would otherwise be difficult to solve or only be solvable via approximate methods.

1.5 Aims

The work described in this thesis relates to computer simulations performed with the aim of providing a greater understanding of the phase behaviour and structural properties of binary liquid crystal mixtures. Specific attention has been focused on the pressure and concentration dependence of a much used intermolecular potential, the Gay-Berne [16]. As an initial step to study the phase behaviour of a bi-disperse system, a recent generalisation of the Gay-Berne intermolecular potential [17] was employed in a system where one molecular species differed slightly from the other. The basic parameterisation used was one for which there is a considerable volume of published data. This study was conducted

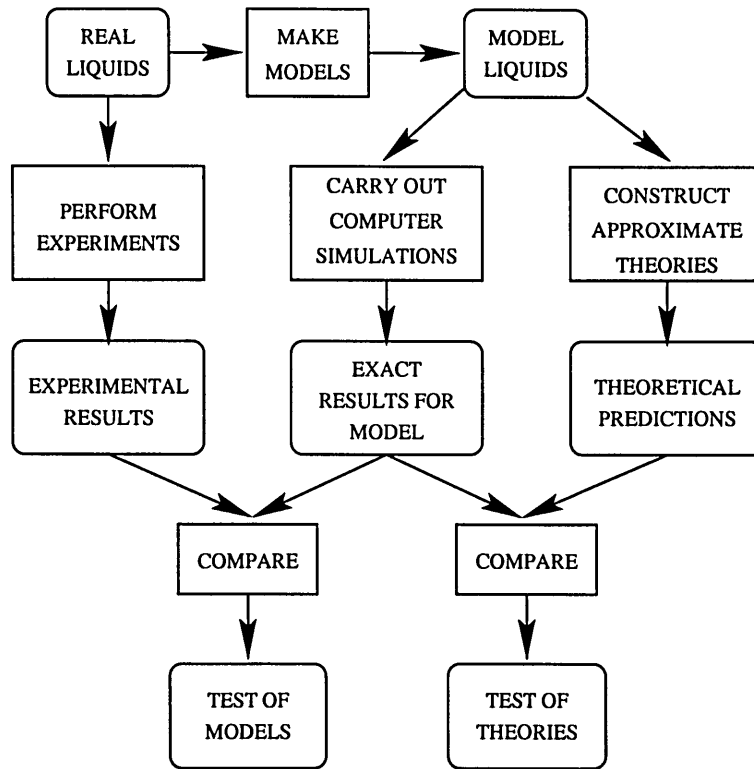


Figure 1.2: The role of computer simulations as described by [15].

mainly to evaluate the viability of the Generalisation Gay-Berne intermolecular potential. Its successful evaluation would offer a viable and computational efficient route to the study of multicomponent and even polydisperse systems.

The studies of the pressure and concentration dependence of the phase behaviour and structural properties of binary liquid crystal mixtures were conducted mainly as to gain a greater understanding of the underlying processes taking place in a generic liquid crystal mixture. More explicitly, the studies aimed to construct phase diagrams resembling those found experimentally and, if successful in this, used to corroborate theories. An additional

goal was to explore any properties or phases not obtainable from either pure system.

1.6 Layout of Thesis

The remaining chapters are arranged as follows. In chapter 2, a brief review of experimental, theoretical and simulation work is presented within the field of liquid crystal mixtures. Chapter 3 presents an overview of the modelling techniques used for liquid phases including the parameterisation of Generalised Gay-Berne intermolecular potential.

Chapters 4 and 5 contain results and analysis from computer simulation of bi-disperse liquid crystals with length to breadth axial ratios of 3.5 to 1 and 3 to 1. Particular attention is paid to the effect of concentration and pressure on phase behaviour and structural properties. Two main studies have been undertaken:

1. (Chapter 4) A constant-*NVE* molecular dynamics simulation of a bi-disperse liquid crystal mixture at a fixed concentration of 50:50; attempts to evaluate the viability of the intermolecular potential, quantify the difference in order parameter between molecular species and investigate the nature of phase transitions.
2. (Chapter 5) Chapter 5 consists of two sections *a*) “Influence of pressure” (section 5.2) and *b*) “Influence of concentration” (section 5.3) each study comprising of a series of constant-*NPH* molecular dynamics simulations of bi-disperse liquid crystal mixtures at various pressures and concentrations; attempts to construct phase diagrams, qualitatively describe phase behaviour properties and identify novel phases.

CHAPTER 1. INTRODUCTION

And finally, chapter 6 summarises the key conclusions and makes suggestions for future work.

Chapter 2

Literature review

In this chapter, a brief review of experimental, theoretical and simulation work is presented within the field of liquid crystal mixtures.

2.1 Experimental

Over the last two decades, liquid crystal mixtures containing a variety of chemical compositions, molecular shapes and sizes have demonstrated many rich phase diagrams and novel mesophases. Reentrant phenomena in liquid crystal mixtures, generally associated with weakly stable smectic phases, have been reported in many polar rod-like systems. Cladis [18] (1975) reported the first such reentrant phenomenon in mixtures of two cyano compounds. Subsequently, Cladis *et al* [19] reported reentrance in a pure compound at elevated pressures. In 1979, the first observation of a transition between two smectic-*A* phases was made by Sigaud *et al* [20]. A year later, Yu and Saupe [21] presented the first

CHAPTER 2. LITERATURE REVIEW

conclusive evidence of a biaxial phase in a mixture of rod-like and disk-like molecules.

Multiplexed twisted nematic displays requiring fast electro-optic characteristics can be achieved using hybrid liquid crystal mixtures of terminally cyano-substituted nematogens and non-polar nematogens [22]. These hybrid mixtures possess the required low bend to splay elastic constant ratio, k_{33}/k_{11} . Increasing the alkyl chain length can further reduce this ratio but often results in the introduction of an injected smectic phase [23, 24]. Gruler [25] postulated that the temperature dependencies of the elastic constants can be attributed to the change in local ordering of the nematic. The four nematic regions described are;

1. pre-transitional isotropic ordering,
2. nematic without any local positional ordering,
3. pre-transitional nematic ordering (increase in k_{11} and k_{33}) and
4. smectic-like local ordering (increase in k_{11} and decrease in k_{33}).

Bradshaw and Raynes [26, 27, 28] measured the elastic constants of various hybrid mixtures and successfully identified the latter two ordering phenomena. In particular, the isotropic-nematic transition temperature varied linearly with mole fraction across the phase diagram for the mixture composed of BDH eutectic mixture E1 (terminally cyano-substituted nematogens) and a *p*-dialkyl nematic mixture (non-polar end group nematogen) *i.e.* a four component system. Within the pre-transitional ordering region, the smectic layers cannot

CHAPTER 2. LITERATURE REVIEW

support bend deformation and thus the increase in k_{33} is attributed to short-lived pseudo layers which oppose such deformation. In contrast the increase in k_{11} is related to the smectic layer compression elastic constant. The results reveal a strong correlation between k_{11}/k_{33} and smectic-like ordering. Furthermore, they substantiate the theory of van der Meer *et al* [29] which predicts a correlation between k_{11}/k_{33} and the mean square molecular displacement.

Lydon and Coakley [30] investigated the miscibility of 8CB and ODOBAF via X-ray diffraction. They found that the smectic layer spacing thickness varies smoothly across the compositional range, in spite of the difference in molecular lengths and the two different pure smectic phase structures. The resulting smectic layers were found to adhere to one of several different symmetries; segregated into domains several layers thick, randomly mixed within each layer or one out of a range of intermediate possibilities.

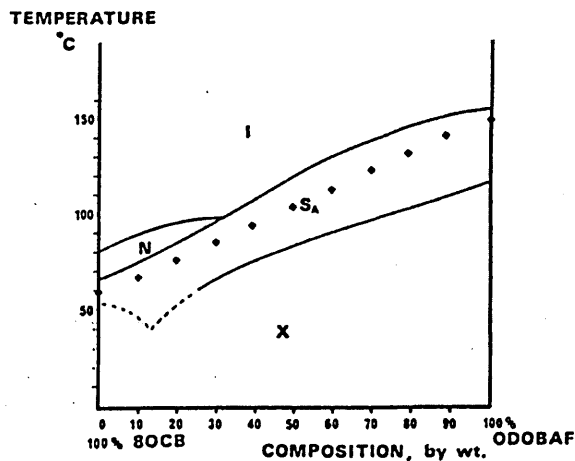


Figure 2.1: Phase diagram for binary mixture of 8OCB and ODOBAF [30].

Shashidhar and co-workers [31, 32, 33] investigated a binary mixture of the polar molecules DB8ONO₂ and DB10ONO₂. They reported a rich phase diagram with no less than 3 reentrant nematics, 2 reentrant smectic phases and a smectic-*A*-reentrant nematic-reentrant smectic-*A*_(re) tricritical point. At a mole fraction of 55%, the phase diagram in Figure 2.2 reveals 11 phase transitions. A great deal of interest still surrounds the extremely

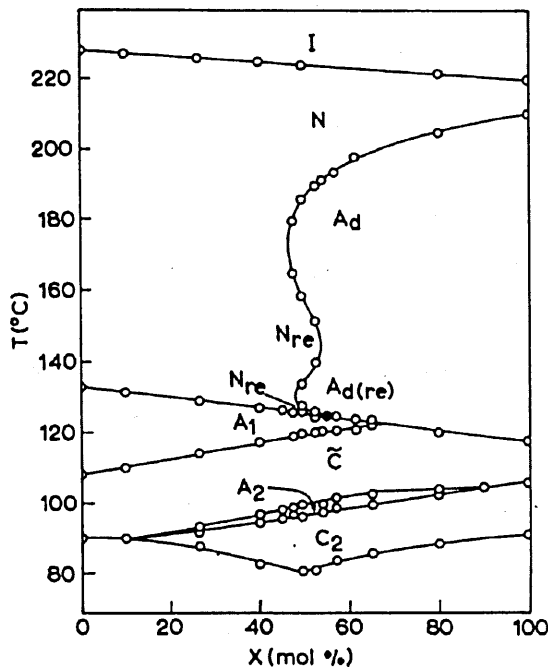


Figure 2.2: Phase diagram for binary mixture of DB8NO₂ and DB10NO₂ [31].

rich phase diagram of polar liquid crystal mixtures. A recent paper by Nounesis *et al* [34] shows evidence of a first-order transition between two nematic phases in the vicinity of the smectic-*A*-smectic-*A*_(re) phase boundary. The understanding of this rich phase behaviour has largely been based on phenomenological models of frustrated smectics in which there is

CHAPTER 2. LITERATURE REVIEW

a competition between smectic layer thickness and molecular lengths.

The reentrant phenomena in polar smectic liquid crystals are well established. In recent years, the possibility of an isolated reentrant nematic region (or a “nematic island”) near a smectic-smectic critical point has been reported experimentally by Hardouin *et al* [35] and Pfeiffer *et al* [36, 37] in mixtures of 10OPCBOB and 11.O.NCS. This behaviour has also been predicted theoretically by Prost and Toner [38] and more recently by Sear and Jackson [39]. A high-resolution ‘ac calorimetric’ investigation by Wu *et al* [40] confirms the findings of the early work of Pfeiffer *et al* [36] and Heppke *et al* [41].

Heppke *et al* [42] investigated the effect of adding mesogenic chiral compounds with high twisting power to a nematic mixture RO-TN404 consisting of cyano-substituted pyrimidine and biphenyl derivates. The authors reported that an induced blue phase can be obtained with less than 10% of a chiral compound. Under the influence of an electric field, a reentrant cholesteric phase can be observed.

Prior to 1990, no paper had reported a miscibility gap (or coexistence curve) and consolute critical point for liquid crystal mixtures. In a paper by Sigaud *et al* [43], the severely limiting experimental conditions were given explaining the lack of such an observation;

1. stability of the mesophase with respect to any other phases or crystallisation,
2. unlike mesogens with similar mesophasic temperatures and,
3. stability of the mesophase over the concentration-temperature phase diagram.

CHAPTER 2. LITERATURE REVIEW

Sigaud *et al* [43] reported the first observation of a miscibility gap and consolute critical point in a smectic-*A* phase for a mixture of unlike chemical structures rather than dissimilar geometrical sizes (Figure 2.3*a*). In common with previous work [44] the first component (molecule *A*) was a polar molecule with a layer spacing to molecule length of $d/l = 37.2/32.5$. There are no reports of a miscibility gap in a mixture of the common non-polar liquid crystals with two aliphatic chains. Instead, a second non-polar molecule was chosen (molecule *B*) which has one aliphatic and one perfluoralkyl chain with $d/l = 30.4/31.0$. The authors claim the success of the investigation relied upon two characteristics of the perfluoro component; a greater stiffness owing to the steric hindrance of the fluorine atoms and the incompatibility of the perfluoro chains with the aliphatic ones. The nematic eutectic (or negative azeotrope) at a mole fraction of $\chi_B \simeq 45\%$ confirms that the unlike *AB* interactions are unfavourable to mixing in the smectic phase. The authors regard the approximate position of the consolute critical point and that of the nematic eutectic not to be an accident. Rather the proximity of the two points is taken to be in qualitative agreement with Brochard's theory of demixing in mesomorphic mixtures [45]. The result of mixing/demixing is also evident within the smectic layer spacing (Figure 2.3*b*).

2.2 Theoretical

With a handful of exceptions, for instance the two-dimensional Ising model [46], there are no exact solutions for the statistical mechanics of non-trivial systems [47]. A brief

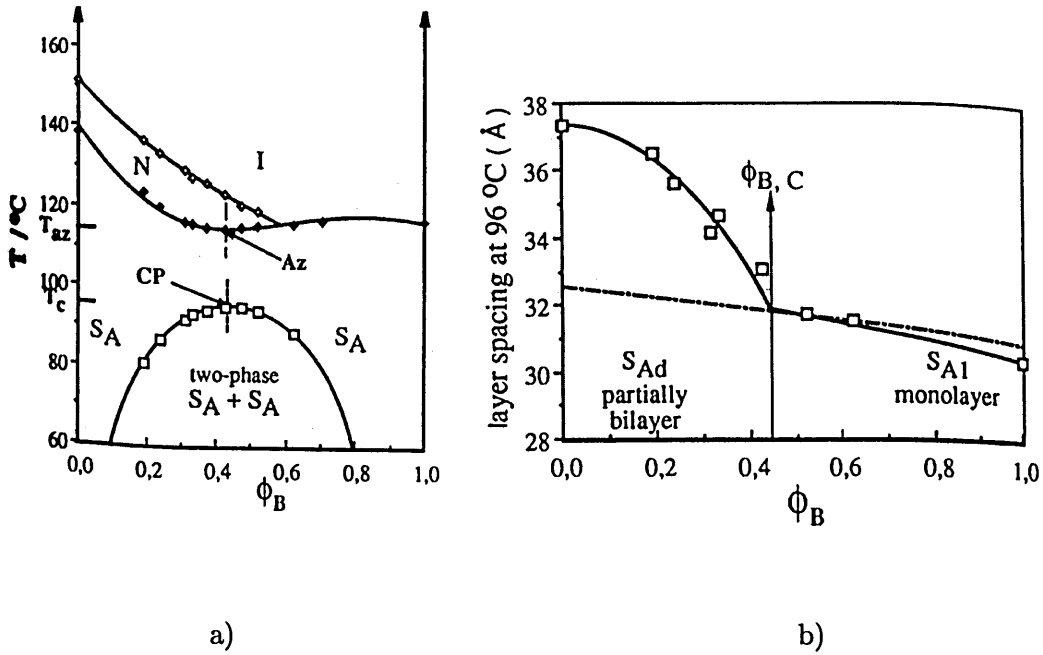


Figure 2.3: a) Phase diagram for binary mixture of a polar molecule and non-polar molecule. b) Layer spacing as a function of composition at constant temperature of slightly above T_C [43].

review is presented of some commonly used approximations for liquid crystals.

In the late 1940s, seminal work by Onsager [48] proved that the isotropic-nematic transition can be explained in terms of excluded volume terms alone, within a system of hard spherocylinders in the limit of infinite length to width (L/D) ratio. Onsager focused on the minimisation of the Helmholtz free energy [49]. The Helmholtz free energy of a canonical ensemble is,

$$F(N, V, T) = -k_B T \ln Q_N(V, T) \quad (2.1)$$

where $Q_N(V, T)$ is the canonical partition function comprising contributions from the con-

figuration partition functional, $Z_N(V, T)$ and de Broglie thermal wavelength, $Q^o(T)$,

$$Q_N(V, T) = Q^o(T) \frac{Z_N(V, T)}{N!}. \quad (2.2)$$

Thus the Helmholtz free energy can be calculated from the difference between a reference chemical potential, $\mu^o(T, \mu_0, \mu_1, \dots)$ and $F(N, V, T)$,

$$\Delta F(N, V, T) = N\mu^o(T, \mu_0, \mu_1, \dots) - Nk_B T \ln \left(Q^o(T) \frac{Z_N(V, T)}{N!} \right) \quad (2.3)$$

which, from an appropriate density expansion of the configurational integral, can be expressed as a virial expansion,

$$\frac{\Delta F(N, V, T)}{Nk_B T} = \frac{\mu^o(T, \mu_0, \mu_1, \dots)}{k_B T} - 1 + \ln \left(\frac{V}{N} \right) + B_2 \rho + \left(\frac{1}{2} \right) B_3 \rho^2 + \dots \quad (2.4)$$

where B_2 and B_3 are the second and third virial coefficients. Hence, the spatial correlations are expanded in terms of cluster integrals in which the virial terms account for effects of coupling within the ensemble amongst clusters of $2, 3, 4, \dots, N$ particles. In the limit $L/D \rightarrow \infty$, Onsager argued that all virial coefficients higher than the second are negligible, i.e. $B_n/B_2^{(n-1)} \rightarrow 0$. The system is able to form the nematic through its ability to gain translational entropy at the expense of some orientational entropy. However, Onsager's excluded volume theory is in poor agreement with the typical experimental values for order parameter and change in density at the transition. Despite these limitations, it remains the only exactly solvable model exhibiting an isotropic-nematic transition with full translational and orientational degrees of freedom.

Almost a decade later, Maier and Saupe [50] proposed an alternative theory using

CHAPTER 2. LITERATURE REVIEW

a system of classical spin vectors constrained on a cubic lattice. The system, solved by mean-field approximations, takes into account attractive intermolecular nearest neighbour interactions. Compared to the Onsager, the Maier and Saupe theory predicts a strongly first order isotropic-nematic transition and a nematic order parameter closer to that observed experimentally.

Experimental work of Yu and Saupe [21] substantiated the prediction of Alben [51] that a biaxial phase could be formed by a mixture of rod-like and disk-like nematogens. Recently, the Onsager theory has undergone several extensions, primarily by Lekkerkerker and coworkers, to incorporate mixtures of geometrically different molecules. Encouraged by the work of Yu and Saupe [21] and Alben [51], Stroobants and Lekkerkerker [52] extended the theory to solutions of cylindrically symmetrical rod-like (molecule *A*) and disk-like (molecules *B*) particles showing that the mixture forms three mesophases depending on the concentration and composition (Figure 2.4); a uniaxial nematic (N_+) within rod-rich mixtures, a uniaxial nematic (N_-) within disk-rich mixtures and a biaxial phase (*B*). The phase diagram is predicted to be symmetrical around $\chi_A = 0.5$. The first-order isotropic-nematic transition for rod-like molecules is predicted to become weaker and move towards a lower density as the mole fraction of disk-like molecules is increased towards $\chi_A = 0.5$. The authors report that the free energy of the biaxial phase is lower than that of the coexisting uniaxial phases at equivalent densities. In addition, the nematic-biaxial transition is predicted to be second-order.

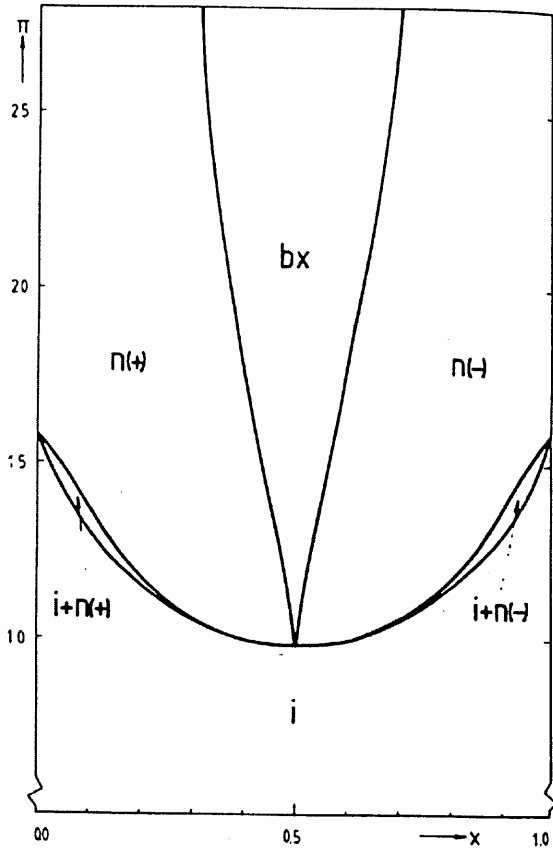


Figure 2.4: Predicted phase diagram for cylindrically symmetrical rod/disk-like mixture from Stroobants and Lekkerkerker [52] extension of Onsager theory.

From a Maier-Saupe mean-field theory of a mixture of rod-like and disk-like molecules interacting via an anisotropic pseudo-potential, Palfy-Muhoray *et al* [53] predicted the two uniaxial and one biaxial mesophases similarly to [52] (Figure 2.5a). However, they concluded that the biaxial phase is thermodynamically unstable since the corresponding free energy is greater than the two coexisting uniaxial phases (Figure 2.5b) in marked contrast with the Onsager theory prediction of Stroobants and Lekkerkerker [52]. Similar mean-field work by Goetz and Hoatson [54] used a generalised pseudo-potential for biaxial

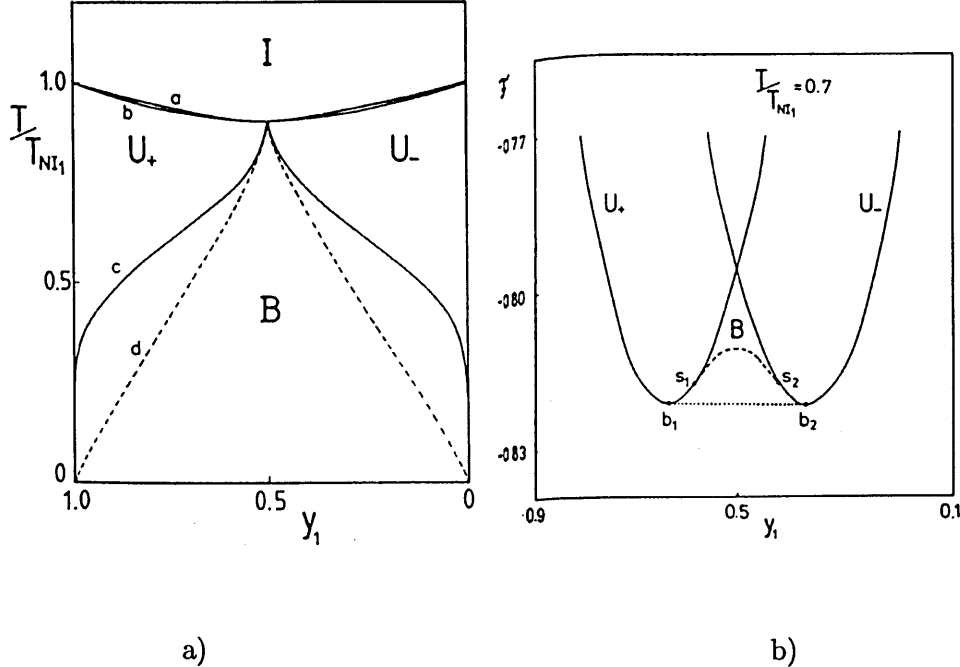


Figure 2.5: Palfy-Muhoray *et al* [53] mean-field theory predicted *a)* phase diagram and *b)* free energy for rod/disk mixture.

molecules within rod/rod, disk/disk and rod/disk mixtures. They concluded that a mixture of slightly biaxial rod-like and disk-like molecules (whose anisotropic shapes are comparable to those of real mesogens) will phase separate into two uniaxial phases in preference to a biaxial phase, agreeing with [53]. Nevertheless, in terms of free energy, a stable biaxial phase is predicted for highly asymmetric rod-like and disk-like molecules.

A numerical analysis by Lekkerkerker *et al* [55] and an analytical Gaussian approximation by Odijk and Lekkerkerker *et al* [56] extended the Onsager theory to solutions of rod-like molecules with the same diameter but two different lengths, *i.e.* a bi-disperse system. Both sets of analysis predicted a number of salient features (Figure 2.6) for two different length ratios $L_A/L_B = 2$ and 5. For the smaller ratio;

CHAPTER 2. LITERATURE REVIEW

- i) strong fractionation effect (the longer molecules preferentially enter the nematic phase),
- ii) widened biphasic gap (the isotropic-nematic coexistence may be wider than that of a one component system),
- iii) in the nematic phase, the long molecules are consistently more ordered than the short molecules,

and for $L_A/L_B \geq 3.5$,

- iv) reentrant nematic phase,
- v) $N_1 - N_2$ biphasic region which is independent of pressure (as predicted by Vroege and Lekkerkerker [57] and confirmed ¹ by van Roij and Mulder [59])
- v) $I - N_1 - N_2$ triphasic region (as [58]),

and as predicted by Mulder [60] and Sluckin [61],

- vi) postponement of nematic-smectic transition to higher densities arising due to a widened nematic phase.

In a recent paper by Vroege and Lekkerkerker [57], the nematic-nematic transition of a bi-disperse mixture of rigid hard rods is attributed to a balance between orientational entropy and entropy of mixing and not the excluded volume effect. Further Maier-Saupe-like and Onsager-like analysis by Sluckin [61] confirms the widening of the biphasic gap and postponement of smectic transition to higher densities in polydisperse systems.

¹Birshtein *et al* [58] predicted the $N_1 - N_2$ biphasic to be closed by a critical point which effectively makes the biphasic phase *dependent* on pressure

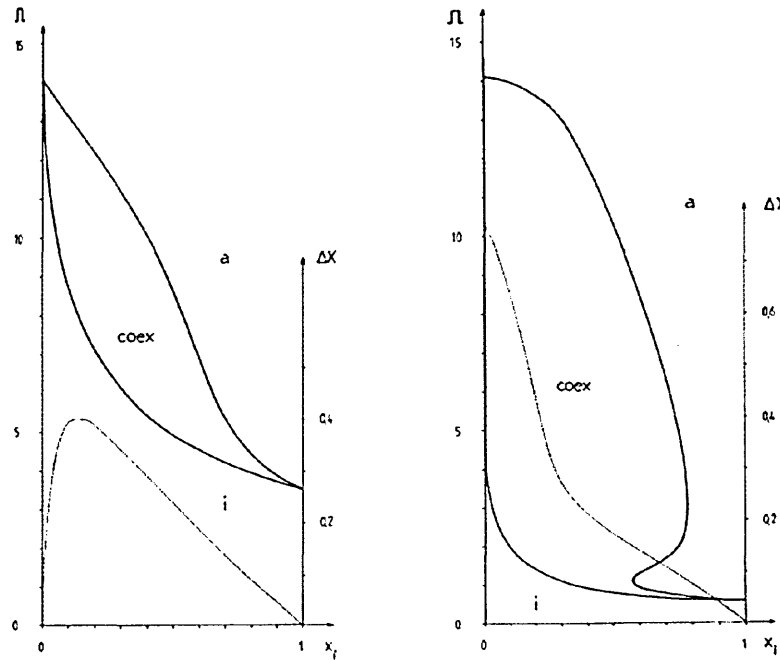


Figure 2.6: Gaussian approximate (Onsager) predicted pressure (Π) *vs.* concentration phase diagram [55] of bi-disperse system for $L_A/L_B = 2$ (left) and $L_A/L_B = 5$ (right). Dotted line represents the difference in mole fractions.

Sear and Jackson [39] predicted an isolated reentrant nematic (Figure 2.7) in a binary mixture of associating cylindrical molecules whereby an intermolecular potential mimics hydrogen bonding allowing a pair of molecules to dimerise end-to-end. Unlike experiments by Hardouin *et al* [35] and Pfeiffer [36], no smectic-smectic critical point is predicted. The reentrant nematic island is attributed to competing tendencies of smectic layer spacings of differing wavelengths.

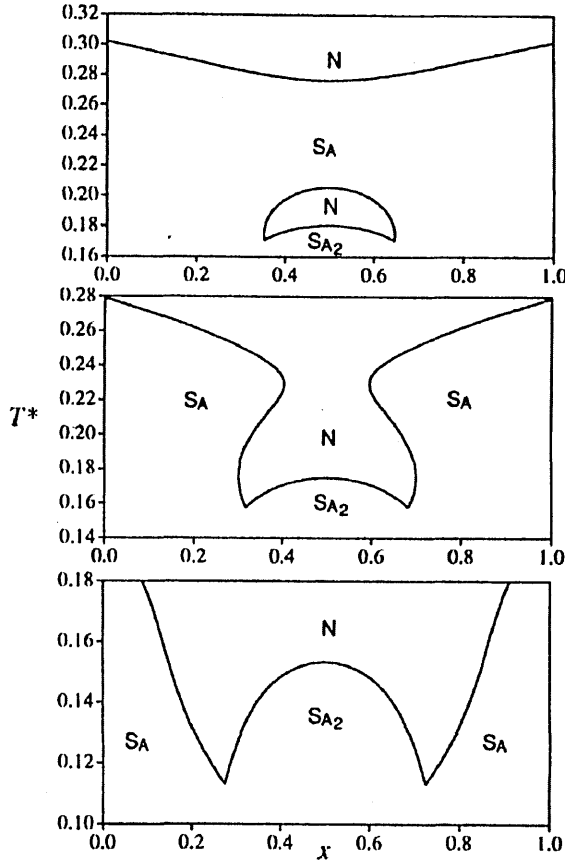


Figure 2.7: Constant pressure phase diagrams of associating cylindrical molecules [39]. Pressure is reduced from top to bottom diagrams.

2.3 Simulation

In the early 1980's, Hashim *et al* [62] performed a Monte Carlo (MC) simulation of an equimolar mixture containing rod-like and disk-like molecules constrained to the sites of a simple cubic lattice. The molecules interacted via an anisotropic potential which was restricted to nearest and next nearest neighbours. From this simple model, they concluded that the mixture phase separated into two uniaxial phases substantiating the claims of

CHAPTER 2. LITERATURE REVIEW

Palffy-Muhoray [53] that the biaxial phase is thermodynamically unstable. A decade later, Hashim *et al* [63] re-addressed this problem. Two models were developed; in MODEL I phase separation was not allowed as the molecules were confined to the sites of a simple cubic lattice so that each rod-like molecule had 6 nearest neighbour disk-like molecules, and vice versa; in MODEL II particle exchanges were allowed to enable the possibility of phase separation. They concluded MODEL I demonstrated a biaxial nematic phase whereas MODEL II separated into two uniaxial nematic phases. However, the later predictions of Goetz and Hoatson [54], that a mixture of highly asymmetric rod-like and disk-like molecules can exhibit a stable biaxial phase, remains unresolved.

A similar lattice based simulation by Hashim *et al* [64] investigated the 95% solvent and 5% solute mixture of anisotropic molecules. The presence of the solute molecule was found to stabilise the nematic phase, in agreement with a molecular field approximation of Humphries, James and Luckhurst [65]. However the theory did over estimate the isotropic-nematic transition temperature by 12%.

Following the extension of the Onsager theory to bi-disperse system [52], Stroobants [66, 67] used a constant-pressure MC simulation to investigate a binary mixture of hard parallel aligned spherocylinders beyond the nematic phase. The shorter spherocylinder was fixed at $L_1/D = 1$, where L_1 is the length of the cylindrical segment. While the longer spherocylinder ranged between $1.3 \leq L_2/D \leq 2.1$ where the mole fraction was adjusted to maintain equal molecular volumes. For $L_2/D > 1.6$ the system exhibited a thermodynam-

ically stable columnar phase which is not present for a homogeneous system (Figure 2.8).

The nematic-smectic transition was postponed approximately linearly by increasing L_2/D and was preempted by a nematic-columnar phase for $L_2/D > 1.9$.

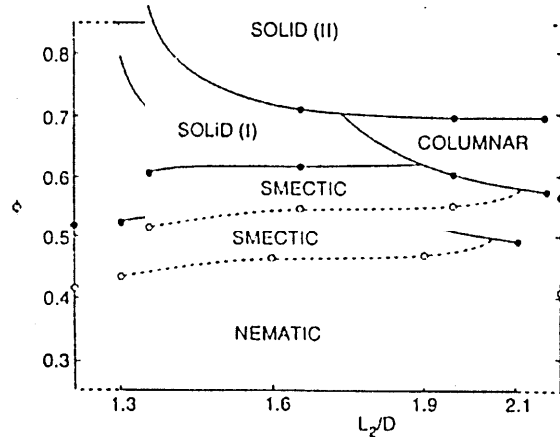


Figure 2.8: Phase behaviour of a binary mixture of hard parallel spherocylinders as a function of L_2/D .

Computer simulations of bi-disperse systems using soft potentials have considered mixtures of Gay-Berne particles and Lennard-Jones sites [68]. More recently, Lukáč and Vesely [69] have reported a brief investigation of a mixture of Gay-Berne molecules based on Lorentz-Berthelot mixing rules and modified well-depth exponents μ and ν (Refer to Chapter 3 for further details). However, it must be noted that this modified potential fails to differentiate between all of the T-configurations available to this system. Nevertheless, from a stable smectic phase 50% of the molecules within the simulation were converted to a variety of new species interacting with the modified Gay-Berne potential, and the effects noted thereafter. The authors reported some systems to demix and others not. No

CHAPTER 2. LITERATURE REVIEW

explanation of these occurrences was offered. However, the longer molecules were observed to be more ordered than the short molecules in agreement with the theoretical predictions of Lekkerkerker and co-workers.

Camp and Allen [70] studied a mixture of hard rod-like and disk-like molecules with aspect ratios of 10:1 and 1:10 respectively using a constant-pressure MC simulation. Two mole fractions were investigated; for $\chi_{rods} = 0.5$ isotropic–biaxial-nematic and for $\chi_{rods} = 0.6$ isotropic–uniaxial-nematic–biaxial-nematic phase transitions were observed. Comparisons were drawn between the simulation results, Onsager theory and Onsager theories incorporating higher virial coefficients indirectly by resummation such as the y -expansion-Onsager theory (Barboy) and renormalised two-particle theory (Parsons). Of these, the latter theory determined the most accurate prediction of the isotropic-nematic transition density (within 10%). However there was some evidence of demixing of the biaxial nematic phase at higher densities. Subsequently in a later paper, Camp *et al* [71] re-addressed this phase separation problem in a mixture of hard rod-like and disk-like molecules using molecules with greater elongation. They concluded that the region of biaxial-nematic phase stability is very small and is limited severely by demixing into two coexisting uniaxial-nematic phases. To date, all theoretical phase diagrams of such systems are symmetrical around $\chi_{rods} = 0.5$ (refer to section 2.2 and references therein). By contrast, these simulations show there to be a considerable asymmetry. Bolhuis [72] (a co-author of [71]) suggests that this symmetry found in the theoretical predictions is an artifact due to the fact that

CHAPTER 2. LITERATURE REVIEW

higher virial coefficients were neglected.

Chapter 3

Modelling Liquid Crystals

In this chapter, an overview of the modelling techniques used for liquid phases is presented.

3.1 Molecular Dynamics

3.1.1 Equation of motion

The microscopic state of a system can be expressed in terms of the positions \mathbf{q}_i and momenta \mathbf{p}_i of a constituent set of particles so that, assuming a classical description is adequate, the Hamiltonian \mathcal{H} of a system of N particles is a sum of the kinetic \mathcal{K} and potential energy \mathcal{V} functions,

$$\mathcal{H}(\mathbf{p}, \mathbf{q}) = \mathcal{K}(\mathbf{p}) + \mathcal{V}(\mathbf{q}). \quad (3.1)$$

The kinetic energy \mathcal{K} takes the form,

$$\mathcal{K} = \sum_{i=1}^N \sum_{\alpha} p_{i\alpha}^2 / 2m_i \quad (3.2)$$

where m_i is the molecular mass and α represents the different (x, y, z) components of the i^{th} molecular momentum. For an atomistic system, the potential energy \mathcal{V} may be separated into terms depending on the coordinates,

$$\mathcal{V} = \underbrace{\sum_i v_1(\mathbf{r}_i)}_{\text{external field}} + \underbrace{\sum_i \sum_{j \neq i} v_2(\mathbf{r}_i, \mathbf{r}_j)}_{\text{pair potential}} + \underbrace{\sum_i \sum_{j \neq i} \sum_{k \neq j \neq i} v_3(\mathbf{r}_i, \mathbf{r}_j, \mathbf{r}_k)}_{\text{three-body potential}} + \dots \quad (3.3)$$

where $\sum_i \sum_{j \neq i}$ indicates a summation over unique pairs i and j (for example, including ij but excluding ji). In the absence of an external field, the first term, v_1 , becomes zero. Three-body terms (and above) are rarely used in computer simulations, owing to the computer overheads of the summation, despite their sizeable potential energy contribution [73]. The many-body effects can be partially included by replacing v_2 with an effective pair potential v_2^{eff} which fortunately provides a remarkably good description of liquid properties.

Following Goldstein [74], it is possible to construct classical equations of motion in Hamiltonian, Lagrangian or Newtonian forms each of which can be used to integrate the time-evolution of the system and all of its mechanical properties. It is convenient to express equation 3.1 in the form of the Lagrangian equation of motion for generalised coordinates \mathbf{q}_k and their time derivatives $\dot{\mathbf{q}}_k$,

$$\frac{d}{dt} \left(\frac{\partial \mathcal{L}}{\partial \dot{\mathbf{q}}_k} \right) - \left(\frac{\partial \mathcal{L}}{\partial \mathbf{q}_k} \right) = 0. \quad (3.4)$$

Here, the Lagrangian, defined in terms of kinetic and potential energies $\mathcal{L} = \mathcal{K} - \mathcal{V}$, is assumed to be a function of $2(3N - \alpha) + 1$ independent variables,

$$(\mathbf{q}_1, \mathbf{q}_2, \dots, \mathbf{q}_{3N-\alpha}), (\dot{\mathbf{q}}_1, \dot{\mathbf{q}}_2, \dots, \dot{\mathbf{q}}_{3N-\alpha}), t \quad (3.5)$$

where α is the number of constraint equations. For a system of atoms with Cartesian coordinates \mathbf{r}_i with kinetic energy of equation 3.2 and interacting via a potential energy of equation 3.3 the Lagrangian equation of motion (equation 3.4) becomes,

$$m_i \ddot{\mathbf{r}}_i = \mathbf{f}_i \quad (3.6)$$

where m_i is the mass of particle i and the force on that particle is,

$$\mathbf{f}_i = \nabla_{\mathbf{r}_i} \mathcal{L} = -\nabla_{\mathbf{r}_i} \mathcal{V}. \quad (3.7)$$

Considering first spherical molecules, the equations of motion of equation 3.6 are $3N$ coupled second-ordered differential equations which, other than for a very limited number of molecules, cannot be solved directly. These coupled equations must therefore be solved numerically by finite difference methods. There are a number of finite difference methods available in the simulators toolbox, the *Verlet* algorithm [75] being the commonest choice (refer to section 3.1.2). The equation of motion for non-linear molecules takes a similar form and is discussed later 3.1.2.2.

3.1.2 Verlet algorithm

3.1.2.1 Translational motion

As described by Allen and Tildesley [15], the general scheme involves taking the known molecular positions at time t and advancing them to a later time $t + \delta t$ to a sufficient degree of accuracy. The choice of δt should be significantly smaller than the time taken to traverse its own length. The Verlet algorithm offers a direct solution to equation 3.6. The molecule i has coordinate \mathbf{r}_i at times $t \pm \delta t$ given by a Taylor expansion about \mathbf{r}_i ,

$$\mathbf{r}_i(t \pm \delta t) = \mathbf{r}_i(t) \pm \mathbf{v}_i(t)\delta t + \frac{1}{2!}\mathbf{a}_i(t)\delta t^2 \pm \frac{1}{3!}\dot{\mathbf{a}}_i(t)\delta t^3 + \dots \quad (3.8)$$

The central-difference prediction for $\mathbf{r}_i(t + \delta t)$ is obtained by the summation of the two expressions of equation 3.8, ignoring all term greater than or equal to $\mathcal{O}(\delta t^3)$, to give

$$\mathbf{r}_i(t + dt) = 2\mathbf{r}_i(t) - \mathbf{r}_i(t - \delta t) + \mathbf{a}_i(t)\delta t^2. \quad (3.9)$$

Subtracting the two expression of equation 3.8 gives an estimate for the velocity,

$$\mathbf{v}_i(t) = \frac{1}{2\delta t} [\mathbf{r}_i(t + \delta t) - \mathbf{r}_i(t - \delta t)]. \quad (3.10)$$

Despite ignoring higher terms of δt and the introduction of some numerical imprecision, equation 3.10 is simplistic in implementation and symmetrical around $\mathbf{r}_i(t)$, making it time-reversible. More accurate estimates of velocities can be obtained by using the predictor-corrector method at the expense of increased memory storage and complexity of the algorithm (not shown). Alternatively, many modifications to the basic Verlet scheme have been

proposed to address these deficiencies. A common choice is the so-called *half-step leap-frog* scheme which stores the current position $\mathbf{r}_i(t)$, acceleration $\mathbf{a}_i(t)$ and mid-step velocities $\mathbf{v}_i(t - \frac{1}{2}\delta t)$,

$$\mathbf{r}_i(t + \delta t) = \mathbf{r}_i(t) + \delta t \mathbf{a}_i(t + \frac{1}{2}\delta t) \quad (3.11)$$

$$\mathbf{v}_i(t + \frac{1}{2}\delta t) = \mathbf{v}_i(t - \frac{1}{2}\delta t) + \delta t \mathbf{a}_i. \quad (3.12)$$

The velocity equation 3.12 is implemented first such that the velocities leap over the positions to give the next mid-step $\mathbf{v}_i(t + \frac{1}{2}\delta t)$. Subsequently, the position equation is applied to advance the positions to $\mathbf{r}_i(t + \delta t)$ where the $\mathbf{a}_i(t + \delta t)$ are evaluated. Velocity at time t , required to calculate the kinetic energies, can be gained from,

$$\mathbf{v}_i(t) = \frac{1}{2} \left[\mathbf{v}_i(t + \frac{1}{2}\delta t) + \mathbf{v}_i(t - \frac{1}{2}\delta t) \right]. \quad (3.13)$$

3.1.2.2 Rotational motion

Molecular systems typically consist of non-spherical bodies and are not rigid bodies in any sense. If a classical treatment is applied to modelling such molecules, as in some of the early simulations of Harp and Berne [76, 77, 78], the molecular bond vibrations would occur so rapidly that an extremely short simulation time-step δt would be required to solve the equation of motion. More importantly, it is important to choose a time-step suitable for the phenomenon under investigation. A common solution to these problems is to fix the intramolecular bond lengths and simplify the molecule as shown, for example, in Figure 3.1. In classical mechanics, the translation of the centre of mass and rotation about the centre of

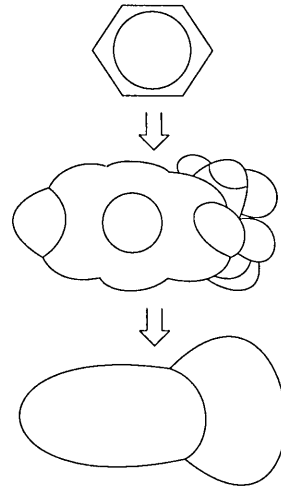


Figure 3.1: Simplification process of ethylbenzene: centre) electron cloud density representation, bottom) ethylbenzene model representation [79]

mass can be regarded separately [74]. Translational motion can be handled by the manner of the previous section 3.1.2.1. Following Allen and Tildesley [15], the rotational motion of a non-linear molecular is governed by the torque τ_i about the centre of mass \mathbf{r}_i which can be regarded as being the vector sum of all intramolecular forces acting on the molecule i ,

$$\tau_i = \sum_{i=1}^a (\mathbf{r}_i^{(a)} - \mathbf{r}_i) \times \mathbf{f}_i^{(a)}. \quad (3.14)$$

For a linear molecule, equation 3.14 simplifies as the angular velocity and the torque must be perpendicular to the unit vector \mathbf{e}_i along the molecule's long axis. Thus the net torque is,

$$\tau_i = \mathbf{e}_i \times \mathbf{g}_i \quad (3.15)$$

where \mathbf{g}_i is determined from the intermolecular potential and for a uniaxial molecular can be replaced by the perpendicular component \mathbf{g}_i^\perp such that,

$$\mathbf{g}_i^\perp = \mathbf{g}_i - (\mathbf{g}_i \cdot \mathbf{e}_i)\mathbf{e}_i. \quad (3.16)$$

The rotational equation of motion can be expressed as two first-order differential equations [80],

$$\dot{\mathbf{e}}_i = \mathbf{u}_i \quad (3.17)$$

$$\dot{\mathbf{u}}_i = \frac{\mathbf{g}_i^\perp}{I} + \lambda \mathbf{e}_i \quad (3.18)$$

where I is the moment of inertia, the term $\lambda \mathbf{e}_i$ is a force along the bond which constrains it to be a unit vector and λ is a Lagrangian multiplier. The molecule i has angular velocity \mathbf{u}_i at times $t \pm \frac{1}{2}\delta t$ is given by a Taylor expansion about $\mathbf{u}_i(t)$ (refer to 3.8),

$$\mathbf{u}_i(t \pm \frac{1}{2}\delta t) = \mathbf{u}_i(t) \pm \frac{1}{2!} \dot{\mathbf{u}}_i(t) \delta t + \frac{1}{3!} \ddot{\mathbf{u}}_i(t) \delta t^2 \pm \dots \quad (3.19)$$

Subtraction of the two expressions of equation 3.19, ignoring all terms greater or equal to $\mathcal{O}(\delta t^3)$, gives

$$\mathbf{u}_i(t + \frac{1}{2}\delta t) = \mathbf{u}_i(t - \frac{1}{2}\delta t) + \dot{\mathbf{u}}_i(t) \delta t. \quad (3.20)$$

The central-difference prediction for $\mathbf{u}_i(t)$ is obtained by the combining equations 3.20 and 3.19 and eliminating $\mathbf{u}_i(t + \frac{1}{2}\delta t)$ to give,

$$\mathbf{u}_i(t) = \mathbf{u}_i(t - \frac{1}{2}\delta t) + \frac{1}{2} \dot{\mathbf{u}}_i(t) \delta t. \quad (3.21)$$

Inserting equation 3.18 into the above equation and taking the dot product of both sides with $\mathbf{e}_i(t)$ gives an equation for the Lagrange multiplier,

$$\lambda\delta t = -2\mathbf{u}_i(t - \frac{1}{2}\delta t) \cdot \mathbf{e}_i(t). \quad (3.22)$$

Leading on from equation 3.20, the integration algorithm used to advance molecule i a full time-step is,

$$\mathbf{u}_i(t + \frac{1}{2}\delta t) = \mathbf{u}_i(t - \frac{1}{2}\delta t) + \frac{\mathbf{g}_{\perp i}(t)}{I}\delta t - 2 \left[\mathbf{u}_i(t - \frac{1}{2}\delta t) \cdot \mathbf{e}_i(t) \right] \mathbf{e}_i(t). \quad (3.23)$$

The step is completed by advancing the unit vector,

$$\mathbf{e}_i(t + \delta t) = \mathbf{e}_i(t) + \mathbf{u}_i(t + \frac{1}{2}\delta t)\delta t. \quad (3.24)$$

3.1.3 Isoenthalpic-Isobaric ensemble, constant-*NPH*

The Verlet algorithm in section 3.1.2 allows simulations to be performed in the microcanonical, or constant-*NVE* ensemble, as used in the simulations of Chapter 4. Although constant volume simulations are generally easy to implement, they do possess a number of disadvantages over ensembles which allow the volume and box shape to vary, for example the isoenthalpic-isobaric ensemble, constant-*NPH*, as used in Chapter 5. In a constant volume simulation, the natural structure of the distribution of constituent molecules may be suppressed in order to be commensurate with the periodic images due to boundary conditions (refer to Section 3.3). Another problem associated with constant volume simulations is that the system cannot change density leading to perhaps metastable phases. For example, it is possible that a crystal may not melt, even at high temperatures, if a high density

is used. A further problem concerns first order transitions such as the isotropic-nematic transition. In the region of phase coexistence, simulation observables, such as the internal energy per particle, are found to be continuous. As a consequence the transition region is hard to locate. In a constant pressure simulation, the phase transition is discontinuous as reflected in the discontinuity of densities (ignoring finite system sizes).

Anderson [81] proposed that the average pressure can be conserved by considering the system in terms of the scaled variables \mathbf{R}_i and $\dot{\mathbf{R}}_i$, both functions of position, \mathbf{r}_i , momentum, \mathbf{p}_i and volume, V ,

$$\mathbf{R}_i = \frac{\mathbf{r}_i}{V^{\frac{1}{3}}} \quad (3.25)$$

$$\dot{\mathbf{R}}_i = \frac{\mathbf{p}_i}{mV^{\frac{1}{3}}}. \quad (3.26)$$

The systems Hamiltonian can then be written as,

$$\mathcal{H}(\mathbf{R}_i, \dot{\mathbf{R}}_i, V, \dot{V}) = \frac{1}{2}V^{\frac{2}{3}} \sum_{i=1}^N m\dot{\mathbf{R}}_i \cdot \mathbf{R}_i + \sum_{i=1}^N \sum_{j \neq i}^N v(r_{ij}V^{\frac{1}{3}}) + \frac{1}{2}M\dot{V}^2 + P_{\text{ext}}V \quad (3.27)$$

where M is a constant and P_{ext} is the external pressure. The first two terms can be considered to be the Hamiltonian of equation 3.1 whereas terms three and four are the kinetic and potential energies associated with the change in volume. A simple physical interpretation of the Hamiltonian equation 3.27 can be given. Suppose a system can be compressed by a piston of mass M which acts upon the fluid to change its volume V in an isotropic fashion. Then, the third term represents the motion of the piston whereas the fourth term is an external pressure acting on the piston.

The coupled Newtonian equations of motion of this system have been given previously by Haile and Graben [82],

$$\ddot{\mathbf{R}}_i = \frac{\mathbf{F}_i}{mV^{\frac{2}{3}}} - \dot{\mathbf{R}}_i \frac{\dot{V}}{V} \quad (3.28)$$

$$\ddot{V} = \frac{(P - P_{\text{ext}})}{M}. \quad (3.29)$$

However, since equation 3.28 contains a term involving $\dot{\mathbf{R}}_i$ it cannot be directly applied to the Verlet leapfrog algorithm. Instead, equation 3.26 is first differentiated with respect to time,

$$\dot{\mathbf{R}}_i = \frac{1}{V^{\frac{1}{3}}} \left(\dot{\mathbf{r}}_i - \frac{1}{3} \mathbf{r}_i \frac{\dot{V}}{V} \right). \quad (3.30)$$

Inserting equation 3.26 gives an equation relating momentum and velocity,

$$\frac{\mathbf{p}_i}{m} = \mathbf{r}_i - \frac{1}{3} \mathbf{r}_i \frac{\dot{V}}{V}. \quad (3.31)$$

Differentiating equation 3.30 with respect to time,

$$\ddot{\mathbf{R}}_i = -\frac{1}{3} \frac{\dot{V}}{V} \dot{\mathbf{R}}_i + \frac{1}{V^{\frac{1}{3}}} \left[\ddot{\mathbf{r}}_i - \frac{1}{3} \dot{\mathbf{r}}_i \frac{\dot{V}}{V} - \frac{1}{3} \mathbf{r}_i \left(\frac{\ddot{V}}{V} - \left(\frac{\dot{V}}{V} \right)^2 \right) \right] \quad (3.32)$$

and substituting equations 3.28 and 3.30 gives,

$$\ddot{\mathbf{r}}_i = \frac{\mathbf{F}_i}{m} + \frac{1}{3} \mathbf{r}_i \left[\frac{\ddot{V}}{V} - \frac{2}{3} \left(\frac{\dot{V}}{V} \right)^2 \right]. \quad (3.33)$$

Prior to integrating the equations of motion, an estimation of the pressure $P(t)$ has to be found to satisfy equation 3.29. Generally the momenta $\mathbf{p}_i(t)$ are needed to calculate the pressure $P(t)$ but these are calculated *after* the integration of particle positions. Following

Brown and Clarke [83], the estimation of pressure $P(t)$ is found from the kinetic contribution to the pressure from the momenta calculated from the previous two time-steps applying the Verlet algorithm to momenta rather than position (ignoring terms $\mathcal{O}(\delta t^2)$ and higher),

$$\mathbf{p}_i(t) = 2\mathbf{p}_i(t - dt) - \mathbf{p}_i(t - 2dt). \quad (3.34)$$

Before integrating the equations of motion, the Verlet algorithm is used to obtain the change in volume,

$$V(t + \delta t) = 2V(t) - V(t - \delta t) + \frac{(P(t) - P_{\text{ext}})}{M} \delta t^2 \quad (3.35)$$

$$\dot{V}(t) = \frac{V(t + \delta t) - V(t - \delta t)}{2\delta t}. \quad (3.36)$$

Finally, the half-step Verlet algorithm of equation 3.12 and equation 3.33 are used to update the velocities,

$$\mathbf{v}_i(t + \frac{1}{2}\delta t) = \mathbf{v}_i(t - \frac{1}{2}\delta t) + \frac{\mathbf{F}_i}{m} + \frac{1}{3}\mathbf{r}_i \left[\frac{\ddot{V}}{V} - \frac{2}{3} \left(\frac{\dot{V}}{V} \right)^2 \right]. \quad (3.37)$$

3.2 Generalised Gay-Berne intermolecular potential

Previous GB simulations have been restricted to mono-disperse systems or mixtures of GB objects and Lennard-Jones spheres. Recently, Cleaver *et al* [17] have proposed a generalised GB (GGB) potential which gives the interaction between two non-identical, anisotropic particles. For cylindrically symmetric but non-identical particles ‘A’ and ‘B’,

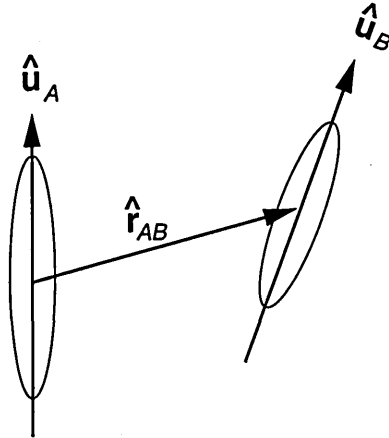


Figure 3.2: Interaction between two non-identical anisotropic particles.

the GGB potential may be expressed in the standard GB form,

$$U(\hat{\mathbf{u}}_A, \hat{\mathbf{u}}_B, \hat{\mathbf{r}}_{AB}) = 4\epsilon(\hat{\mathbf{u}}_A, \hat{\mathbf{u}}_B, \hat{\mathbf{r}}_{AB}) \left[\left(\frac{\sigma_0}{r_{AB} - \sigma(\hat{\mathbf{u}}_A, \hat{\mathbf{u}}_B, \hat{\mathbf{r}}_{AB}) + \sigma_0} \right)^{12} - \left(\frac{\sigma_0}{r_{AB} - \sigma(\hat{\mathbf{u}}_A, \hat{\mathbf{u}}_B, \hat{\mathbf{r}}_{AB}) + \sigma_0} \right)^6 \right] \quad (3.38)$$

but with modified anisotropic range parameter, $\sigma(\hat{\mathbf{u}}_A, \hat{\mathbf{u}}_B, \hat{\mathbf{r}}_{AB})$ and well depth parameter, $\epsilon(\hat{\mathbf{u}}_A, \hat{\mathbf{u}}_B, \hat{\mathbf{r}}_{AB})$.

The modified range parameter is of the form,

$$\sigma(\hat{\mathbf{u}}_A, \hat{\mathbf{u}}_B, \hat{\mathbf{r}}_{AB}) = \sigma_0 \left[1 - \frac{1}{2} \chi \left\{ \frac{(\alpha \hat{\mathbf{r}}_{AB} \cdot \hat{\mathbf{u}}_A + \alpha^{-1} \hat{\mathbf{r}}_{AB} \cdot \hat{\mathbf{u}}_B)^2}{1 + \chi(\hat{\mathbf{u}}_A \cdot \hat{\mathbf{u}}_B)} + \frac{(\alpha \hat{\mathbf{r}}_{AB} \cdot \hat{\mathbf{u}}_A - \alpha^{-1} \hat{\mathbf{r}}_{AB} \cdot \hat{\mathbf{u}}_B)^2}{1 - \chi(\hat{\mathbf{u}}_A \cdot \hat{\mathbf{u}}_B)} \right\} \right]^{-1/2} \quad (3.39)$$

where the new scalar quantity α is defined in terms of the lengths l and breadths d of the two interacting molecular species A and B as,

$$\alpha^2 = \sqrt{\frac{(l_A^2 - d_A^2)(l_B^2 + d_A^2)}{(l_B^2 - d_B^2)(l_A^2 + d_B^2)}} \quad (3.40)$$

and the quantity χ is now given by,

$$\chi = \sqrt{\frac{(l_A^2 - d_A^2)(l_B^2 - d_B^2)}{(l_B^2 + d_A^2)(l_A^2 + d_B^2)}}. \quad (3.41)$$

The role of α is to distinguish between the two independent tee configurations available to a bi-disperse system. The anisotropic well depth function is modified by the introduction of the new parameter α' , and takes the form,

$$\epsilon(\hat{\mathbf{u}}_A, \hat{\mathbf{u}}_B, \hat{\mathbf{r}}_{AB}) = \epsilon_0^{A-B} \epsilon_1^\nu(\hat{\mathbf{u}}_A, \hat{\mathbf{u}}_B) \epsilon_2^\mu(\hat{\mathbf{u}}_A, \hat{\mathbf{u}}_B, \hat{\mathbf{r}}_{AB}) \quad (3.42)$$

where

$$\epsilon_1(\hat{\mathbf{u}}_A, \hat{\mathbf{u}}_B) = [1 - \chi^2(\hat{\mathbf{u}}_A \cdot \hat{\mathbf{u}}_B)^2]^{-1/2} \quad (3.43)$$

and

$$\begin{aligned} \epsilon_2(\hat{\mathbf{u}}_A, \hat{\mathbf{u}}_B, \hat{\mathbf{r}}_{AB}) &= 1 - \frac{1}{2} \chi' \left\{ \frac{(\alpha' \hat{\mathbf{r}}_{AB} \cdot \hat{\mathbf{u}}_A + \alpha'^{-1} \hat{\mathbf{r}}_{AB} \cdot \hat{\mathbf{u}}_B)^2}{1 + \chi'(\hat{\mathbf{u}}_A \cdot \hat{\mathbf{u}}_B)} \right. \\ &\quad \left. + \frac{(\alpha' \hat{\mathbf{r}}_{AB} \cdot \hat{\mathbf{u}}_A - \alpha'^{-1} \hat{\mathbf{r}}_{AB} \cdot \hat{\mathbf{u}}_B)^2}{1 - \chi'(\hat{\mathbf{u}}_A \cdot \hat{\mathbf{u}}_B)} \right\}. \end{aligned} \quad (3.44)$$

The parameter α' is required to enable the two non-equivalent tee configurations to have different well-depths. It should be noted that in the limit $l_A, d_A \rightarrow l_B, d_B$, both α and α' go to unity and the potential reverts smoothly to the original GB form.

3.2.1 GGB parameterisation

The GB potential has traditionally been parameterised with reference to the interaction of sets of Lennard-Jones sites. Following a similar parameterisation route, the

comparison with arrays of discretised sites was found to be an unreliable approach since the potential of two such arrays in a tee configuration reflects the internal structure of the cross-bar molecule. Specifically, the well-depth minimum of a tee configuration shows an odd-even dependence on the number of sites being used to represent that cross-bar molecule. A parameterisation characterised by the differences in its tee configurations was determined to be particularly sensitive to this effect. To avoid this difficulty, the GGB potential was parameterised with reference to the interaction between two Lennard-Jones jellium lines, given by,

$$U_{AB}^{\text{LJ}}(\mathbf{r}_A, \mathbf{r}_B, \hat{\mathbf{u}}_A, \hat{\mathbf{u}}_B) = \varepsilon_0^{\text{LJ}} \int_{\mathbf{r}_B - L_B^{\text{LJ}} \hat{\mathbf{u}}_B}^{\mathbf{r}_B + L_B^{\text{LJ}} \hat{\mathbf{u}}_B} \int_{\mathbf{r}_A - L_A^{\text{LJ}} \hat{\mathbf{u}}_A}^{\mathbf{r}_A + L_A^{\text{LJ}} \hat{\mathbf{u}}_A} \left(\frac{\sigma_0^{\text{LJ}}}{|\mathbf{r}'_A - \mathbf{r}'_B|} \right)^{12} - \left(\frac{\sigma_0^{\text{LJ}}}{|\mathbf{r}'_A - \mathbf{r}'_B|} \right)^6 d\mathbf{r}'_A d\mathbf{r}'_B. \quad (3.45)$$

Where the terms L_A^{LJ} and L_B^{LJ} are half line lengths of the two lines. The parameterisation route is briefly outlined below;

1. Evaluating the separations of two infinite/semi-infinite Lennard-Jones jellium lines, at which the potential is zero for the tee and cross configurations.
2. Equating these separations with the equivalent GGB separations thus obtaining L_A^{LJ} and L_B^{LJ} .
3. Least squares fit parameterisation of the numerical evaluations of equation 3.45 to the unparameterised GGB potential.

3.2.2 Evaluating separations

Assuming infinite Lennard-Jones jellium lines, an analytical evaluation of the separation at repulsion can be determined. A minimum of two configurations are required for Stage 2; tee and cross configurations. The integral for the tee configuration (Figure 3.3) is given by,

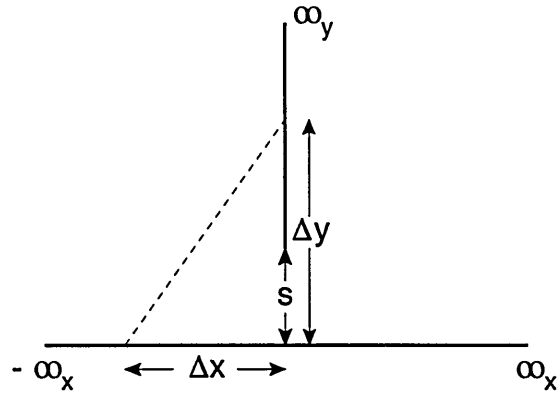


Figure 3.3: Tee configuration of infinite Lennard-Jones and semi-infinite jellium lines.

$$U_{AB}^{\text{Tee}}(x, y) = \int_{-\infty_x}^{\infty_x} \int_s^{\infty_y} \frac{1}{(x^2 + y^2)^6} - \frac{1}{(x^2 + y^2)^3} dx dy. \quad (3.46)$$

Where the inner integral in equation 3.46 has the solution [84] in terms of n ,

$$\int_{-\infty_x}^{\infty_x} \frac{1}{(x^2 + y^2)^n} dx = \frac{\sqrt{\pi} \Gamma(n - \frac{1}{2})}{y^{2n-1} \Gamma(n)}. \quad (3.47)$$

Therefore equation 3.46 simplifies to,

$$U_{AB}^{\text{Tee}}(x, y) = \int_s^{\infty_y} \frac{\sqrt{\pi} \Gamma(5\frac{1}{2})}{y^{11} \Gamma(6)} - \frac{\sqrt{\pi} \Gamma(2\frac{1}{2})}{y^5 \Gamma(3)} dy \quad (3.48)$$

$$= \sqrt{\pi} \int_s^{\infty_y} \frac{63}{256} y^{-11} - \frac{3}{8} y^{-5} dy \quad (3.49)$$

$$= \frac{\sqrt{\pi}}{s^4} \left[\frac{63}{2560} s^{-6} - \frac{3}{32} \right]. \quad (3.50)$$

For the tee configuration, the potential is equal to zero when,

$$s = \left(\frac{21}{80} \right)^{1/6} \sigma_0^{\text{LJ}}. \quad (3.51)$$

Similarly, the integral for the cross configuration (Figure 3.4) is given by,

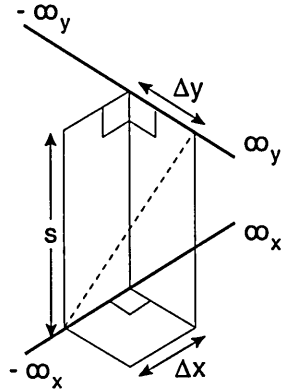


Figure 3.4: Cross configuration of two infinite Lennard-Jones jellium lines.

$$U_{AB}^{\text{Cross}}(x, y) = \int_{-\infty_x}^{\infty_x} \int_{-\infty_y}^{\infty_y} \frac{1}{(x^2 + y^2 + s^2)^6} - \frac{1}{(x^2 + y^2 + s^2)^3} dx dy. \quad (3.52)$$

In terms of n the integral reduces to,

$$\begin{aligned} \int_{-\infty_x}^{\infty_x} \int_{-\infty_y}^{\infty_y} \frac{1}{(x^2 + y^2 + s^2)^n} &= \frac{\sqrt{\pi} \Gamma(n - \frac{1}{2})}{\Gamma(n)} \int_{-\infty_y}^{\infty_y} \frac{1}{(y^2 + s^2)^{n - \frac{1}{2}}} dy \\ &= \frac{\pi \Gamma(n - 1)}{\Gamma(n)} \frac{1}{s^{2n-2}}. \end{aligned}$$

Returning to equation 3.52, evaluation of the integral becomes,

$$U_{AB}^{\text{Cross}}(x, y) = \frac{\pi}{s^4} \left[\frac{1}{5}s^{-6} - \frac{1}{2} \right]. \quad (3.53)$$

For the cross configuration, the potential is equal to zero when,

$$s = \left(\frac{2}{5} \right)^{1/6} \sigma_0^{\text{LJ}}. \quad (3.54)$$

3.2.3 Determination of L_A^{LJ} and L_B^{LJ} .

Equating the equivalent Generalised Gay-Berne separations, where the potential is zero, the lengths L_A^{LJ} and L_B^{LJ} and the scale unit σ_0^{LJ} of equation 3.45 can be determined in terms of σ_0^{GB} . For the cross configuration, taking $\sigma_0^{\text{GB}} = (d_A^2 + d_B^2)^{1/2}$,

$$(\gamma d_A)^2 + (\gamma d_B)^2 = \left(\frac{2}{5} \right)^{1/3} (\sigma_0^{\text{LJ}})^2 \quad (3.55)$$

where γ relates σ_0^{GB} to σ_0^{LJ} units and assuming $d_A = d_B = d$, the Lennard-Jones length parameter is,

$$(\sigma_0^{\text{LJ}})^2 = 2 \left(\frac{2}{5} \right)^{-1/3} (\gamma d)^2. \quad (3.56)$$

A similar approach can be used for the two T_1 and T_2 tee configuration. Equating the T_1 configuration gives,

$$\left[1 + (L_A^{\text{GB}})^2 \right] (\gamma d)^2 = \left[\left(\frac{21}{80} \right)^{1/6} + L_A^{\text{LJ}} \right]^2 (\sigma_0^{\text{LJ}})^2 \quad (3.57)$$

where L_A^{GB} is the half length of the Gay-Berne major axis. Using equation 3.56,

$$\left[1 + (L_A^{\text{GB}})^2 \right] \left(\frac{2}{5} \right)^{1/3} = 2 \left[\left(\frac{21}{80} \right)^{1/6} + L_A^{\text{LJ}} \right]^2 \quad (3.58)$$

the half Lennard-Jones jellium line length is,

$$L_A^{\text{LJ}} = \frac{1}{\sqrt{2}} \left[1 + (L_A^{\text{GB}})^2 \right]^{1/2} \left(\frac{2}{5} \right)^{1/6} - \left(\frac{21}{80} \right)^{1/6}. \quad (3.59)$$

Similarly, for the T_2 configuration, L_B^{LJ} is

$$L_B^{\text{LJ}} = \frac{1}{\sqrt{2}} \left[1 + (L_B^{\text{GB}})^2 \right]^{1/2} \left(\frac{2}{5} \right)^{1/6} - \left(\frac{21}{80} \right)^{1/6}. \quad (3.60)$$

With respect to the l/d ratio of the Gay-Berne molecules for the values $L_A^{\text{GB}} = 3.5$ and $L_B^{\text{GB}} = 3.0$ the two half line lengths are $L_A^{\text{LJ}} = 1.409$ and $L_B^{\text{LJ}} = 1.119$. These separations at repulsion are matched to within 1% for GB molecules with l/d of 2.5 or greater.

3.2.4 Least squares fit.

Since it was expected that the smectic layers would be disrupted in the mixture, a relatively strong side to side intermolecular potential was chosen, with $\mu = 1$ and $\nu = 2$ as used by Luckhurst *et al* [85]. The four remaining variables, α' , χ' , $\epsilon_0^{A-A}/\epsilon_0^{B-B}$ and $\epsilon_0^{A-B}/\epsilon_0^{B-B}$ were determined by performing a least squares fit to curves generated by numerical integration of equation 3.45, subject to the constraint $\epsilon_0^{A-B} = \sqrt{\epsilon_0^{A-A}\epsilon_0^{B-B}}$ (i.e. the Lorentz-Berthelot mixing rule). From this, the remaining values were determined to be $\alpha' = 1.011$, $\chi' = 0.6662$, $\epsilon_0^{A-A}/\epsilon_0^{B-B} = 1.103$. A further constraint which could have been applied was to set the side to side : end to end well depth ratio for mixed interactions to 5, to match the value used for unmixed interactions. In the event, the unconstrained fit gave a value of 4.992 for this ratio. The parameters for the mixed (GGB) and unmixed (GB) interactions that have been used for the studies of Chapters 4 and 5 are summarised in

Table 3.1 where the label **FIT** indicates those values obtained using the parameterisation as described above. Also, this parameterisation of the GGB potential is illustrated for various configurations in Figure 3.5.

	$A-A$ 3.5:1	$B-B$ 3.0:1	$A-B$ mixed	$B-A$
$\sigma_0 = \sqrt{2}d$	1.0	1.0	1.0	1.0
χ	0.849	0.800	0.824	0.824
χ'	0.666 ^r	0.666 ^r	FIT	χ'^{A-B}
ϵ_0	FIT	1.0	$\sqrt{\epsilon_0^{A-A} \epsilon_0^{B-B}}$	ϵ_0^{A-B}
α'	1.0	1.0	FIT	$1/\alpha'^{A-B}$

Table 3.1: Parameter values used for this investigation. Those marked **FIT** were obtained via parameterisation described in this section.

3.3 Periodic boundary conditions

It is impracticable to simulate a real system of the order 10^{23} molecules due to the computational overheads (before even considering the allocation of random access memory). Typical molecular simulations consider 10^2 to 10^4 molecules confined to a geometrical box which is replicated throughout space to form an infinite lattice which overcomes surface effects. This requires the deployment of periodic boundary conditions; as a molecule leaves one face its periodic image enters the opposite face thus conserving the number density (refer to Figure 3.6).

Despite the popularity of periodic boundary conditions there is a well known prob-

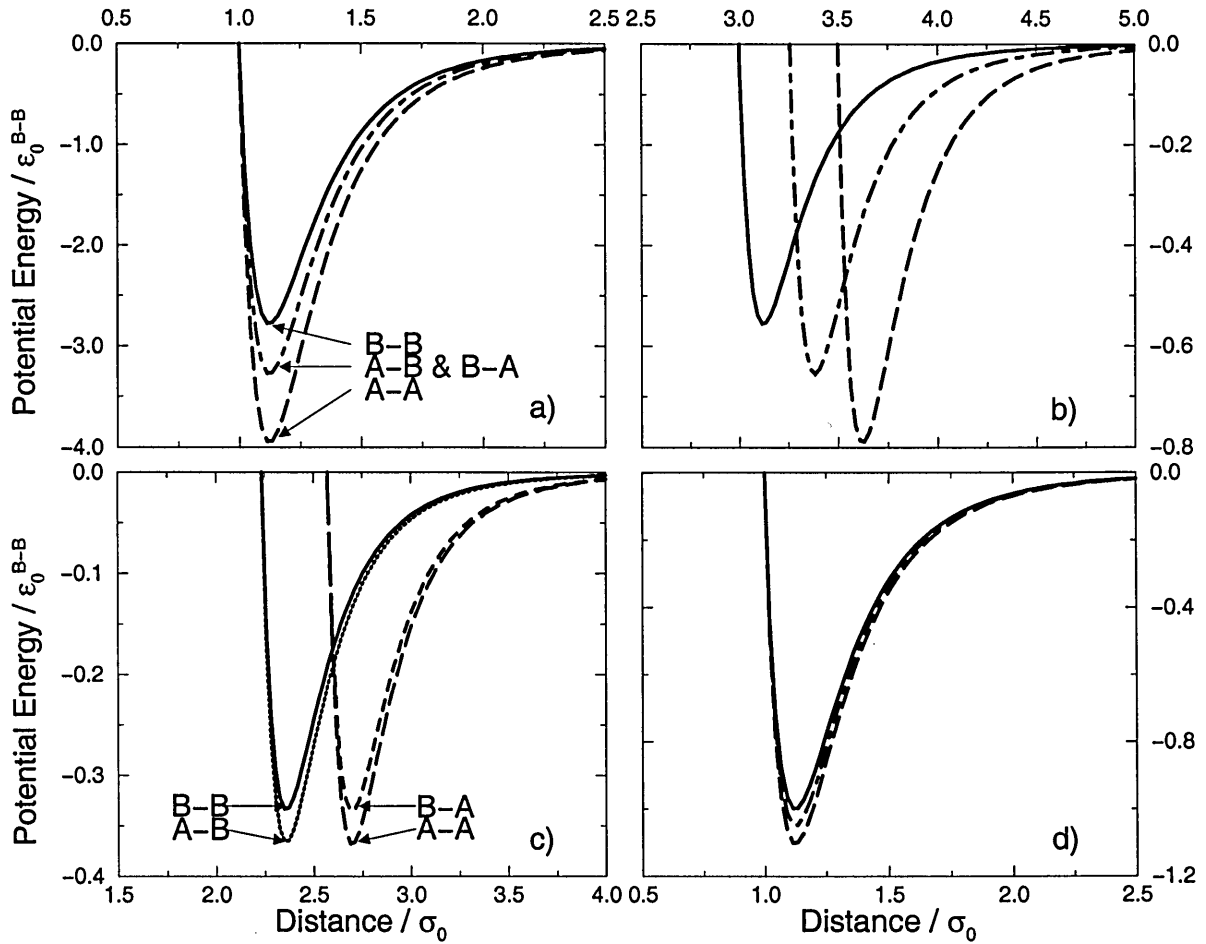


Figure 3.5: Generalised Gay-Berne intermolecular potential between two non-identical anisotropic particles 3.5:1 (molecules *A*) and 3:1 (molecules *B*) for configuration arrangements *a*) side-side, *b*) end-end, *c*) tee and *d*) cross. Molecular species interaction key: *A*-*A* (long dash), *A*-*B* (dotted), *A*-*B* & *B*-*A* (dot dashed), *B*-*A* (dashed) and *B*-*B* (solid).

lem; may the small infinitely periodic system represent the macroscopic system? Obviously this will depend on the phenomenon under investigation and the length scale of the intermolecular potentials employed. Periodic boundary conditions will suppress any density waves greater than the length of the simulation box, for example, at the gas-liquid critical point where the fluctuations range over all length scales. It is also known that first-order transitions under periodic boundary conditions may exhibit the characteristics of higher or-

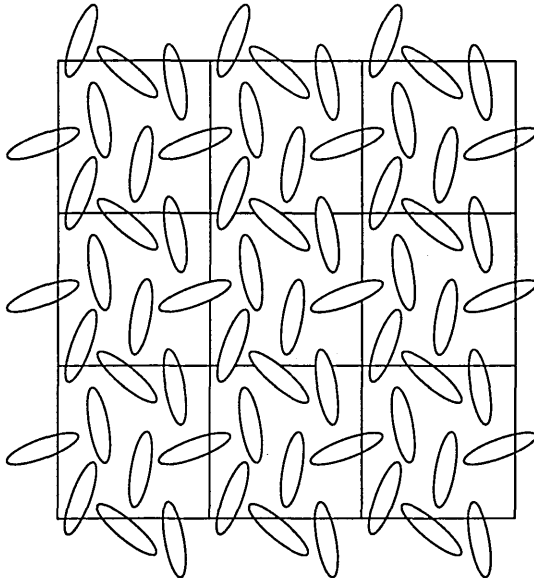


Figure 3.6: 2D representation of periodic boundary conditions. As molecules leave one face its periodic image enters the opposite face.

der transitions. In addition, if the length scale of the intermolecular potential is comparable to the size of the simulation box, for example charged ions or dipolar molecules, then the molecule may ‘sense’ the presence of itself.

3.4 Order parameters and structural properties

3.4.1 Orientational order parameter

Within the field of liquid crystal simulation, probably the most commonly used structural quantity to measure the degree of orientational order of the system is the nematic orientational order parameter S (or simply the ‘order parameter’),

$$S = \frac{1}{N} \left\langle \sum_i \frac{3}{2} (\hat{\mathbf{e}}_i \cdot \hat{\mathbf{d}})^2 - \frac{1}{2} \right\rangle \quad (3.61)$$

where $\hat{\mathbf{e}}_i$ is the unit vector of molecule i and $\hat{\mathbf{d}}$ is the systems director. The order parameter ranges from $\approx N^{-\frac{1}{2}}$ for a system with no orientational order (*i.e.* isotropic) to 1.0 for a perfectly aligned crystal. Following Zannoni [11], the order parameter can be determined by diagonalising the \mathbf{Q} -tensor,

$$\mathbf{Q} = \frac{1}{N} \sum_{i=1}^N \begin{pmatrix} q_i(x, x) & q_i(x, y) & q_i(x, z) \\ q_i(y, x) & q_i(y, y) & q_i(y, z) \\ q_i(z, x) & q_i(z, y) & q_i(z, z) \end{pmatrix} \quad (3.62)$$

where $q_i(x, y)$ is the product of the x and y component direction cosines of molecule i .

Diagonalising equation 3.62 produces three eigenvalues, the largest of which λ_1 is used to evaluate the order parameter,

$$\langle S \rangle = \lambda_1 - \frac{1}{2}(\lambda_2 + \lambda_3) = \frac{1}{2}(3\lambda_1 - 1) \quad (3.63)$$

where $\lambda_1 + \lambda_2 + \lambda_3 = 1$.

3.4.2 Pair distribution functions

Structural information can be gained from a set of distribution functions based on molecular positions. The most simple of these functions is the pair distribution function, $g(r)$, which represents the probability of finding a pair of molecules at distance r apart. The histogram $H(r)$ is compiled of the number of molecules found in concentric shells of radius r and width dr around each particle and normalised against the probability expected for a

completely random distribution at the equivalent density,

$$g(r) = \frac{1}{N} \left\langle \frac{H(r)}{\frac{4}{3}\pi\rho^* [(r+dr)^3 - r^3]} \right\rangle, \quad (3.64)$$

where N is the number of molecules within the whole system and $\langle \rangle$ represents the average over configurations. Typically, the distribution peaks around $r \simeq 1.1\sigma$ corresponding to the first coordination shell. The probability of finding a molecule in subsequent coordination shells diminishes with increasing r . By considering the distances resolved parallel and perpendicular to the director, two additional histograms can be compiled, namely $g_{||}(r)$ and $g_{\perp}(r)$. Here, the appropriate histogram is normalised with respect to the probability of finding a molecule in a slice of the sphere and a cylinder with the difference between two hemispherical caps of radius r and $r+dr$ respectively. Density waves resolved parallel to the director can be revealed in $g_{||}(r)$; isotropic and nematic phases show no significant density waves in contrast to the smectic phase. Coordination shells are readily distinguishable within $g_{\perp}(r)$, more so than $g(r)$.

3.4.3 Bond orientational order parameter

Whereas $g_{\perp}(r)$ reveals the extent of packing within smectic layers it is unable to distinguish between smectic-A and smectic-B; both have hexagonal ordering but the smectic-B phase should show a loss of long range positional order but not of the bond orientational ordering of the hexagonal crystals (refer to Figure 3.7). Correlation of bond orientational order at separation r can be gained from the bond orientational order param-

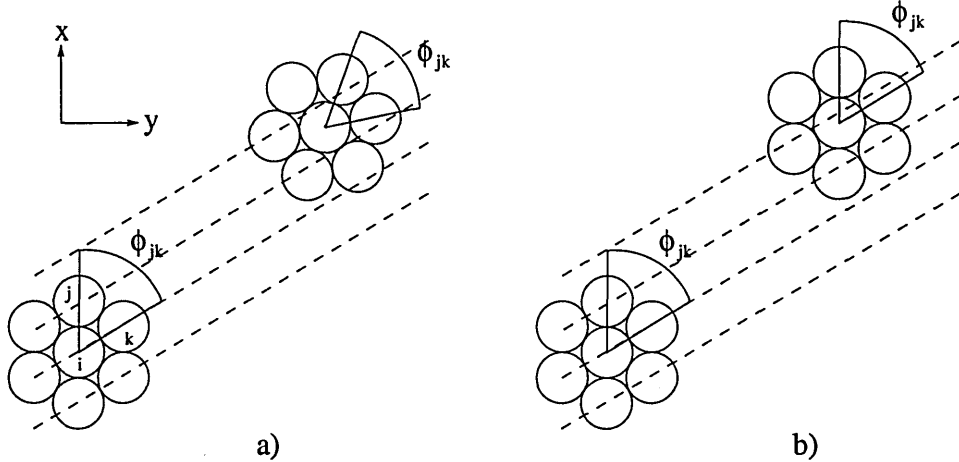


Figure 3.7: Hexagonal crystals at distances r apart within a) smectic-A and b) smectic-B. Both showing a loss of long range positional order but b) has bond orientational order. Note: hexagonal crystals are drawn oversimplified as the packing arrangements within smectic-A and smectic-B layers are only pseudo-hexagonal.

eter $g_6(r)$. A local axis is defined around molecule i , the reference molecule, whose z -axis is parallel to the system's director. The angle ϕ_{jk} (refer to Figure 3.7) makes with the reference molecule i of all (j, k) molecule pairs enclosed within a disk of height $\pm 0.75\sigma_0$ ¹ perpendicular to the director is used to calculate,

$$O_j = \frac{1}{n_j} \sum_{k=1}^{n_j} \cos(6\phi_{jk}) + i \sin(6\phi_{jk}). \quad (3.65)$$

Here n_j is the number of nearest neighbours of molecule j and ϕ_{jk} is defined as

$$\phi_{jk} = \tan^{-1} \left(\frac{y_k - y_j}{x_k - x_j} \right). \quad (3.66)$$

The histogram $H_B(r)$ is compiled for the correlation between bond orientations of molecular pairs between concentric cylinders of width r and $r + dr$ and height $\pm 0.75\sigma_0$ and normalised

¹selected from examination of $g_{||}(r)$

by the number of molecules found within each concentric cylinder N_d ,

$$g_6(r) = H_B(r)/N_d. \quad (3.67)$$

3.4.4 Orientational correlation function

For a system of rigid rod-like molecules, the n^{th} -order orientational correlation function, $G_n(r)$, may be used to describe orientational correlations as a function of separation. It is defined as,

$$G_n(r) = \frac{1}{g(r)} \left\langle \sum_i \sum_{j \neq k} P_n(\cos \gamma_{ij}) \right\rangle \quad (3.68)$$

where $P_n(\cos \gamma_{ij})$ is a Legendre polynomial and γ_{ij} is the angle between the unit vectors $\hat{\mathbf{e}}_i$ and $\hat{\mathbf{e}}_j$. The 2^{nd} -order correlation function is commonly used to characterise long range orientational order in the nematic phase, $P_2(\cos \gamma_{ij})$ being given by $\frac{3}{2}(\hat{\mathbf{e}}_i \cdot \hat{\mathbf{e}}_j)^2 - \frac{1}{2}$.

Chapter 4

Length dispersity study

4.1 Introduction

The review in Chapter 2 illustrated that liquid crystal systems of relevance to device applications are seldom single-component, or mono-disperse, but normally multi-component. Such systems offer an attractive route to material properties otherwise unattainable [47]. However, use of full atomistic or *ab-initio* models to simulate phase behaviour of liquid crystal materials are beyond current computational resources. As with single-component systems, previous models have been simplified to retain only the essential characteristics such as geometrical considerations and “hard” or “soft” intermolecular potentials and still remain accessible via computer simulations.

Previous, hard particle simulations of bidisperse systems have been limited to perfectly aligned spherocylinder [66] and cylinder [86] models. Although these have produced

CHAPTER 4. LENGTH DISPERSITY STUDY

qualitative agreement with the theoretical predictions of Lekkerkerker and co-workers [55, 56, 87, 57] it must be noted that these simulations offer no insight into the effects of free rotation and/or attractive interactions. Computer simulations of bi-disperse systems of soft potentials have considered mixtures of Gay-Berne particles and Lennard-Jones particles [16, 68], or lattice models of various symmetries [88].

There is a considerable volume of published data from simulations of GB particles with a length to breadth axial ratio of 3 to 1. As an initial step in determining the properties of the GGB potential and the effect of length dispersity, this chapter reports a constant-*NVE* molecular dynamics (MD) simulation of a system differing only slightly from this well-characterised 3 to 1 case: a 50:50 mixed system containing GGB rod-like molecules with length to breadth axial ratios of 3 to 1 and 3.5 to 1. This length dispersity was considered to be sufficiently large to induce a change in phase behaviour and/or structural properties. More pronounced difference was avoided since if the length dispersity was too large, that is to say the shapes of the two molecular species were too dissimilar, it might promote phase separation (refer to Frenkel [89]).

A consistent nomenclature for the axial ratios of the two species has been adopted for this and the following chapters viz; molecules *A* refers to long rod-like particles with σ_e/σ_s of 3.5 to 1 and molecules *B* refers to short rod-like particles with σ_e/σ_s of 3 to 1. Order parameters and correlation functions have been calculated over all molecules, *e.g.* $g^{all}(r^*)$, where no distinction is made between molecular species, and over each species

independently, either molecules *A* or molecules *B*, *e.g.* $g^{A-A}(r^*)$ and $g^{B-B}(r^*)$ respectively.

4.2 Simulation details

A molecular dynamics simulation was undertaken in the constant-*NVE* ensemble with 250 GGB rod-like molecules of each species, *i.e.* $N = 500$ molecules in total. One should bear in mind that the MD *NVE* simulations alone are not the best technique for the study of phase transitions without “thermodynamic integration” methods [90] since the system may be forced into metastable states. This investigation must therefore be regarded as an initial investigation in determining the properties of the GGB potential within a mixture of mesogenic molecules. An unequivocal characterisation of the stable states will be addressed by applications of the constant-*NPH* ensemble in the following chapter.

Intuitively, one might expect the smectic layers to be disrupted in the mixture. To prevent phase separation of the smectic phase a relatively strong side to side intermolecular potential was used as of Luckhurst *et al* [85], with $\mu = 1$ and $\nu = 2$. The choice of exponents does not influence the relative well depths of the side-by-side or end-by-end configurations but it is seen that the side-by-side configurations is relatively more stable in comparison to the cross and tee configurations. The remaining GGB parameters are summarised in Table 3.1 of Chapter 3. For both species, the mass m was set to unity and the reduced moment of inertia $I^* = I/\sigma_0^2 = 4.0$. The integration time-step used was $\delta t^* = (\epsilon_0^{B-B}/\sigma_0^2)^{1/2}t = 0.003$. At each state point the system underwent equilibration

and production periods of 20,000 and 25,000 time-steps, respectively. These periods were doubled over the temperature range $2.0 \leq \langle T^* \rangle = \langle k_B T / \epsilon_0^{B-B} \rangle \leq 2.3$. The potential cut-off for both species was $r_c^* = r_c / \sigma_0 = 4.5$. A neighbourhood list was used to save computational time, with a radius of $r_{list}^* = 5.1$. Changes in temperature were achieved by reducing the previous configuration's velocities by 2% for temperatures $\langle T^* \rangle \geq 1.35$ and by 5% for lower temperatures. Preliminary investigations at a reduced density of $\rho^* = \rho \sigma_0^3 = 0.23$ revealed incomplete smectic layers whereas no such problems were observed at $\rho^* = 0.25$ and so this latter density was used thereafter.

4.3 Results and analysis

The computer simulation of the liquid crystal mixture commenced from an isotropic configuration melted from a f.c.c. lattice. The system was cooled through the reduced temperature range $2.5 \geq \langle T^* \rangle \geq 1.0$. Equipartition between the reduced translational and rotational kinetic energies per particle was observed for each state point. Temperature dependencies of several observables are shown in Figure 4.1 and Table 4.1.

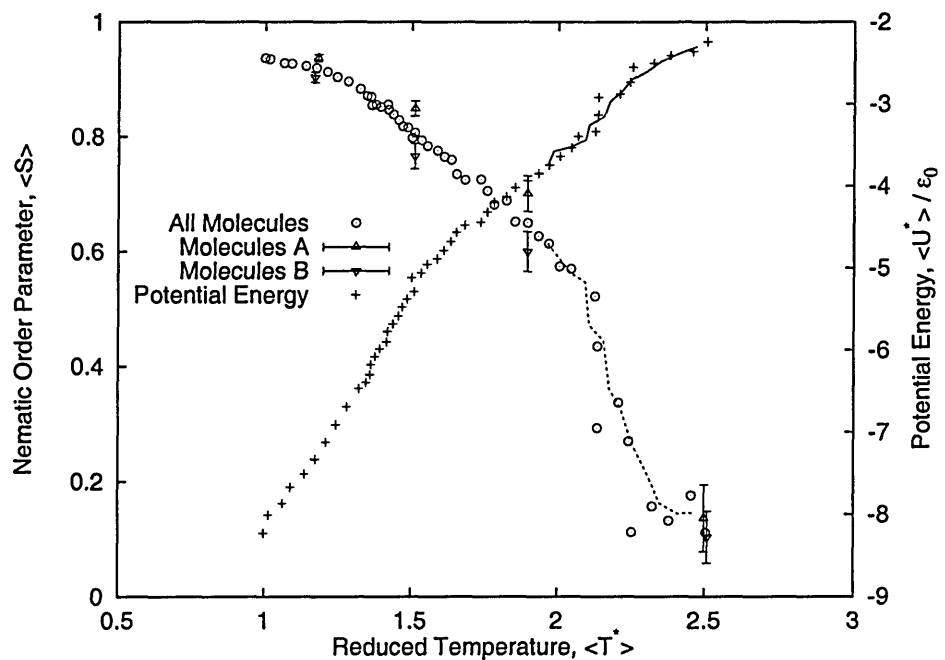


Figure 4.1: Molecular dynamics simulation results for a 50:50 mixture of GGB rods with axial ratios of 3.5:1 (molecules A) and 3:1 (molecules B). Order parameter over all molecules, $\langle S^{all} \rangle$ (o), with corresponding order parameters for $\langle S^A \rangle$ (Δ) and $\langle S^B \rangle$ (∇). Potential energy of all molecules, $\langle U^* \rangle$ (+). In addition, results are shown of subsequent heating cycle for order parameter over all molecules, $\langle S^{all} \rangle$ (- - -) and potential energy of all molecules, $\langle U^* \rangle$ (—).

$\langle T^* \rangle$	$\langle U^* \rangle$	$\langle P^* \rangle$	$\langle S^{all} \rangle$	$\langle S^A \rangle$	$\langle S^B \rangle$	$\langle S^A - S^B \rangle$
2.50(4)	-2.24(10)	4.99(20)	0.11(05)	0.14(06)	0.10(04)	0.033(49)
2.46(4)	-2.36(10)	4.87(19)	0.18(07)	0.20(07)	0.16(07)	0.045(40)
2.38(4)	-2.41(10)	4.70(18)	0.13(04)	0.15(05)	0.12(04)	0.035(41)
2.33(5)	-2.53(12)	4.58(20)	0.18(04)	0.20(04)	0.17(06)	0.037(48)
2.32(4)	-2.50(11)	4.58(18)	0.16(05)	0.18(06)	0.14(06)	0.040(46)
2.25(4)	-2.55(10)	4.45(18)	0.11(04)	0.14(04)	0.10(04)	0.035(42)
2.24(4)	-2.74(10)	4.31(18)	0.27(06)	0.31(08)	0.24(06)	0.069(46)
2.21(5)	-2.88(12)	4.20(18)	0.34(07)	0.39(08)	0.29(06)	0.096(47)
2.13(5)	-2.92(11)	4.06(17)	0.29(08)	0.34(09)	0.25(08)	0.081(50)
2.14(4)	-3.13(10)	3.93(17)	0.43(05)	0.49(05)	0.38(05)	0.108(40)
2.13(4)	-3.34(10)	3.79(18)	0.52(04)	0.58(04)	0.46(05)	0.124(41)
2.07(4)	-3.40(11)	3.66(16)	0.51(06)	0.57(06)	0.45(06)	0.122(37)
2.04(4)	-3.53(10)	3.54(17)	0.57(03)	0.63(03)	0.51(04)	0.114(42)
2.01(4)	-3.64(10)	3.43(16)	0.57(03)	0.64(03)	0.51(04)	0.137(44)
1.97(4)	-3.74(09)	3.30(15)	0.61(03)	0.68(03)	0.55(04)	0.123(38)
1.94(5)	-3.85(13)	3.19(15)	0.63(05)	0.68(05)	0.58(06)	0.095(30)
1.90(4)	-3.94(09)	3.07(16)	0.65(03)	0.70(03)	0.60(04)	0.101(38)
1.85(4)	-4.02(09)	3.00(16)	0.65(02)	0.71(03)	0.60(02)	0.113(28)
1.82(4)	-4.13(09)	2.86(15)	0.69(02)	0.73(02)	0.64(03)	0.090(31)
1.78(4)	-4.20(09)	2.78(15)	0.68(02)	0.74(03)	0.62(03)	0.117(31)
1.76(3)	-4.32(08)	2.67(16)	0.71(02)	0.76(02)	0.66(03)	0.096(28)
1.74(3)	-4.44(08)	2.56(16)	0.73(02)	0.77(02)	0.68(02)	0.090(23)
1.68(4)	-4.48(10)	2.46(14)	0.72(03)	0.77(02)	0.68(04)	0.095(31)
1.65(4)	-4.56(09)	2.40(14)	0.73(02)	0.78(02)	0.69(03)	0.091(29)
1.64(3)	-4.68(08)	2.31(14)	0.76(01)	0.80(02)	0.72(03)	0.082(34)
1.61(4)	-4.79(09)	2.22(15)	0.77(02)	0.81(02)	0.72(03)	0.093(23)
1.59(4)	-4.89(09)	2.15(14)	0.78(02)	0.82(02)	0.74(02)	0.079(23)
1.55(4)	-4.95(10)	2.05(13)	0.78(02)	0.83(02)	0.74(03)	0.083(23)
1.53(4)	-5.06(09)	1.99(13)	0.79(02)	0.83(01)	0.76(02)	0.078(22)
1.50(3)	-5.12(08)	1.90(13)	0.80(01)	0.83(01)	0.76(02)	0.072(20)
1.51(4)	-5.29(09)	1.86(13)	0.81(01)	0.85(01)	0.77(02)	0.083(24)

Table 4.1 *continued...*

$\langle T^* \rangle$	$\langle U^* \rangle$	$\langle P^* \rangle$	$\langle S^{all} \rangle$	$\langle S^A \rangle$	$\langle S^B \rangle$	$\langle S^A - S^B \rangle$
<i>...continuation of Table 4.1</i>						
1.49(4)	-5.38(09)	1.80(13)	0.82(01)	0.86(01)	0.77(02)	0.084(23)
1.47(3)	-5.47(08)	1.75(13)	0.82(01)	0.86(01)	0.78(02)	0.083(20)
1.46(3)	-5.58(08)	1.70(12)	0.83(01)	0.87(01)	0.79(02)	0.076(16)
1.44(3)	-5.68(08)	1.63(12)	0.84(01)	0.88(01)	0.80(02)	0.080(22)
1.42(3)	-5.77(09)	1.58(13)	0.85(01)	0.88(01)	0.81(02)	0.069(23)
1.42(3)	-5.90(07)	1.53(14)	0.86(01)	0.89(01)	0.82(02)	0.064(18)
1.39(3)	-5.99(08)	1.45(12)	0.85(01)	0.90(01)	0.81(02)	0.083(23)
1.38(3)	-6.08(08)	1.43(12)	0.86(02)	0.90(01)	0.82(02)	0.079(24)
1.37(3)	-6.17(08)	1.36(12)	0.85(01)	0.90(01)	0.81(02)	0.088(18)
1.36(3)	-6.30(08)	1.30(12)	0.87(01)	0.91(01)	0.84(02)	0.069(22)
1.35(3)	-6.39(08)	1.27(12)	0.87(01)	0.91(01)	0.83(02)	0.075(20)
1.32(3)	-6.47(07)	1.21(11)	0.88(01)	0.91(01)	0.86(01)	0.053(14)
1.28(3)	-6.69(07)	1.04(11)	0.90(01)	0.92(01)	0.87(01)	0.048(15)
1.24(3)	-6.91(08)	0.88(10)	0.90(01)	0.93(01)	0.88(01)	0.042(12)
1.21(3)	-7.12(08)	0.76(10)	0.91(01)	0.93(01)	0.89(01)	0.038(10)
1.17(3)	-7.33(07)	0.59(11)	0.92(01)	0.94(01)	0.90(01)	0.034(09)
1.14(2)	-7.51(06)	0.46(11)	0.92(01)	0.94(01)	0.90(01)	0.039(09)
1.09(2)	-7.67(06)	0.36(10)	0.93(01)	0.95(00)	0.91(01)	0.041(11)
1.06(2)	-7.87(06)	0.23(10)	0.93(01)	0.95(00)	0.90(01)	0.048(11)
1.01(3)	-8.01(07)	0.07(11)	0.94(01)	0.96(00)	0.91(01)	0.042(10)
1.00(2)	-8.23(06)	0.04(08)	0.94(00)	0.95(01)	0.92(01)	0.035(07)

Table 4.1: Molecular dynamics simulation results of *cooling* a 50:50 mixture of GGB rods with axial ratios of 3.5:1 (molecules *A*) and 3:1 (molecules *B*). Columns key: $\langle T^* \rangle$ reduced temperature, $\langle U^* \rangle$ reduced potential energy per molecule (no long range correction), $\langle P^* \rangle$ reduced pressure (no long range correction), $\langle S^{all} \rangle$ order parameter resolved over all molecules, $\langle S^A \rangle$ molecules *A* order parameter, $\langle S^B \rangle$ molecules *B* order parameter and $\langle S^A - S^B \rangle$ order parameter difference.

An isotropic phase was established at $\langle T^* \rangle = 2.50 \pm 0.04$ with an order parameter resolved over all molecules of $\langle S^{all} \rangle = 0.11 \pm 0.05$. Inspection of pair correlation functions resolved over all directions, $g^{all}(r^*)$ (Figure 4.2), and parallel and perpendicular to the director (Figures 4.3 and 4.4) showed no significant density waves (shown as dashed lines). Furthermore, at $\langle T^* \rangle \geq 2.32$ the second rank orientation correlation function, $\langle G_2^{all}(r^*) \rangle$

$\langle T^* \rangle$	$\langle U^* \rangle$	$\langle P^* \rangle$	$\langle S^{all} \rangle$	$\langle S^A \rangle$	$\langle S^B \rangle$	$\langle S^A - S^B \rangle$
1.97(4)	-3.73(10)	3.31(18)	0.61(03)	0.67(03)	0.56(04)	0.105(33)
1.99(4)	-3.58(10)	3.42(16)	1.99(04)	0.61(04)	0.50(05)	0.109(37)
2.04(4)	-3.52(10)	3.55(16)	0.56(04)	0.62(04)	0.51(05)	0.108(36)
2.09(4)	-3.44(11)	3.66(16)	0.55(05)	0.61(06)	0.49(05)	0.116(37)
2.11(4)	-3.26(10)	3.81(17)	0.47(05)	0.53(05)	0.42(05)	0.113(40)
2.16(4)	-3.16(11)	3.93(17)	0.45(06)	0.50(06)	0.39(06)	0.113(36)
2.17(5)	-2.97(12)	4.09(17)	0.36(07)	0.41(08)	0.31(07)	0.101(53)
2.21(4)	-2.85(11)	4.22(18)	0.33(05)	0.38(06)	0.28(06)	0.102(40)
2.25(4)	-2.70(10)	4.35(18)	0.27(06)	0.31(07)	0.23(06)	0.082(50)
2.30(4)	-2.60(10)	4.48(18)	0.22(08)	0.25(09)	0.19(07)	0.065(44)
2.35(4)	-2.48(11)	4.63(18)	0.16(05)	0.19(06)	0.14(05)	0.044(47)
2.41(4)	-2.39(10)	4.77(18)	0.14(06)	0.16(07)	0.13(06)	0.031(41)
2.47(4)	-2.31(10)	4.92(19)	0.15(05)	0.17(06)	0.14(04)	0.032(45)

Table 4.2: Molecular dynamics simulation results of *heating* a 50:50 mixture of GGB rods with axial ratios of 3.5:1 (molecules *A*) and 3:1 (molecules *B*). Columns key: as of Table 4.1

approached zero at large distances (Figure 4.5). The order parameter spontaneously increased to $\langle S^{all} \rangle = 0.29 \pm 0.08$ at $\langle T^* \rangle = 2.25 \pm 0.05$, with an associated discontinuity in the potential energy. A second increase in order parameter, to a value of $\langle S^{all} \rangle = 0.45 \pm 0.05$, ensued at $\langle T^* \rangle = 2.14 \pm 0.04$. At these temperatures the orientation correlation functions adopted a non-zero limiting values at large distances. Due to the finite systems size, it is irresolvable whether these trends are quasi-long ranged or not. The pursuant heating cycle did not show a similar “double step” transition (Table 4.2 and shown as dashed lines on Figure 4.1). The ambiguity is thought to be related to several interesting phenomena of the *I-N* transition of a mixed system *e.g.* widening of the coexistence region, fractionation effect *etc.* For this system, the *I-N* transition appears to lie in the temperature range

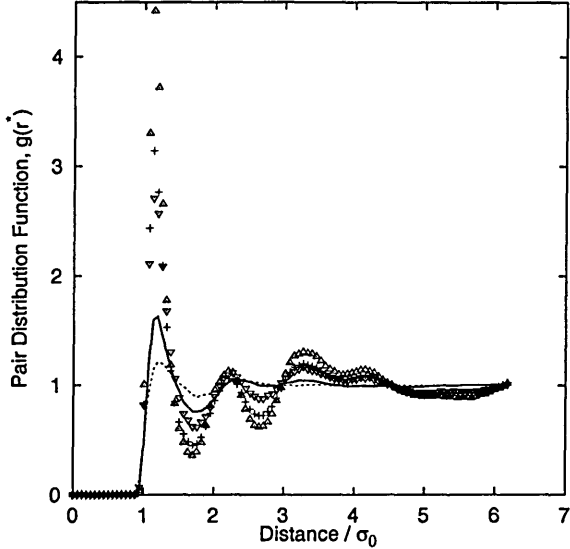


Figure 4.2: Pair distribution functions over all molecules, $g^{all}(r^*)$, in the isotropic phase at $\langle T^* \rangle = 2.5 \pm 0.04$ (- - -), nematic phase at $\langle T^* \rangle = 1.65 \pm 0.04$ (—), smectic phase at $\langle T^* \rangle = 1.32 \pm 0.03$ (+) with corresponding pair distribution functions for $g^{A-A}(r^*)$ (Δ) and $g^{B-B}(r^*)$ (∇).

$2.10 \leq \langle T^* \rangle \leq 2.25$. However, the width of this coexistence region has to be further studied using the Gibbs ensemble [91].

On further cooling over the temperature range $2.0 \geq \langle T^* \rangle \geq 1.5$, $\langle S^{all} \rangle$ increased but the system remained in the nematic phase. The order parameter shows a weak discontinuity at $\langle T^* \rangle = 1.38 \pm 0.02$. Inspection of the potential energy reveals three discontinuities at $\langle T^* \rangle = 1.50 \pm 0.03$, 1.42 ± 0.03 and 1.36 ± 0.03 . At the last of these temperature, strong peaks in $g^{all}(r^*)$ are evident at $r^* = 1.1$, corresponding to a shell of nearest neighbours (Figure 4.2). Equivalently, Figure 4.4 shows peaks in $g_{\perp}^{all}(r^*)$ at $r^* = 1.1$, 2.1 , 3.1 , but there was no significant growth of transverse positional correlation and the system remained liquid like. Below $\langle T^* \rangle < 1.36$, the six-fold in-plane bond orientation correlation function,

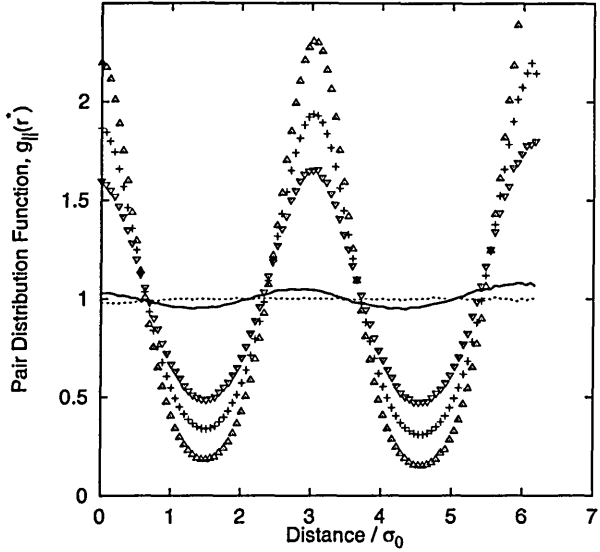


Figure 4.3: Pair distribution functions over all molecules resolved parallel to the director, $g_{\parallel}^{all}(r^*)$, in the isotropic phase at $\langle T^* \rangle = 2.5 \pm 0.04$ (---), nematic phase at $\langle T^* \rangle = 1.65 \pm 0.04$ (—), smectic phase at $\langle T^* \rangle = 1.32 \pm 0.03$ (+) with corresponding pair distribution functions resolved parallel to the director for $g_{\parallel}^{A-A}(r^*)$ (Δ) and $g_{\parallel}^{B-B}(r^*)$ (∇).

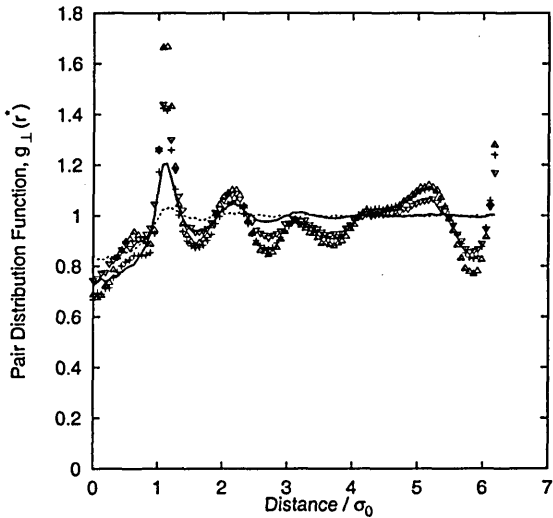


Figure 4.4: Pair distribution functions over all molecules resolved perpendicular to the director, $g_{\perp}^{all}(r^*)$, in the isotropic phase at $\langle T^* \rangle = 2.5 \pm 0.04$ (---), nematic phase at $\langle T^* \rangle = 1.65 \pm 0.04$ (—), smectic phase at $\langle T^* \rangle = 1.32 \pm 0.03$ (+) with corresponding pair distribution functions resolved perpendicular to the director for $g_{\perp}^{A-A}(r^*)$ (Δ) and $g_{\perp}^{B-B}(r^*)$ (∇).

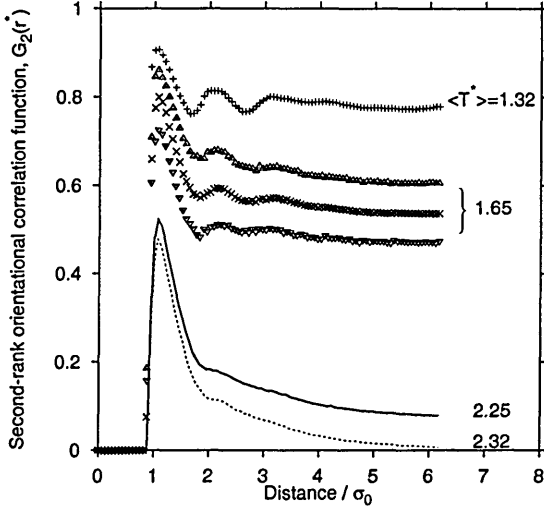


Figure 4.5: Second-rank orientational correlation functions over all molecules, $\langle G_2^{all}(r^*) \rangle$, in the isotropic phase at $\langle T^* \rangle = 2.32 \pm 0.04$ (---), nematic phase at $\langle T^* \rangle = 2.25 \pm 0.06$ (—), smectic phase at $\langle T^* \rangle = 1.32 \pm 0.03$ (+) and pre-smectic region at $\langle T^* \rangle = 1.65 \pm 0.04$ (x) with corresponding second-rank orientational correlation functions for $\langle G_2^{A-A}(r^*) \rangle$ (Δ) and $\langle G_2^{B-B}(r^*) \rangle$ (∇).

$g_6^{all}(r^*)$ adopts a non-zero limiting value at large distances (Figure 4.6) and the existence of layering is apparent from the pair correlation function resolved parallel to the director, $g_{\parallel}^{all}(r^*)$ consistent with the *SmB* phase. As with the *I-N* transition, the *N-SmB* transition is not well defined.

Intriguingly between $1.5 \leq \langle T^* \rangle \leq 1.7$, density waves resolved parallel to the director, $g_{\parallel}^{all}(r^*)$, for the different molecular species are measurable and were found to have the same wavelength although different phases (Figures 4.7). The temperature dependency of the maximum and minimum density waves resolved parallel to the director, shown in Figure 4.8, resemble weak smectic order. The pre-smectic like ordering of the nematic phase is postulated to arise from the competition between the two molecular species of differing

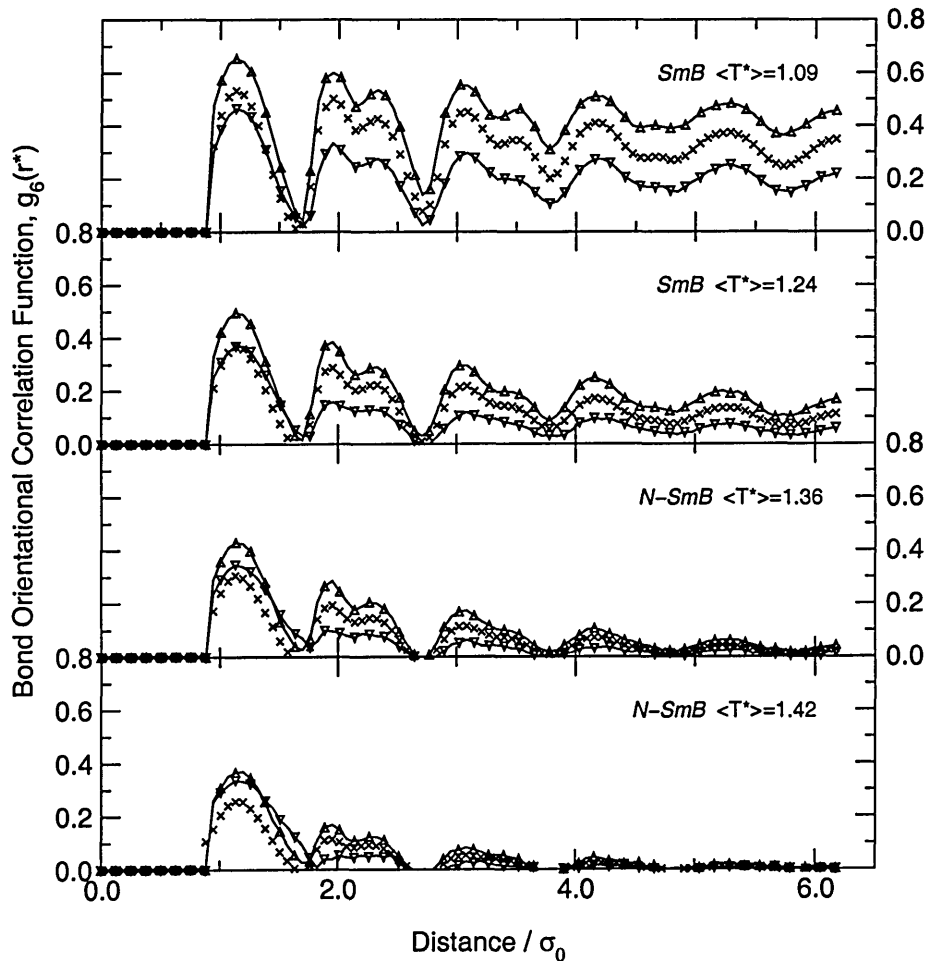


Figure 4.6: Bond orientational correlation function over all molecules, $g_6^{all}(r^*)$ (+), with corresponding bond orientational correlation functions for $g_6^{A-A}(r^*)$ (Δ) and $g_6^{B-B}(r^*)$ (∇).

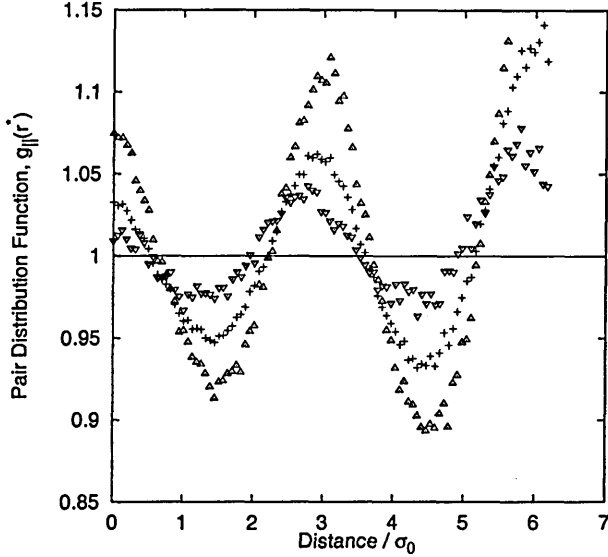


Figure 4.7: Pair distribution function over all molecules resolved parallel to the director, $g_{\parallel}^{all}(r^*)$ with corresponding amplitudes of the pair distribution functions resolved parallel to the director for $g_{\parallel}^{A-A}(r^*)$ (Δ) and $g_{\parallel}^{B-B}(r^*)$ (∇). Pre-smectic region extends over the reduced temperature range $1.5 \leq \langle T^* \rangle \leq 1.7$

lengths. Gruler [25] postulated that this precursor should be accessible by experiment by studying the temperature dependencies of the bend to splay elastic constant ratio, k_{33}/k_{11} . The suppression of the smectic phase to higher densities has been predicted by Mulder [60] and Sluckin [61]. However, from a single simulation, no conclusions regarding suppression of the smectic phase can be drawn. This point will be addressed in the Chapter 5. As the *SmB* transition is approached, the density waves associated with each species move into phase (Figure 4.3).

Throughout the simulation the long molecules have a consistently higher value of $\langle S \rangle$ than the short molecules, as shown in Figure 4.1 and Table 4.9. It is believed that this behaviour is a consequence of the short molecules' greater orientational freedom.

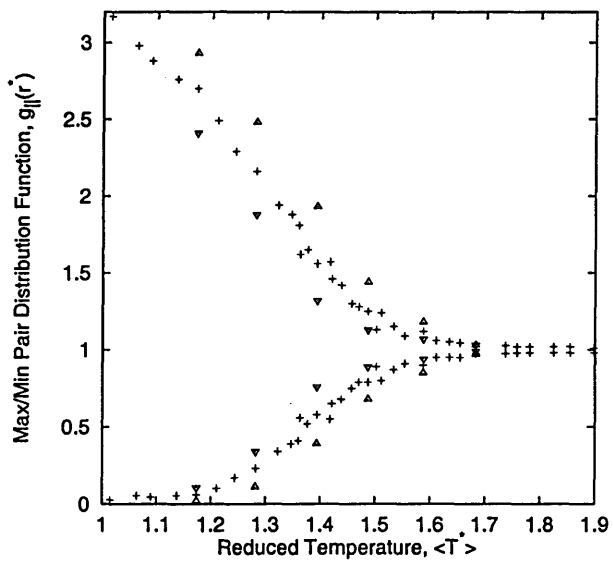


Figure 4.8: Maximum and minimum amplitudes of the pair distribution function over all molecules resolved parallel to the director, $g_{\parallel}^{all}(r^*)$ as a function of reduced temperature, $\langle T^* \rangle$ with corresponding amplitudes of the pair distribution functions resolved parallel to the director for $g_{\parallel}^{A-A}(r^*)$ (Δ) and $g_{\parallel}^{B-B}(r^*)$ (∇). Pre-smectic region extends over the reduced temperature range $1.5 \leq \langle T^* \rangle \leq 1.7$

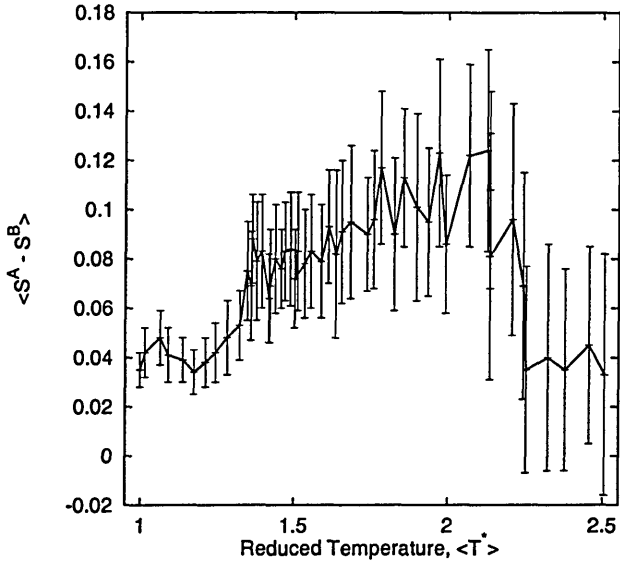


Figure 4.9: Difference between $\langle S^A \rangle$ and $\langle S^B \rangle$ as a function of reduced temperature, $\langle T^* \rangle$.

Indeed, this feature has been predicted by theoretical calculations of Lekkerkerker and co-workers [55, 56, 87, 57] and Sluckin [61]. Nevertheless, these calculations do not predict the behaviour shown in Figure 4.9: the difference in order of the long and short molecules is greatest immediately below the *I–N* transition and then decreases as the smectic region is approached. Theory predicts strong fractionation associated with the *I–N* transition where the long molecules preferentially enter the nematic before the short molecules. Thus it can be inferred the greater difference in order below the *I–N* transition is due to the long molecules driving the system into the nematic phase with the short molecules subsequently ordering within the field of the long molecules.

Correlation function	Coordination number
$g^{A-A}(r^*)$	3.10
$g^{B-B}(r^*)$	2.78
$g^{all}(r^*)$	5.24

Table 4.3: Numerical integration over the first coordination shell within the smectic phase, $\langle T^* \rangle = 1.32$, of the pair distribution function over all molecules, $g^{all}(r^*)$, with corresponding functions for $g^{A-A}(r^*)$ and $g^{B-B}(r^*)$.

For this mixed system no evidence of demixing was observed either within the nematic or smectic phase. Notwithstanding, some evidence of different local ordering between the two molecular species is evident from pair distribution functions, as shown in Figure 4.2. Numerical integration of $4\pi \int_0^{1.7} r^{*2} g(r^*) dr^*$ over the first coordination shell at $\langle T^* \rangle = 1.32 \pm 0.03$ reveals that the nearest neighbour shell of a long molecule is more highly coordinated than that of the nearest neighbour shell of a short molecule (Table 4.3 and 3D visualisation of configuration in Figure 4.10). However, there was strong evidence of demixing in a preliminary investigation of a 50:50 mixed system containing GGB rod-like molecules with length to breadth axial ratios of 3:1 and 4.5:1. Therefore, it can be assumed that the unlike interactions (AB and BA) of the molecules used in this study are not sufficiently dissimilar to promote demixing.

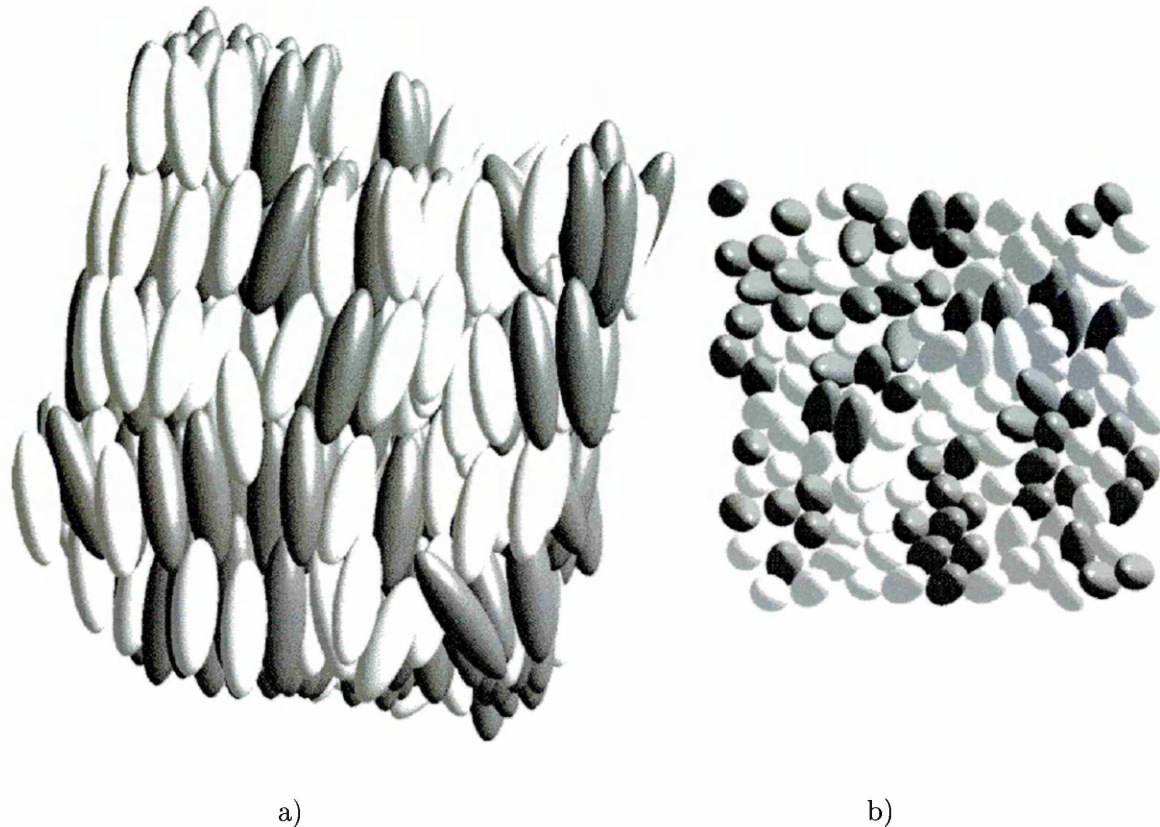


Figure 4.10: Three dimensional visualisation at $\langle T^* \rangle = 1.21 \pm 0.03$ of a) the smectic phase and b) a single smectic layer viewed parallel to the director. Molecular species key: dark particles are 3.5:1 (molecules A) and light particles are 3:1 (molecules B). These show some local compositional ordering within the smectic layers but no evidence of demixing.

4.4 Conclusions

The simulations undertaken involved a 50:50 mixture of Gay-Berne rod-like molecules with axial ratios of 3.5 to 1 and 3 to 1 using the Generalised Gay-Berne intermolecular potential. The results show that the mixture exhibits both nematic and smectic-B phases, with the *I–N* phase boundary not clearly defined. Throughout the simulations, the long molecules had a consistently higher order parameter than that of the short molecules, consistent with theoretical and experimental behaviour. The difference between these order parameters was greatest just below the nematic transition and then decreased with decreasing temperature. The *N–SmB* transition was preceded by a relatively wide pre-smectic region identified by resolving $g_{||}(r^*)$ for the individual species. This extended pre-smectic region appeared to be associated with the competition between the two different density waves of the same wavelength but different phase. The smectic phase was fully commensurate and no evidence of demixing was observed albeit the long molecules possessed a higher degree of local ordering. The results indicate that the Generalised Gay-Berne intermolecular potential offers a viable and computationally efficient route to the study of multicomponent and even polydisperse systems.

Clearly, this simple model has also presented some unresolved questions: namely, to what extent does the use of the constant-*NVE* thermodynamic ensemble affect the phase behaviour. Thus, an unequivocal characterisation of stable states cannot be fully resolved. Moreover, many phenomena associated with mixed systems (such as the concentration,

CHAPTER 4. LENGTH DISPERSITY STUDY

width of the I - N coexistence region, fractionation effect *etc*) are inaccessible with this ensemble. In the next chapter, therefore, an ensemble permitting adiabatic volume and energy fluctuations was employed to address these concerns.

Chapter 5

Concentration and pressure study

5.1 Introduction

In chapter 4 results were presented for a 50:50 mixture of 3.5:1 and 3:1 molecules within the microcanonical, constant-*NVE*, ensemble to study the effect of length dispersity. It was shown that a finite length dispersity leads to a more complicated phase diagram than that of a homogeneous system. The results of chapter 4 have been limited to a fixed molar concentration of two components. In this chapter the the phase behaviour of liquid crystal mixtures is expanded to include an addition inherent degree of freedom, namely concentration. To facilitate this it is necessary to undertake these simulation studies within an ensemble permitting adiabatic volume and energy fluctuations. For this study the isoenthalpic-isobaric, constant-*NPH* ensemble¹ was chosen thus enabling a more meaningful

¹Another candidate is the isothermal-isobaric, constant-*NPT*, ensemble. The construction of such ensemble involves combining the constant-*NVT* and constant-*NPH* schemes.

CHAPTER 5. CONCENTRATION AND PRESSURE STUDY

comparison of simulations performed at different concentrations and equal pressures.

This chapter is divided in two studies, each study comprising of a series of simulations. First, results are presented detailing the influence of pressure on the phase behaviour of liquid crystals at a constant mole fraction of $\chi_A = 0.5$ (section 5.2). Following this, in section 5.3 the determination of phase behaviour and structural properties of liquid crystal over a range of mole fractions is presented.

For ease of reading, a number of tables of observable averages are confined to Appendix A and B owing to the number of simulations.

5.2 Influence of pressure

The influence of pressure on the phase behaviour of liquid crystals has long been known experimentally. Both the nematic-smectic and isotropic-nematic transition temperatures increase by raising the system pressure; a pressure induced mesomorphism. Moreover, the slope dT_{I-N}/dP for the latter is greater which equates to a wider nematic phase at elevated pressures. The location of a wide nematic range would be beneficial for the study of the effect of concentration. There are a limited number of papers in the literature which report widening of the nematic phase under the influence of adiabatic volume fluctuations. Of these papers, Hashim *et al* [92] remarked on the lack of a nematic phase in a system of homogeneous 3:1 Gay-Berne molecules at a reduced pressure of $\langle P^* \rangle \leq 1.0$. Meanwhile, Mills and Cleaver [91] reported a small widening of a nematic phase in a sys-

CHAPTER 5. CONCENTRATION AND PRESSURE STUDY

tem of 2:1 and 2.5:1 Generalised Gay-Berne molecules over a reduced pressure range of $0.5 \leq \langle P^* \rangle \leq 2.0$. Similarly, in a recent paper Bates [93] reports a widening of the nematic phase over $1.0 \leq \langle P^* \rangle \leq 2.0$ for a homogeneous system of 4.4 Gay-Berne molecules with a novel intermolecular potential Gay-Berne parameterisation. More extensive studies of the dependence of the phase behaviour of homogeneous systems upon molecular length [94] and intermolecular strength [95] has been reported by de Miguel and co-workers. They report the growth of a stable *SmA island* in the phase diagrams of molecular lengths above 3:1.

The primary aim of this section is to select an appropriate reduced pressure from analysis of $\langle T^* \rangle$ vs. $\langle \rho^* \rangle$ and $\langle P^* \rangle$ vs. $\langle T^* \rangle$ phase behaviour diagrams which is then used for the subsequent concentration study. The secondary aim is to answer the following question; is there a stable *SmA* phase in a mixture of 3.5:1 and 3:1 molecules? In keeping with the previous chapter, the same choice of Gay-Berne exponents were used. To this end, a series of simulations at different reduced pressures were undertaken. Each simulation consisted a 50:50 mixtures of 3.5:1 and 3:1 rod-like molecules (total of $N = 500$), as in chapter 4, within the isoenthalpic-isobaric, constant-*NPH*, ensemble where the reduced pressure was taken to be one of the following values $\langle P^* \rangle = 1.0, 2.0, 3.0, 4.0$ or 5.0 .

5.2.1 Simulation details

The constant-*NPH* ensemble can be constructed from a combination of isoenthalpic and isothermal constraints, as described in chapter 3. For both species, the mass, m , was set to unity, and the reduced moment of inertia, $I^* = I/\sigma_0^2 = 4.0$, whilst the Gay-

Berne exponents were $\mu = 1$ and $\nu = 2$. The remaining GGB parameters are summarised in Table 3.1 of chapter 3. The potential cut-off was $r_c^* = r_c/\sigma_0 = 4.5$ and a neighbourhood list, of radius $r_{nlist}^* = 5.1$, was used to save computational time. The integration time-step was $\delta t^* = (\epsilon_0^{B-B}/\sigma_0^2)^{1/2}t = 0.003$. The external mass of the piston of $M^* = M\sigma_0^4 m^{-1} = 0.0019$ was arrived at from preliminary investigations where the frequencies of volume fluctuations were approximately equal to those of pressure fluctuations in a constant-*NVE* system [82].

5.2.2 Onset of orientational order, T_{I-N}

Each series of simulations commenced with the molecules *A* and *B* distributed randomly on an f.c.c. lattice at a reduced density of $\langle \rho^* \rangle = 0.17$. A relatively high reduced temperature of $\langle T^* \rangle = 3.0$ was employed for each simulation to melt the molecules off the lattice. The order parameters for individual simulations decreased to values of typically $\langle S \rangle \simeq 0.1$. Each simulation was identified to be within an isotropic phase from examination of the pair distribution functions resolved in all directions, $g^{all}(r^*)$ and parallel to the director, $g_{||}^{all}(r^*)$ which revealed no significant density waves. The second-rank orientational correlation function, $\langle G_2^{all}(r^*) \rangle$ was found to decay to zero at large distances thereby establishing an isotropic phase at each pressure.

The onset of orientational order was signified by sizeable time-scale fluctuations of the order parameter, reduced density and reduced potential energy. Extended equilibration periods of typically 500,000 time-steps were required, proceeded by production runs of equal magnitude. Away from a transition, the distribution of an observable, \hat{O} , will have a

CHAPTER 5. CONCENTRATION AND PRESSURE STUDY

single (near-Gaussian) peak, $\Phi(\hat{O})$. For real systems of infinite size first-order transition are characterised by discontinuities in the first derivative of the free energy leading to δ -function singularities in the specific heat. However, for simulations such singularities do not occur due to the finite system size leading to finite peak height in the specific heat and the shift of the location of the maxima in a size dependent fashion. Although the specific heat is not calculated for this study, the fluctuations of the reduced potential energy diverged at the onset of orientational order. Close to first-order transitions the distribution $\Phi(\hat{O})$ will closely represent two overlapping Gaussians [96] where the system samples both phases either side of the transition. Following the analysis of Berardi *et al* [97], normalised histograms of the order parameter S were constructed to study the long time-scale orientational fluctuations. For ease of interpretation only the analysis of the simulation carried out at a reduced pressure of $\langle P^* \rangle = 4.0$ is presented in Table 5.1 and Figure 5.1. (Similar histogram analysis was performed on each simulation in the pressure study series). In common with the results presented in chapter 4 for the 50:50 mixtures within the constant-*NVE*, long molecules have a consistently higher value of $\langle S \rangle$ than the short molecules as a consequence of the short molecules' greater orientational freedom.

The skewness and kurtosis characterises the degree of asymmetry of the distribution around its mean. Close to a transition the distribution $\Phi(O)$ would be expected to be skewed towards the transition reflected in a positive value of skewness (3^{rd} moment). For this to be meaningful, the degree of skewness should be several times larger than *its*

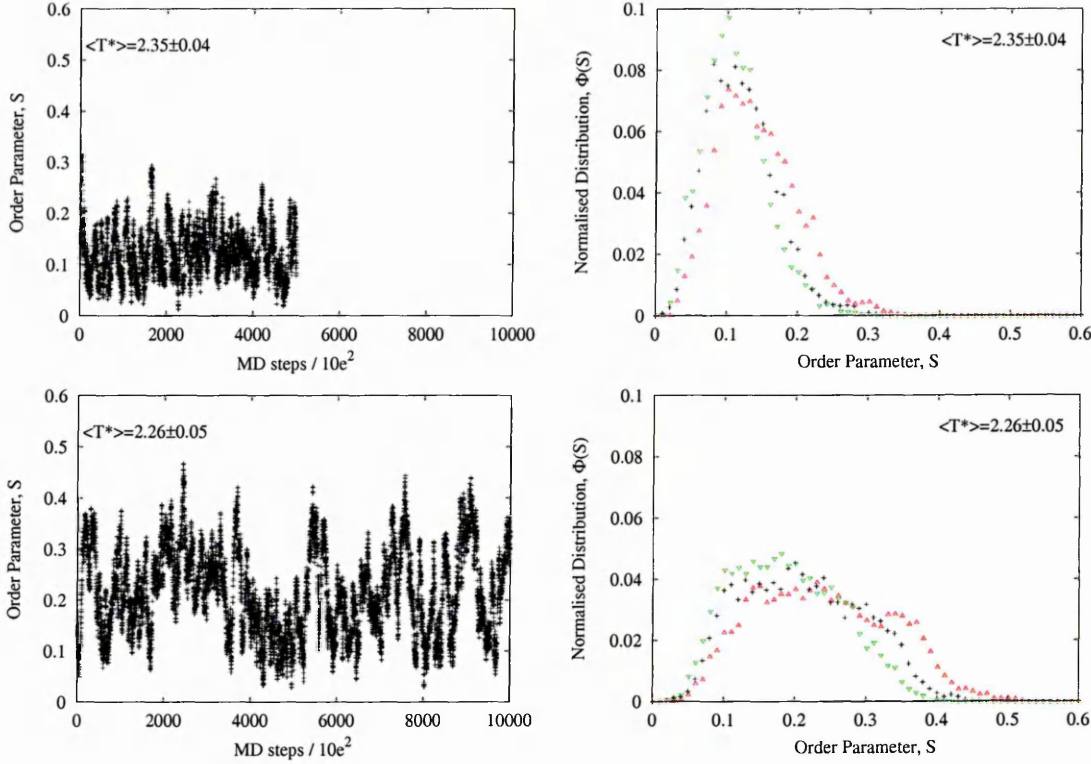


Figure 5.1: Order parameter evolution (left column) and normalised distribution functions (right column) for a 50:50 mixture of GGB rods with axial ratios of 3.5:1 (molecules *A*) and 3:1 (molecules *B*) and reduced pressure of $\langle P^* \rangle = 4.0$. Order parameter resolved over all molecules $\langle S \rangle$ (+), $\langle S^A \rangle$ (Δ) and $\langle S^B \rangle$ (∇).

standard deviation. In practice this can be judged by comparing the skewness to the standard deviation of the skewness of an idealised Gaussian distribution, which is approximately $\sqrt{15/N_S}$ where N_S is the number of samples. Similarly, the kurtosis needs to be several times larger than that of the standard deviation of the kurtosis of an idealised Gaussian distribution, which is approximately $\sqrt{96/N_S}$. Both estimates are presented in Table 5.1. At $\langle T^* \rangle = 2.35 \pm 0.04$ there is some, but not conclusive, evidence of two overlapping peaks in $\Phi(S^A)$ and $\Phi(S^B)$. Both distributions are skewed towards values typical of orientational

CHAPTER 5. CONCENTRATION AND PRESSURE STUDY

ordering although care has to be taken in the interpretation since the the distribution is limited to $0.0 \leq \Phi(S) \leq 1.0$. Upon cooling to $\langle T^* \rangle = 2.26 \pm 0.05$ orientational ordering was observed although not persisting indefinitely. The equilibrium period was extended to 1,000,000 time-steps in an attempt to study the long time-scale fluctuations. The $\Phi(S)$ distribution widened considerably, as reflected in a negative kurtosis, and there is some evidence of overlapping peaks. Further extensive runs are required to resolve the nature of the peaks. Upon further cooling to $\langle T^* \rangle = 1.98 \pm 0.04$ the order parameter and density spontaneously increased with an associated discontinuity in potential energy which is characteristic of a first-order transition. The fluctuations of these observables was observed to be persistent and the phase was identified as nematic from the inspections of a non-zero limiting value of $\langle G_2^{all}(r^*) \rangle$ at large distances and the absence of significant density waves within $g_{||}^{all}(r^*)$. Fluctuations in the reduced potential energy aided the location of the $I-N$ transition temperatures and are presented in Table 5.2. Nematic ordering was observed upon cooling each of the remaining simulations.

5.2.3 Higher ordered phase and metastability, T_{N-Sm}

The temperature and pressure dependencies of $\langle S \rangle$, $\langle \rho^* \rangle$ and $\langle U^* \rangle$ are displayed in Tables A.1 through to A.5, Table 5.2 and within Figures 5.2, 5.3, 5.4, and 5.5. Before embarking on a qualitative discussion of the nematic phase temperature range, the T_{N-Sm} phase boundaries are discussed in this section and their approximate locations are super-

CHAPTER 5. CONCENTRATION AND PRESSURE STUDY

Reduced Temperature	Order Parameter	Mean	Mean Deviation	Variance	$\frac{\text{Skewness}}{\sqrt{15/N_S}}$	$\frac{\text{Kurtosis}}{\sqrt{96/N_S}}$
$\langle T^* \rangle = 2.35 \pm 0.04$	$\langle S^{all} \rangle$	0.124	0.039	0.002	10.61	2.03
	$\langle S^A \rangle$	0.146	0.045	0.003	9.81	0.41
	$\langle S^B \rangle$	0.115	0.036	0.002	11.87	4.17
$\langle T^* \rangle = 2.26 \pm 0.05$	$\langle S^{all} \rangle$	0.216	0.070	0.007	2.80	-6.46
	$\langle S^A \rangle$	0.244	0.078	0.009	2.97	-6.03
	$\langle S^B \rangle$	0.193	0.062	0.006	4.16	-5.81

Table 5.1: Histogram analysis of long time-scale orientational fluctuations close to the onset of orientational order for simulation at a reduced pressure of $\langle P^* \rangle = 4.0$ (Refer to Figure 5.1). Where the number of samples $N_S = 5000$ for $\langle T^* \rangle = 2.35 \pm 0.04$ and $N_S = 10,000$ for $\langle T^* \rangle = 2.26 \pm 0.05$, each sample equivalent to 100 MD steps.

imposed on the various phase behaviour diagrams to aid the eye. This section is further subdivided into two sub-sections; $1.0 \leq \langle P^* \rangle \leq 3.0$ (section 5.2.3.1) and $4.0 \leq \langle P^* \rangle \leq 5.0$ (section 5.2.3.2).

Before discussing the phase behaviour diagrams, a salient feature of these diagrams is the behaviour of the each simulation at high order parameter, $\langle S \rangle \approx 0.9$. Close to first-order transitions a small system may experience van de Waals heating as a consequence of the system entering a metastable phase space region. A schematic diagram showing the temperature and volume relationship² and corresponding Gibbs free energy as a function of temperature for a first-order transition at constant pressure is shown in Figure 5.6. The line traced out by ABCDE represents the coexistence region where the Gibbs free energy of the two phase are equal. Points B and D present the limits of metastability whereas

²The standard thermodynamics literature commonly report pressure and volume relationship with isotherms of constant temperature. Figure 5.6 schematic was based on evaluating the van de Waals equation at constant temperature with isobars of constant pressure.

Transition	Pressure $\langle P^* \rangle$	Temperature $\langle T^* \rangle$	Transition ratio T_{N-SmA}/T_{I-N}	Density $\langle \rho^* \rangle$	Energy $\langle U^* \rangle$
$I-N$	1.0	1.39(03)	-	0.203(001)	-3.56(06)
	2.0	1.73(04)	-	0.223(001)	-3.53(08)
	3.0	1.98(04)	-	0.242(001)	-3.97(08)
	4.0	2.22(05)	-	0.248(001)	-3.53(10)
	5.0	2.46(05)	-	0.255(001)	-3.34(11)
$N-SmA$	1.0	1.33(03)	0.96	0.233(002)	-5.55(07)
	2.0	1.50(03)	0.87	0.259(001)	-6.15(00)
	3.0	1.61(04)	0.81	0.275(001)	-6.55(08)
	4.0	1.73(04)	0.78	0.284(001)	-6.40(09)
$SmA-SmB$	1.0	1.28(03)	-	0.249(002)	-6.93(07)
	2.0	1.44(03)	-	0.273(001)	-7.64(07)
	3.0	1.59(04)	-	0.284(001)	-7.62(10)
	4.0	1.63(04)	-	0.292(001)	-7.34(08)
$N-SmB$	5.0	1.80(06)	-	0.298(001)	-7.31(14)

Table 5.2: Approximate location of T_{I-N} , T_{N-SmA} , $T_{SmA-SmB}$ transition temperature and estimations of the nematic-smectic-A transition strength [98] over the reduced pressure range $1.0 \leq \langle P^* \rangle \leq 5.0$.

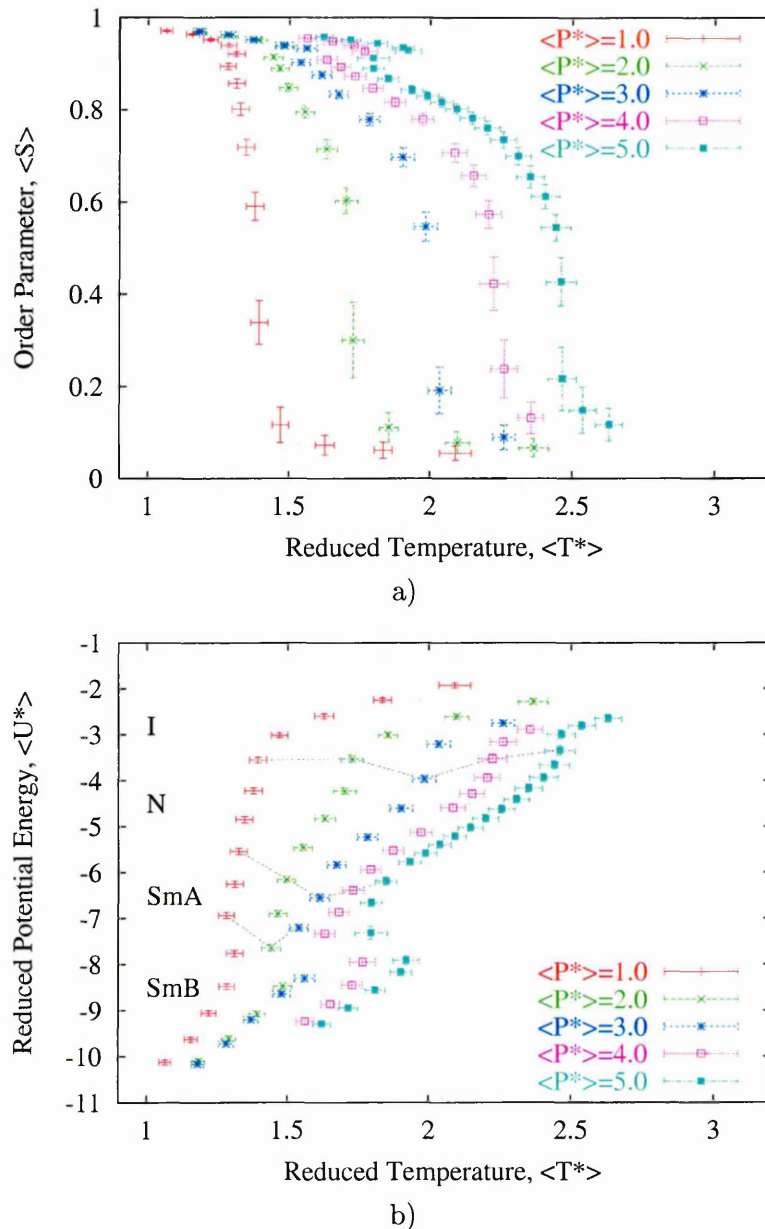


Figure 5.2: Temperature dependencies of a) order parameters, $\langle S^{all} \rangle$ and b) reduced potential energy, $\langle U^* \rangle$ of constant-*NPH* molecular dynamics simulations for 50:50 mixtures of GGB rods with axial ratios of 3.5:1 (molecules A) and 3:1 (molecules B) over reduced pressure range $1.0 \leq \langle P^* \rangle \leq 5.0$. Approximate location of phase boundaries are shown.

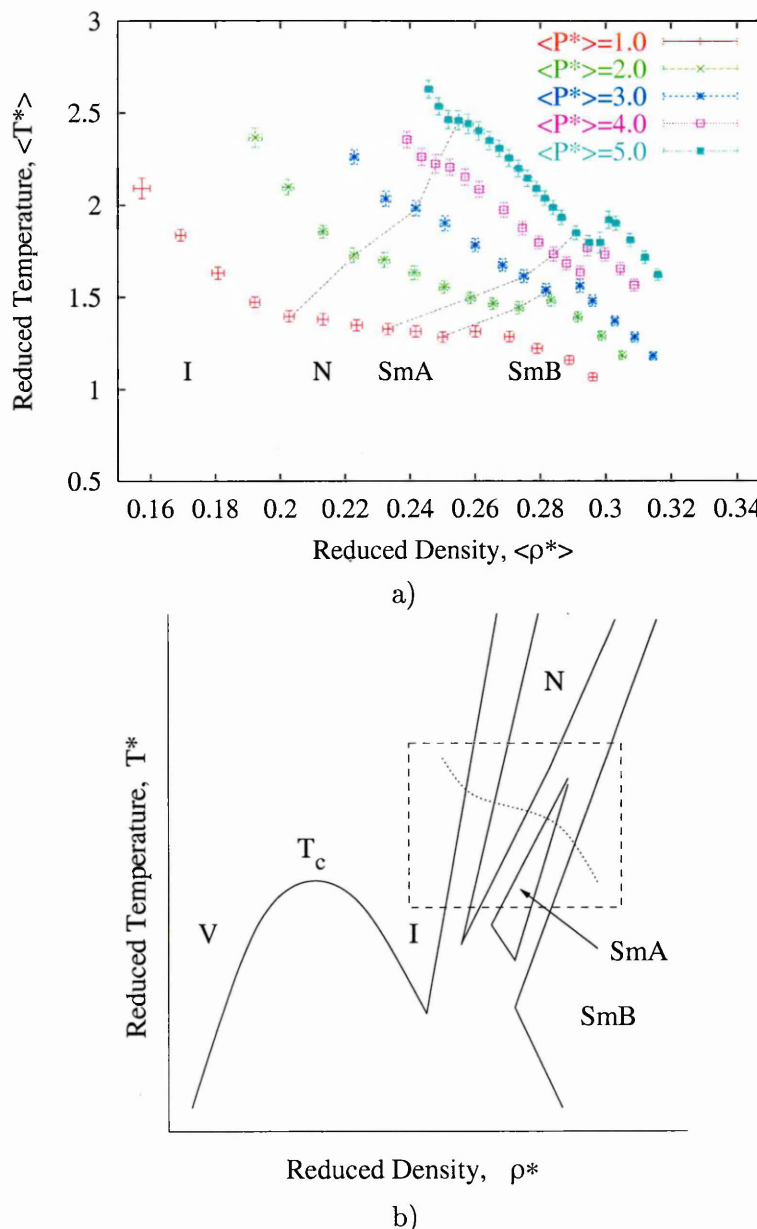


Figure 5.3: Temperature dependencies of a) reduced densities, $\langle \rho^* \rangle$ for mole fraction $\chi_A = 0.5$ over reduced pressure range $1.0 \leq \langle P^* \rangle \leq 5.0$ and b) schematic representations of $\langle T^* \rangle$ vs. $\langle \rho^* \rangle$ phase diagram of GB fluid.

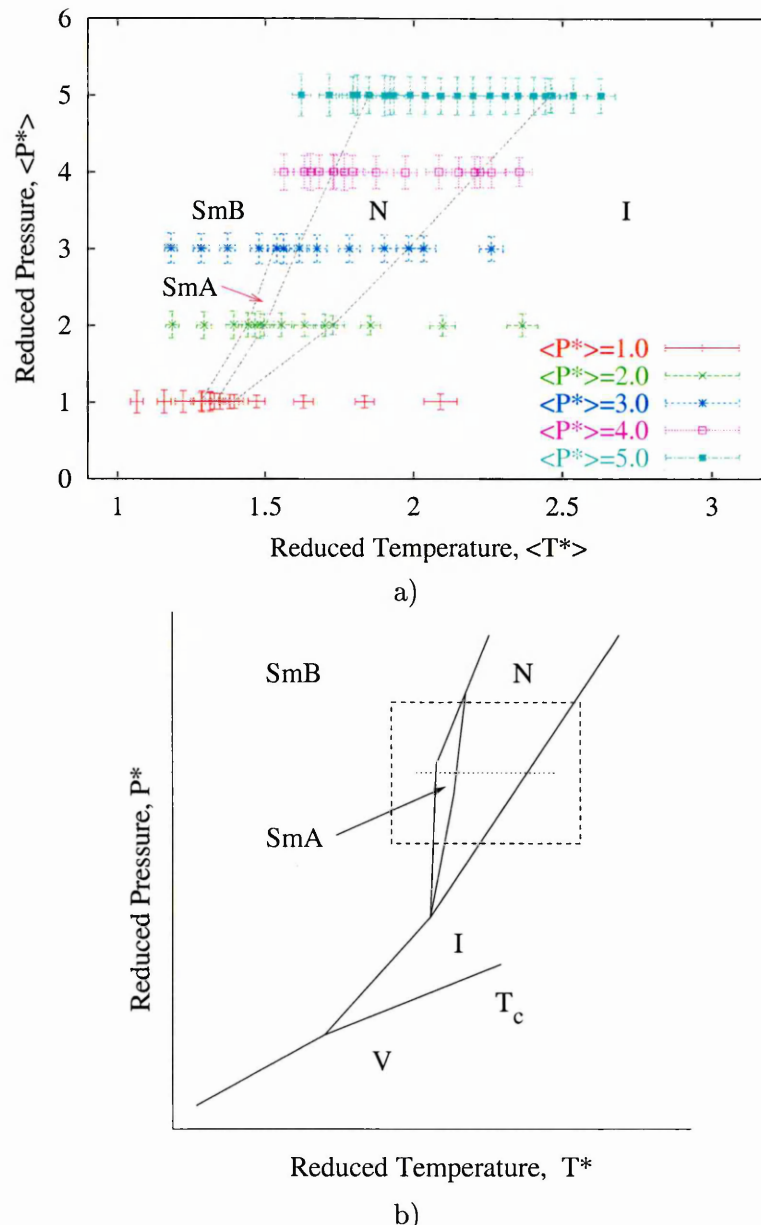


Figure 5.4: Temperature dependencies of a) reduced densities, $\langle \rho^* \rangle$ for mole fraction $\chi_A = 0.5$ over reduced pressure range $1.0 \leq \langle P^* \rangle \leq 5.0$ and b) schematic representations of $\langle P^* \rangle$ vs. $\langle T^* \rangle$ phase diagram of GB fluid and isobar of traced out by simulation.

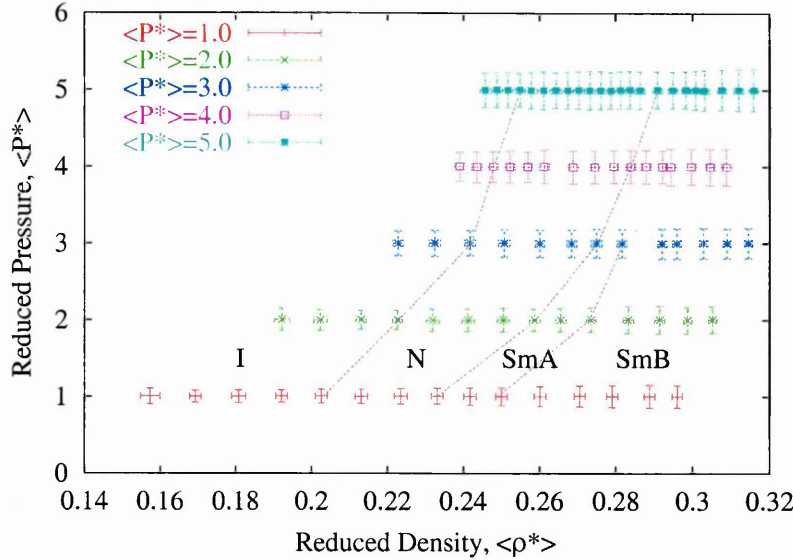


Figure 5.5: Pressure dependencies of reduced densities, $\langle \rho^* \rangle$ for mole fraction $\chi_A = 0.5$ over reduced pressure range $1.0 \leq \langle P^* \rangle \leq 5.0$

BCD is mechanical unstable. Recalling the reduced temperature is not constrained in the constant-*NPH* ensemble, for this study it is unclear at what temperature the simulations enter (AB) or leave (DE) the metastable region (the crosses over from one branch of $G(T)$ to the other). Knowing the location of B and D would not be sufficient to locate T_{N-Sm} as the transition temperature is located where the areas enclosed by ABC and CDE are equal. For a large system size these enclosed areas will diminish and the transition temperature will be become more apparent.

5.2.3.1 $1.0 \leq \langle P^* \rangle \leq 3.0$ simulations

Upon further cooling $\langle P^* \rangle = 1.0$, 2.0 and 3.0 simulations, the following stable phases were observed; *I-N-SmA-SmB* (the identity of each phase is discussed below). The

CHAPTER 5. CONCENTRATION AND PRESSURE STUDY

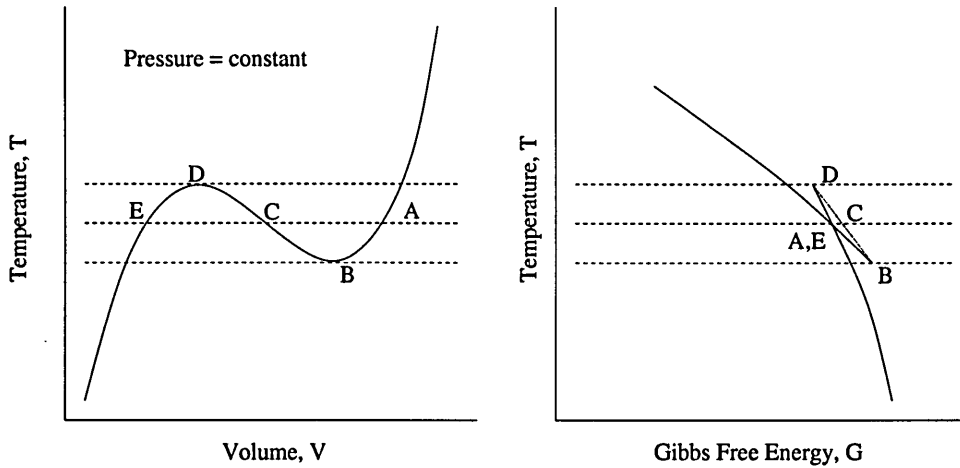


Figure 5.6: Temperature and volume relationship and corresponding Gibbs free energy as a function of temperature for a first-order transition at constant pressure.

3-dimensional representation of the isotropic, nematic, smectic-A and smectic-B phases are shown in Figure 5.7.

At higher densities each system underwent an apparently weak transition to a *SmA* phase reflected in the discontinuity in reduced potential energies and densities. The T_{N-SmA} transition temperature moves to a higher density as the pressure is increased. Just below T_{N-SmA} the behaviour of $g_{\perp}^{all}(r^*)$ showed no significant growth of transverse positional correlation and remained liquid-like (refer to Figure 5.8 for $\langle P^* \rangle = 2.0$); whereas, strong density waves parallel to the director were established. However, clearer indication is apparent in the six-fold in-plane bond correlation function $g_6^{all}(r^*)$ (equation 3.67) which approached zero at large distances clearly identifying *SmA* phases. Analysis of the reduced potential energy fluctuations over 600,000 time-steps determined the stability of the *SmA* phase for both pressures (not shown). It has been previously demonstrated that a homoge-

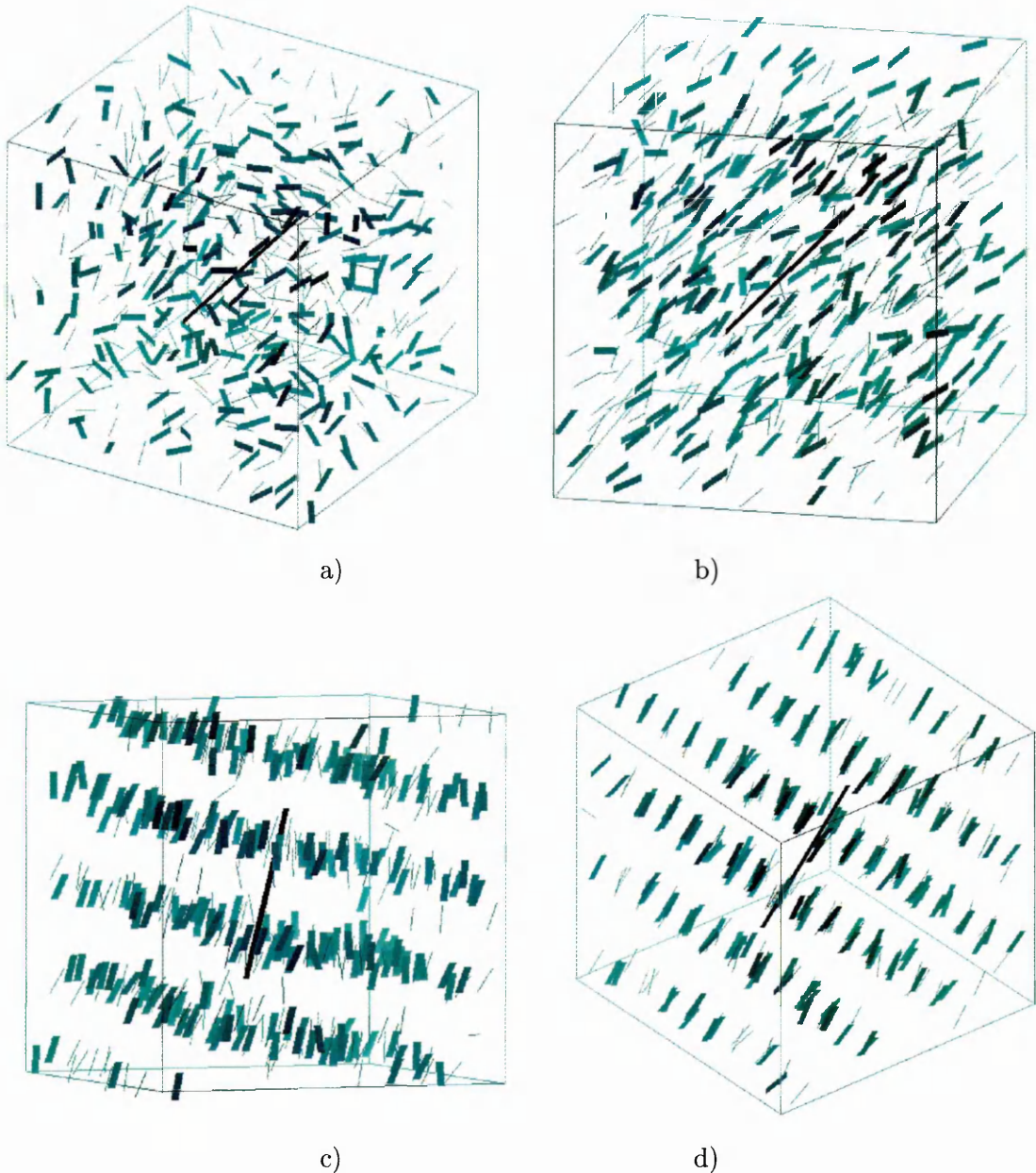


Figure 5.7: 3D visualisation of a) isotropic, b) nematic, c) smectic-A and d) smectic-B of a 50:50 GGB rods mixture (represented as unit vectors) with axial ratios of 3.5:1 (thick lines) and 3:1 (thin lines) at a reduced pressure $\langle P^* \rangle = 2.0$

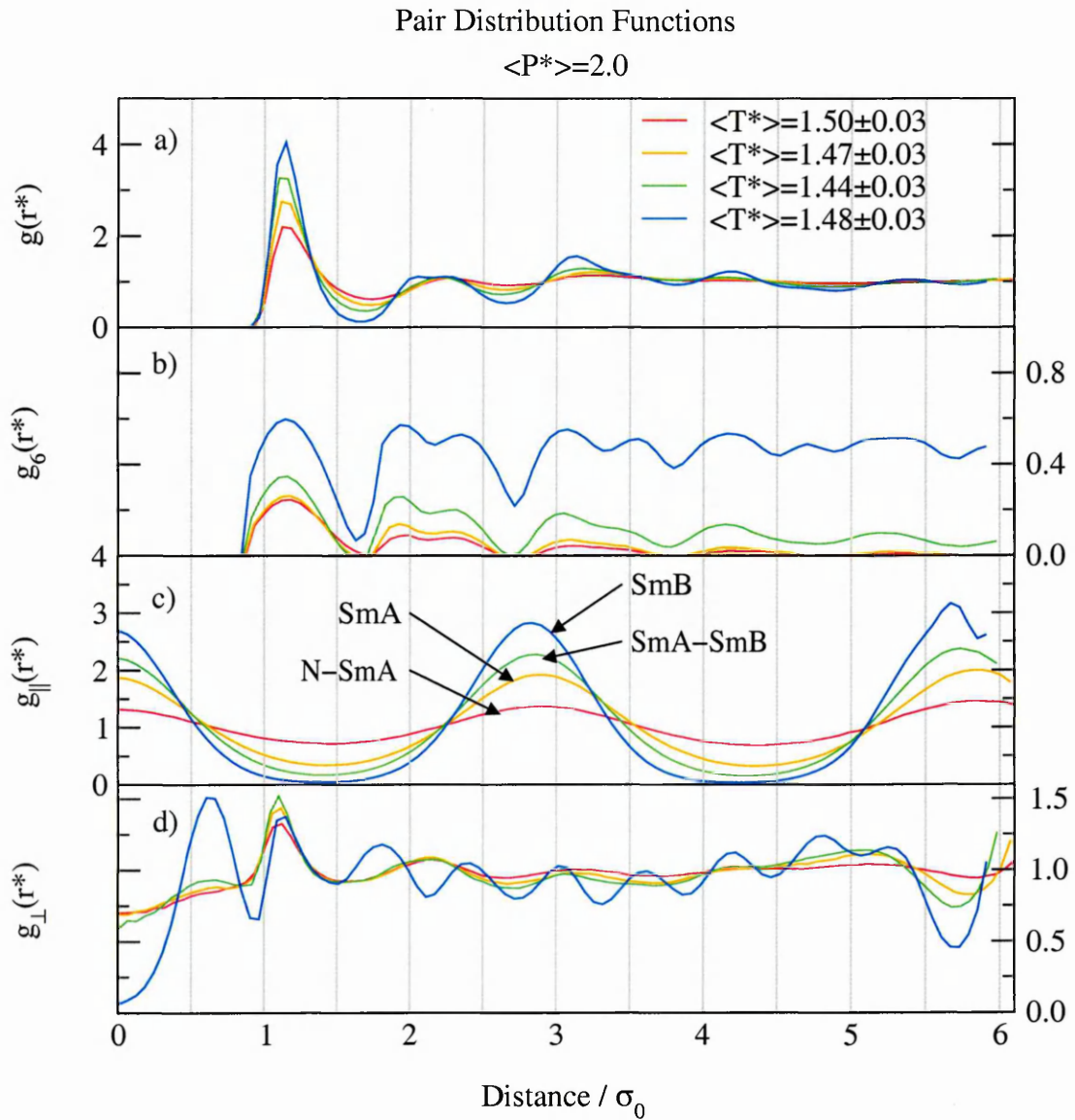


Figure 5.8: Identification of smectic-A and smectic-B phases. a) pair distribution functions, b) in-plane six-fold bond orientation functions, c) and d) pair distribution functions resolved parallel and perpendicular to the director respectively at reduced pressure $\langle P^* \rangle = 1.0$.

CHAPTER 5. CONCENTRATION AND PRESSURE STUDY

neous system of 3:1 molecules do not show a stable *SmA* phase [94] whereas molecules with aspect ratios of greater or equal to 3.6:1 do however show a stable *SmA* phase. This study is believed to be the first simulation to report a stable *SmA* phase in a mixture of 3:1 and 3.5:1 molecules. The nematic to smectic-A transition is commonly regarded as harder to measure because of the weak nature of the transition; which is shown to be true for these simulations. The order of the *N-SmA* transition is estimated by the McMillan ratio [98] T_{N-SmA}/T_{I-N} , shown in Table 5.2, which considers the coupling between the nematic and smectic order parameters. When large fluctuations within the nematic order parameter are permitted over a narrow nematic extent the phase transition is first order. A nematic phase of large extent, however, would result in the suppression of nematic order parameter thereby reducing the significance of the coupling so the transition becomes second order. The McMillan theory predicts that for a ratio $T_{N-SmA}/T_{I-N} \leq 0.89$ the transition should be second order which therefore leads to the assumption that the $\langle P^* \rangle = 1.0$ is apparently weakly first-ordered. For $\langle P^* \rangle = 2.0$ and 3.0 simulations the McMillan ratio decreased with increased pressure, as reported experimentally [99], so the transition should be continuous. However, it must be noted that in spite of the considerable research activity over the past two decades the identity of the *N-SmA* transition remains one of the principle unsolved problems in equilibrium statistical physics. In particularly, there has been a lot of controversy of the theoretical predictions [51, 100, 101] which has spurred numerous experimental studies by Garland and co-workers [102, 103, 104, 105] and simulations by Frenkel and

co-workers [106, 107, 108, 109, 110].

A third transition is apparent upon cooling the *SmA* phase. The $T_{SmA-SmB}$ transitions displays characteristic properties of a first-order process. The developing structure in $g_{\perp}^{all}(r^*)$ and a weak split in the 2nd correlation shell of $g^{all}(r^*)$ indicate transverse positional correlation (Figures 5.8). Hexagonal ordering, as expected for a smectic-B, is evident in the six-fold bond orientational ordering within the layers persisting across length of simulation box. However, the smectic-B phase should possess a loss of long range positional order but not orientational ordering of the hexagonal crystals. Due to the finite size of the simulation box, it is hard to determine whether this is the case. In addition, the shift of the first peak in $g_{\perp}^{all}(r^*)$ to $r^* \simeq 0.6\sigma_0$ is indicative of correlation between adjacent layers. The density range over which the *SmA* phase is stable diminishes upon increasing the pressure (refer to Figure 5.5) indicating a small *SmA island*. It is therefore argued that the transition from the *SmA* phase to the geometric symmetry of the *SmB* phase would be more suited to a first-order process as a continuous second-ordered phase can not lead to a change in symmetry, as reported experimentally in great detail by Chao *et al* [111]. The existence of a *N-SmA-SmB* triple point at a higher pressure and density is discussed in the following subsection.

5.2.3.2 $4.0 \leq \langle P^* \rangle \leq 5.0$ simulations

For the $\langle P^* \rangle = 4.0$ simulation, the following stable phases were observed; *I-N-SmA-SmB*. The identity of each phase was, again, distinguished by examination of

CHAPTER 5. CONCENTRATION AND PRESSURE STUDY

pair distribution functions and inlayer six-fold orientational correlation functions. The McMillan ratio T_{N-SmA}/T_{I-N} suggest that the transition should be second-order. There is some evidence of a *knee* in reduced potential energy verses temperature relationship corresponding to the T_{N-SmA} transition. Further cooling produced an apparent first-order $T_{SmA-SmB}$ transition. It is argued that the limit of the smectic-A stability is approached as can be seen from the narrowing of the smectic-A *island* as a function of pressure (refer to Figure 5.5). For the $\langle P^* \rangle = 5.0$ simulation, there is an absence of a stable *SmA* phase resulting in the following observed stable phases; *I-N-SmB*. There is some evidence of a *N-SmA* transition but the stability of the *SmA* phase is questionable since the fluctuations in reduced potential energy grow after the ambiguous T_{N-SmA} transition temperature (shown in Figure 5.9). On cooling, the system passes through close to the vicinity of the *N-SmA-SmB* triple point, as inferred from the sizable amplitude and time-scale fluctuations of the reduced potential energy in comparison to lower pressure simulations.

5.2.4 Phase behaviour diagrams

The temperature and pressure dependencies were used to construct phase behaviour diagrams from the approximate location of phase boundaries and are presented in Figures 5.3 and 5.4 with their corresponding schematic diagrams. It should be noted that all of these diagrams should be regarded as a slice through constant concentration and no attempt is made within this section to determine how exactly the addition of an extra degree of freedom, namely concentration, would change these diagrams. This is the topic of

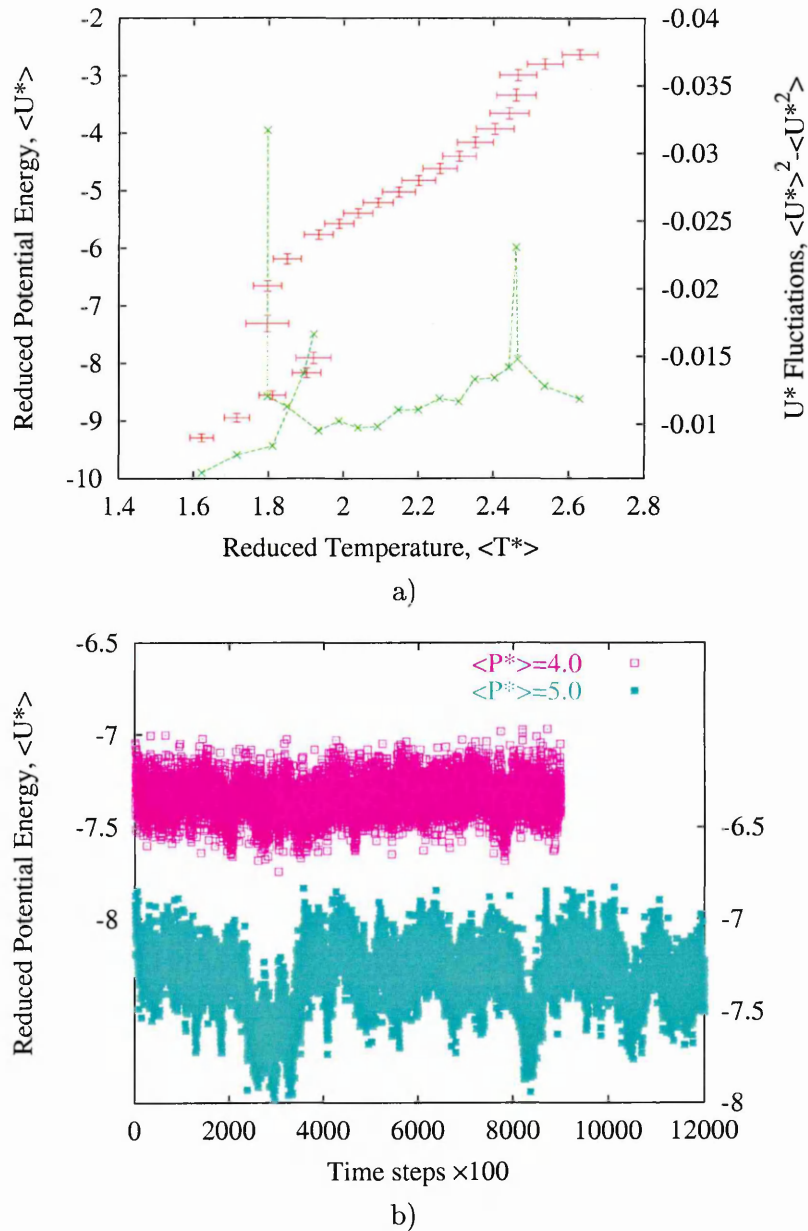


Figure 5.9: a) Temperature dependencies of reduced potential energy (+) and fluctuations analysis of reduced potential energy (x) for $\langle P^* \rangle = 5.0$ b) Evolution of reduced potential energy for $\langle P^* \rangle = 4.0$ at the $T_{SmA-SmB}$ transition temperature and for $\langle P^* \rangle = 5.0$ in the vicinity of the $N-SmA-SmB$ triple point.

CHAPTER 5. CONCENTRATION AND PRESSURE STUDY

the next study (section 5.3). The approximate location of the phase boundaries are shown; clearly reliability of the specific boundary locations has to be resolved by detailed specific heat calculations. Nevertheless, extrapolations of the phase boundaries show the *I-N* slope of dT_{I-N}/dP to be larger than the equivalent *N-Sm* slope in accordance with experimental [112] and theoretical predictions of the Clausius-Clapeyron equation. This leads to an increased nematic range *i.e.* the temperature range over which the nematic phase is stable increases as the pressure is increased. The increased nematic range may be a consequence of the reduction of the molecules' free space such that the smectic phase is suppressed and the system remains nematic. In addition, the greater slope of the *I-N* phase boundary in comparison to the *N-SmA* phase boundary suggests that the nematic phase may vanish at low pressures, $\langle P^* \rangle < 1.0$. Therefore the location of the *I-N-Sm* triple point, T_o is suggested to be in the vicinity of $\langle T^* \rangle = 1.25 \pm 0.10$, $\langle P^* \rangle = 0.75 \pm 0.25$ and $\langle \rho^* \rangle = 0.21 \pm 0.02$.

In common with the results presented in chapter 4 for the 50:50 mixtures within the constant-*NVE* ensemble, long molecules have a consistently higher value of $\langle S \rangle$ than the short molecules as a consequence of the short molecules' greater orientational freedom. The difference in order of the long and short molecules is greater proceeding the *I-N* transition and then decreases as the smectic phase is approached (Refer to Table A.1 through to A.5). As a precursor to the smectic phase, density waves resolved parallel to the director for each molecular species are present in the nematic phase. This pre-smectic ordering is believed to be associated with the suppression of the smectic phase and arises from the competition

between the two molecules of differing lengths.

5.2.5 Summary

In this study a series of simulations are reported characterising the behaviour of binary mixtures consisting of 3.5:1 and 3:1 Generalised Gay-Berne molecules at a fixed $\chi_A = 0.5$ concentration over a range of pressure $1.0 \leq \langle P^* \rangle \leq 5.0$ within the constant-*NPH* ensemble. The binary mixture exhibits isotropic, nematic, smectic-A and smectic-B phases depending on the choice of pressure. This study is believed to be the first report of a stable *SmA* phase in a mixture of 3:1 and 3.5:1 molecules. Phase diagrams are presented for $\langle T^* \rangle vs. \langle \rho^* \rangle$ and $\langle P^* \rangle vs. \langle T^* \rangle$. A small smectic-A *island* appears in the phase diagrams above $\langle P^* \rangle = 1.0$ which is bounded by a *N-SmA-SmB* triple point at approximately $\langle P^* \rangle \simeq 5.0$. The phase boundaries show the *I-N* slope of dT_{I-N}/dP larger than the equivalent *N-Sm* slope resulting in an increased nematic range in agreement with experimental data. Extrapolation of the phase diagram suggests that the nematic may be absent at low pressures of $\langle P^* \rangle < 1.0$.

5.3 Influence of concentration

So far the discussion has been restricted to discussing fixed 50:50 mixtures of 3.5:1 and 3:1 rod-like molecules. The remainder of this chapter examines the effect of concentration on the phase behaviour and structural properties of bidisperse liquid crystal.

CHAPTER 5. CONCENTRATION AND PRESSURE STUDY

Much of the theoretical background of bidisperse liquid crystals are limited to rigid hard rods and are based around extensions of the Onsager theory developed in the mid-eighties by Lekkerkerker and co-workers [55, 56, 87, 57], Sluckin [61], and recently revisited by Mulder and co-workers [60, 113, 114, 59, 115, 116, 117] (refer to section 2.2 of chapter 2). However, there are a limited number of bidisperse simulations of hard (or soft) rod-like molecules in the literature. Of these, Stroobants [66, 67] investigated the effect of length dispersity on the stability of the smectic phase using parallel aligned bidisperse spherocylinders. Stroobants reported that the smectic phase is suppressed to higher densities and, for large deviations from monodispersity, is pre-empted by the columnar phase (refer to Figure 2.8 of chapter 2). More exotic biphasic ($I-I$) and triphasic ($I-N-N$) coexistence phases have recently been studied by van Roij *et al* [118, 115] using a binary mixture of rod-like molecules (colloids) and ideal needles each of extreme length-to-breadth ratios. Escobedo [119] and Mills [91] studied the $I-N$ coexistence region in bidisperse simulations where the constituted molecules had less extreme length-to-breadth ratios. The aforementioned simulations have their limitations. Aligned rod-like molecules of Stroobants' simulations do not posses orientational freedom. Meanwhile, all four phase coexistence studies exploited the Gibbs ensemble and, as such, are limited to low densities. No bidisperse simulations to date have shown an extended nematic range (defined by $T_{N-Sm} - T_{I-N}$) which depends on concentration. It is the aim of this section to characterise the effect of a concentration on the phase behaviour and structural properties of a liquid crystal mixture.

CHAPTER 5. CONCENTRATION AND PRESSURE STUDY

Before commencing the series of simulations, it was not clear whether the choice of constitute molecules would phase-separate as the composition of each mixture varies. In a homogeneous mixture held at constant temperature and pressure, the system will separate into two phase if the total Gibbs free energy of both phase configurations is less than that of the homogeneous mixture. Within an inhomogeneous mixture the condition for thermodynamic equilibrium of any mixture at constant temperature and pressure the system still has to satisfy the condition that the Gibbs free energy is a minimum. The only difference which the introduction of several components makes is that the Gibbs free energy contains a greater number of variables and, as such, has a greater degree of phase space to explore [120]. In general, phase separation is governed by the competition between entropy of mixing and changes in energy associated with the energy of interactions between dissimilar and similar molecules. The entropy of mixing behaves in the same way as mixing two ideal gases. The energy of mixing is essentially independent of the temperature but the entropic contribution is proportional to the temperature and increasingly favours the mixed state as the temperature is raised.

In this section, the phase behaviour and structural properties are investigated for several systems of 3.5:1 and 3:1 rod-like molecules (total of $N = 500$) at one of the following mole fractions, $\chi_A = 0, 0.25, 0.75$ and 1 each at a reduced pressure of $\langle P^* \rangle = 5.0$. The simulation at $\chi_A = 0.5$ is taken from the previous study and not repeated. The choice of reduced pressure should maximise the nematic range across the concentration range. It

CHAPTER 5. CONCENTRATION AND PRESSURE STUDY

has been shown in the previous section that simulations performed at a reduced pressure of $\langle P^* \rangle = 5.0$ and mole fraction of $\chi_A = 0.5$ do not exhibit a smectic-A phase. Therefore, reappearance of such phases in the χ_A vs. $\langle T^* \rangle$ phase diagram can be characterised as a concentration dependency and not pressure induced mesomorphism.

5.3.1 Simulation details

The simulation details for this investigation are identical to those used in section 5.2.

5.3.2 Results and analysis

The series of simulations were carried out in essentially the same manner as the previous study. Each starting configuration was generated at the appropriate mole fraction and commenced with the molecules *A* and *B* distributed randomly on an f.c.c. lattice at a reduced density of $\langle \rho^* \rangle = 0.17$ and melted off the lattice at a relatively high reduced temperature of $\langle T^* \rangle = 3.0$. After establishing an isotropic phase for each system from examination of order parameter pair distribution and orientational correlation functions, each system was steadily cooled by reducing the rotational and translational velocities by a scaling factor typically of 0.9 with respect to the previous temperature and by 0.95 close to transition temperatures. The temperature dependencies of order parameter, reduced potential energy and reduced density are shown in Figures 5.10 and 5.11 and in Tables B.1 through B.4 of Appendix B and Table A.5 of Appendix A.

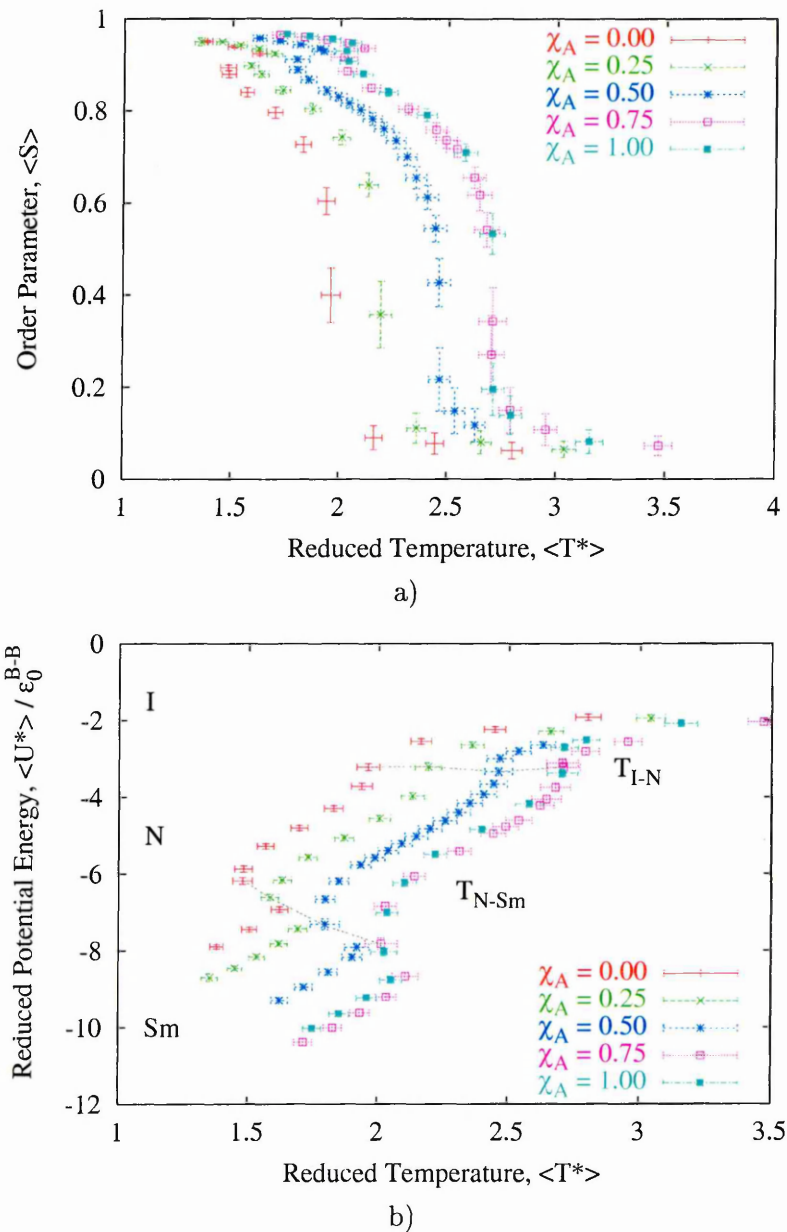


Figure 5.10: Temperature dependencies of a) order parameters, $\langle S^{all} \rangle$ and b) reduced potential energy, $\langle U^* \rangle$ of constant-*NPH* molecular dynamics simulations of GGB rods with axial ratios of 3.5:1 (molecules A) and 3:1 (molecules B) at mole fractions $\chi_A = 0, 0.25, \dots, 1$ and reduced pressure of $\langle P^* \rangle = 5.0$.

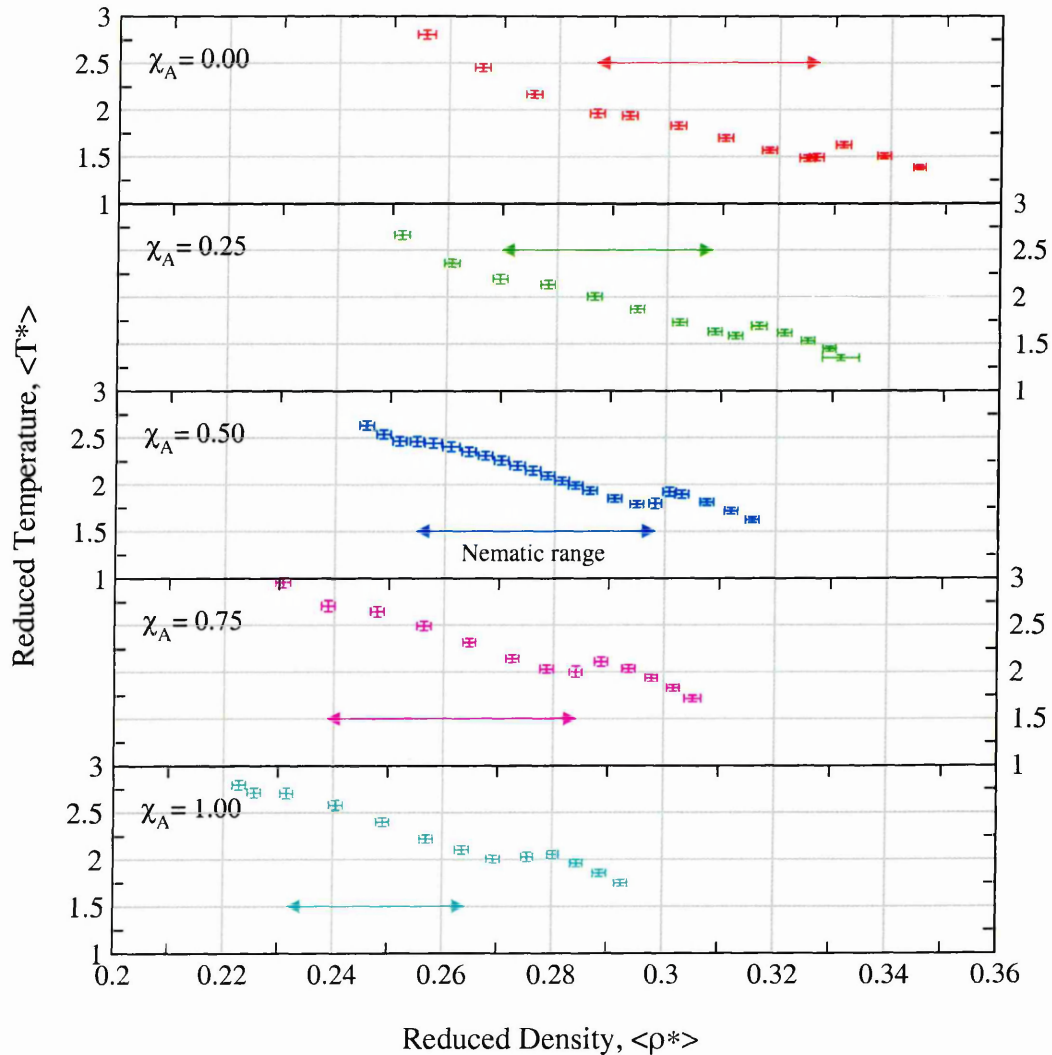


Figure 5.11: Temperature dependency of reduced density, $\langle \rho^* \rangle$ at mole fractions $\chi_A = 0, 0.25, \dots, 1$ and reduced pressure of $\langle P^* \rangle = 5.0$. The range of the nematic phase is indicated by horizontal arrows.

These simulations share common salient features with those in the previous study and are briefly discussed here. The onset of orientational order was signified by sizeable time-scale fluctuations in order parameter, reduced potential energy and reduced density. Upon cooling each simulation showed a discontinuity in the aforementioned observables, characteristic of a first-order transition. The long time-scale fluctuations were observed to be persistent thus establishing a stable nematic phase. Throughout the nematic phase the long molecules had a greater order parameter than their smaller counterparts. This difference was greatest proceeding the *I–N* transition and diminished prior to the *N–Sm* transition.

5.3.3 Comparison of homogeneous 3:1 simulation to literature

The exponents of the Gay-Berne parameterisation well depth function $\epsilon(\hat{\mathbf{u}}_A, \hat{\mathbf{u}}_B, \hat{\mathbf{r}}_{AB})$ used in all simulations of chapters 4 and 5 differs from the original Gay-Berne parameterisation; $\mu = 1$ and $\nu = 2$ were used rather than $\mu = 2$ and $\nu = 1$ (refer to section 4.2 of chapter 4). The systems at the extremes of the concentration phase diagram, $\chi_A = 0$ and $\chi_A = 1$, are homogeneous. A comparison can be drawn between the simulation at $\chi_A = 0$ (monodisperse 3:1 rod-like molecules) and the constant-*NVE* simulation of Luckhurst *et al* [85] at a reduced density of $\langle \rho^* \rangle = 0.3$. Equivalent reduced temperatures and densities from both simulations are shown in Table 5.3. No pressure data is reported by Luckhurst. Order parameters from Luckhurst's simulation was estimated by linear extrapolation between two data points with the nematic phase and are shown to be in reasonable agreement

$\langle T^* \rangle$	$\langle S \rangle$	$\langle S_{(L)} \rangle$	$\langle \rho^* \rangle$	$\rho_{(L)}^*$
1.92(04)	0.60(03)	0.55	0.293(001)	0.3
1.82(04)	0.73(02)	0.65	0.302(001)	0.3

Table 5.3: Comparison between Luckhurst *et al* [85] constant-*NVE* simulation (displayed with the suffix “L”) and results obtained from the $\chi_A = 0$ constant-*NPH* simulation of this study.

with the $\chi_A = 0$ simulation.

5.3.4 Concentration dependency on T_{I-N}

Following the analysis of the previous study, the approximate location of transition temperatures for each mole fraction were determined by identifying discontinuities in reduced potential energies and densities, growth of increased correlation within pair distribution functions and, in part, from studying fluctuations of the reduced potential energy (refer to Table 5.4). The transition temperature dependencies of each simulation were used to construct the phase behaviour diagram (the location of the transition are shown as a dotted grey lines on Figure 5.12). The *I*-*N* transition dependence on concentration is interesting. The transition temperature varies essentially linearly over $0 \leq \chi_A < 0.75$ and then breaks from linearity at $\chi_A = 0.75$. Two explanations are offered: *a)* The $\chi_A = 0.75$ simulation is not in thermodynamic equilibrium and does not reflect the true location of the *I*-*N* location. This would not seem likely as after the transition long time-scale fluctuations of the order parameters, reduced potential energy and density were observed to be

Transition or Phase	Mole Fraction χ_A	Temperature $\langle T^* \rangle$	Density $\langle \rho^* \rangle$	Energy $\langle U^* \rangle$
<i>I-N</i>	0.00	1.96(04)	0.287(001)	-3.22(09)
	0.25	2.19(05)	0.270(001)	-3.21(10)
	0.50	2.46(05)	0.255(001)	-3.34(10)
	0.75	2.70(06)	0.239(001)	-3.23(13)
	1.00	2.70(05)	0.232(001)	-3.37(11)
<i>SmA</i>	0.25	1.63(03)	0.308(001)	-6.16(09)
<i>N-SmA</i>	1.00	2.10(05)	0.264(001)	-6.24(10)
<i>SmA-SmB</i>	0.25	1.60(04)	0.315(001)	-6.87(07)
	1.00	2.02(05)	0.275(001)	-8.03(11)
<i>N-SmB</i>	0.00	1.47(03)	0.327(001)	-6.18(09)
	0.50	1.80(03)	0.298(001)	-7.31(14)
	0.75	2.01(06)	0.284(001)	-7.82(15)

Table 5.4: Approximate location of T_{I-N} , T_{N-SmA} , $T_{SmA-SmB}$ transition temperatures

persistent. *b*) The short molecules miscible (25%) within the greater number long molecules (75%) make no significant contributions to changing the kinetics of the system on the whole as evident from the temperature dependency of the reduced potential energy (Figures 5.10). This is backed up by mean field theory prediction [56] and Gibbs ensemble simulations of Mills *et al* [91] of the *I-N* coexisting envelope (shown in the schematic of Figure 5.12). Although the simulation cannot trace the coexisting envelope outline, it is suggested that the *I-N* transition temperature will reflect the upper envelope.

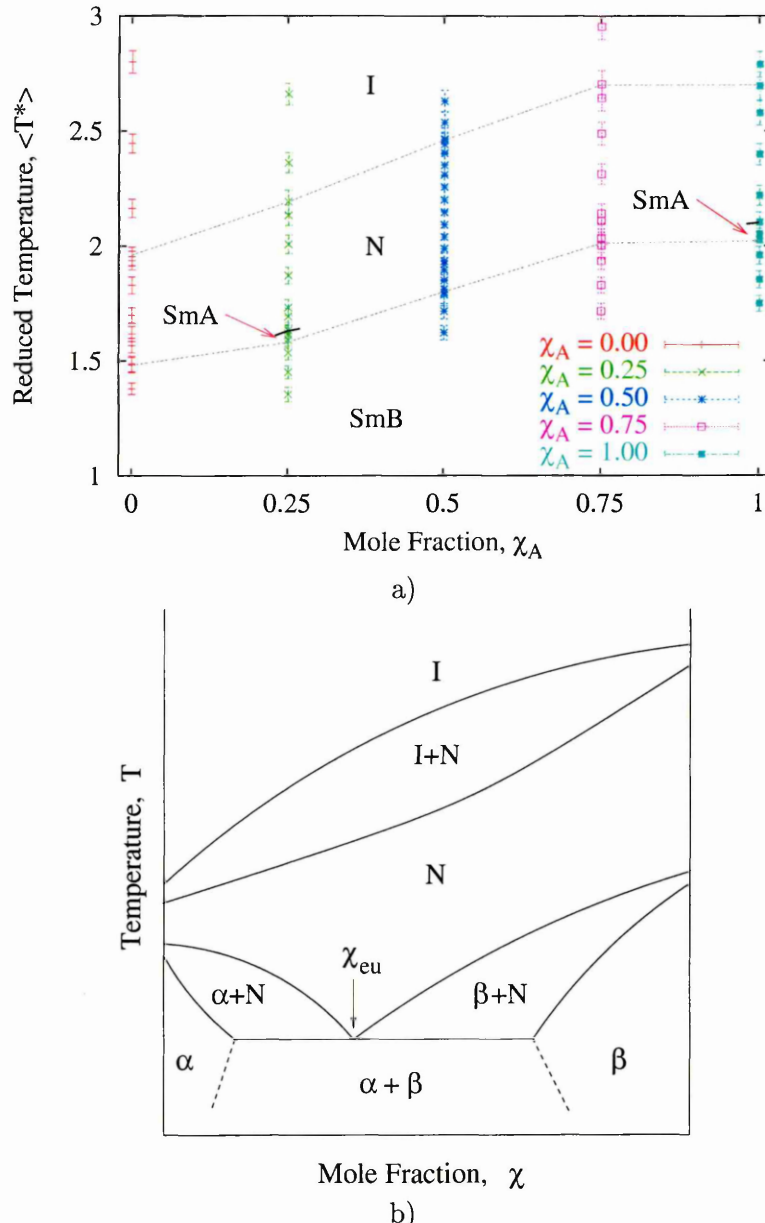


Figure 5.12: a) Concentration dependencies of transition temperatures at mole fractions $\chi_A = 0, 0.25, \dots, 1$ and reduced pressure of $\langle P^* \rangle = 5.0$. b) General schematic phase diagram leading to eutectic point χ_{eu} between different crystal structures α and β .

5.3.5 Postponement of Smectic Phases and Layer Spacing

Before embarking on a qualitative discussion of the concentration dependency of the nematic range the location of the N - Sm transitions were determined by similar analysis previously described in section 5.2.3.1. In summary, the $\chi_A = 0.00, 0.50$ and 0.75 simulations demonstrated the following stable phases I - N - SmB . Whereas, the $\chi_A = 0.25$ and 1.00 simulations revealed the following stable phases I - N - SmA - SmB (refer to Figures 5.18 and 5.14). The possibility of an *induced SmA* phase is discussed in the following section.

The location and nature of the N - SmB transition in the concentration phase diagram is of particularly interest. Theory predicts the postponement of the N - Sm transition to higher densities [61, 60] reflecting the fact that molecules of different lengths will interfere with the natural layering of the homogeneous smectic phases thus destabilising them with respect to the nematic phase. This was demonstrated by simulations of Stroobants' [66, 67] and McGrother *et al* [121] but the effect of concentration was not established. The postponement of the smectic phase to higher densities is clearly shown in Figure 5.11 as the mole fraction of molecule *A* (3.5:1 length-to-breadth ratio) is reduced. The following conjecture is made by the author: the postponement of the smectic phase to higher densities is achieved by,

- increasing the molecular dispersity, keeping the mixtures at their equivalence point so that the partial volume fractions of both compounds are equal [66, 67],

CHAPTER 5. CONCENTRATION AND PRESSURE STUDY

- or by decreasing the mole fraction of the longer molecule, effectively reducing the systems free volume.

This conjecture is not surprising since both parameters, length dispersity and concentration, can be regarded as independent to each other in parameter space.

The $\chi_A = 0.0$ simulation (3:1 molecules) showed no evidence of a stable *SmA* phase, whereas the $\chi_A = 1.0$ simulation (3.5:1 molecules) indicates the presence of a narrow stable *SmA* phase at $\langle T^* \rangle = 2.05 \pm 0.04$, $\langle \rho^* \rangle = 0.280 \pm 0.001$ and $\langle U^* \rangle = -8.76 \pm 0.09$ (refer to Figures 5.13 and 5.14). This results is consistent with the conclusion of Brown *et al* [94] that the *SmA* phase is possibly just becoming stable as the molecular elongation increases to 3.4:1 ratio (just below the molecules' elongation used in this study). Brown *et al* employed the original Gay-Berne potential exponents. Considering that the mixture would disrupt the formation of smectic layers an alternative choice of Gay-Berne potential exponents were used in all simulations of Chapters 4 and 5 (refer to section 4.2). Nevertheless, the location of the *SmA* phase for the $\chi_A = 1.0$ simulation is in agreement with the equation of state diagram of Brown *et al* [94].

The *SmB* layer spacing immediately proceeding the transition also shows a cubic relationship similar to the T_{N-Sm} transition temperatures. The *SmB* layer spacing is in good agreement with experimental results of Lydon and Coakley [30] (refer to section 2.1). At no concentration is the *SmB* layer spacing greater than or less than that of the homogeneous systems $\chi_A = 0.0$ and $\chi_A = 1.0$ respectively. Figures 5.15 presents two extreme models

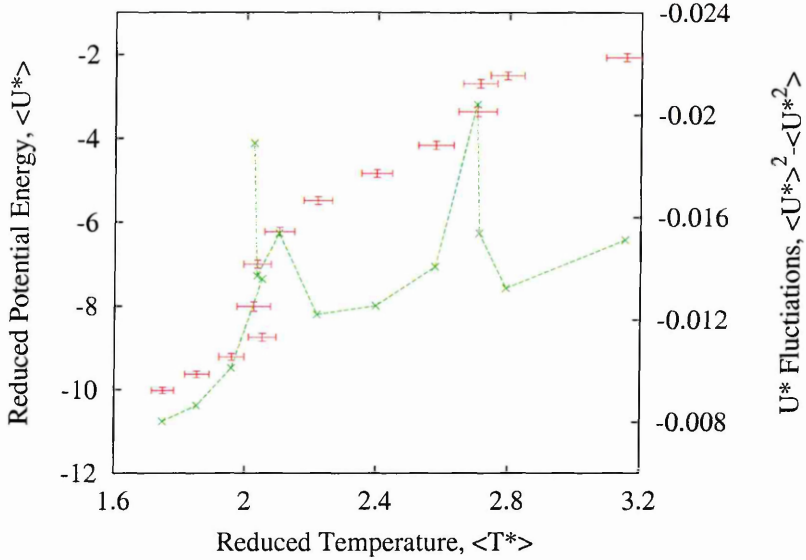


Figure 5.13: Temperature dependencies of reduced potential energy (+) and fluctuations analysis of reduced potential energy (x) for $\chi_A = 1.0$.

suggested by Lydon and Coakley [30] for molecular packing arrangements of mixed smectic phases. In model *a*) the molecules are segregated into domains of like molecules, where each domain extends over several smectic layers. In model *b*) the molecules are randomly mixed within each smectic layer where, therefore, the smectic layer thickness relies on the competition between the two molecular species of differing lengths. However, a range of intermediate possibilities exists incorporating variations of domain size to a single layer and in-plane local ordering of an appreciable area. For this study, the smectic phases across the concentration phase diagrams are found to be fully commensurate. Therefore, it is suggested that the molecular packing arrangements of mixed smectic phases in this study are more suited to model *b*). This could account for a certain degree of local order seen in $g^{all}(r^*)$ as previously reported in Chapter 4.

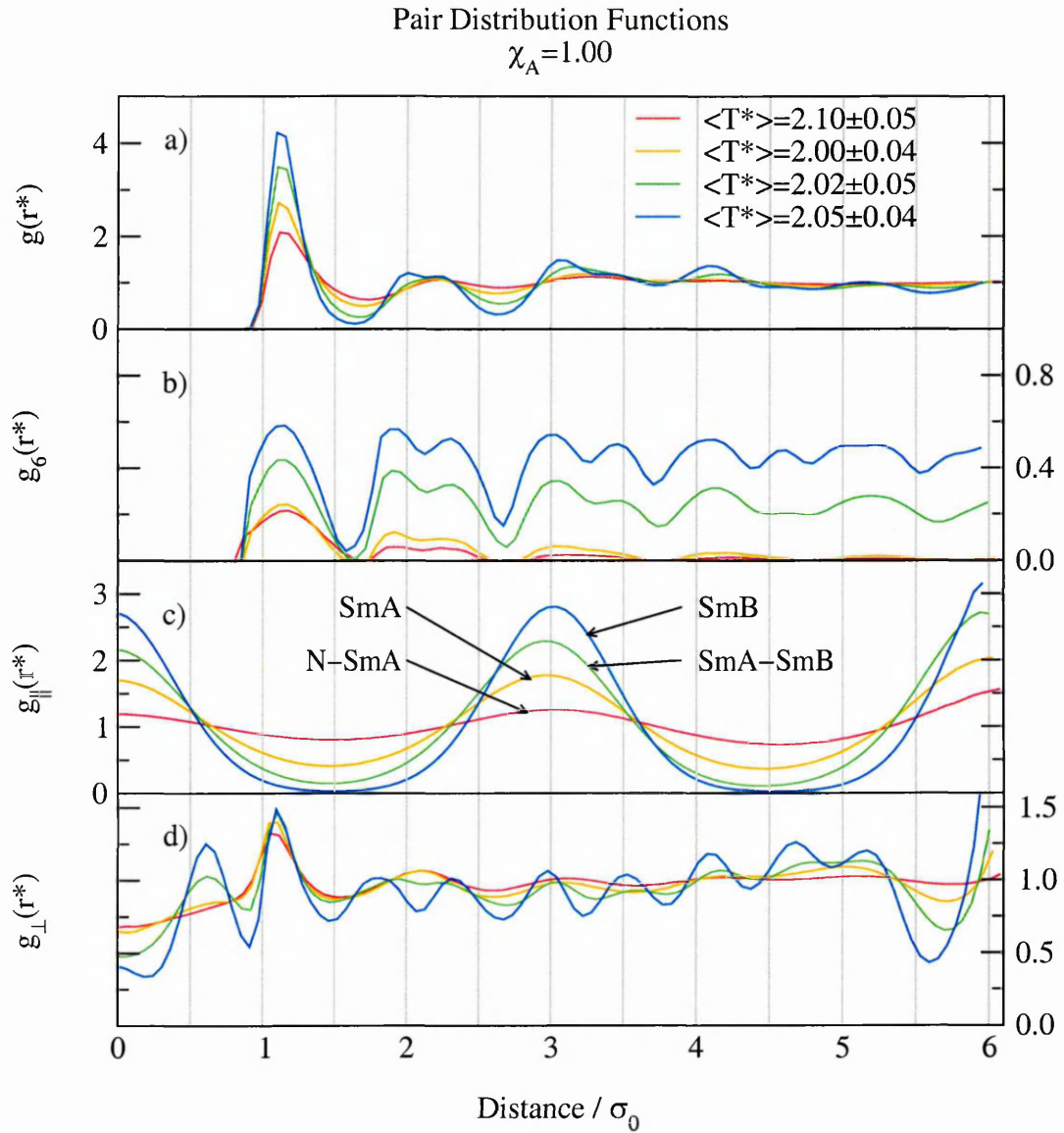


Figure 5.14: Identification of smectic-A and smectic-B phases. a) pair distribution functions, b) in-plane six-fold bond orientation functions, c) and d) pair distribution functions resolved parallel and perpendicular to the director respectively at concentration $\chi_A = 1.0$.

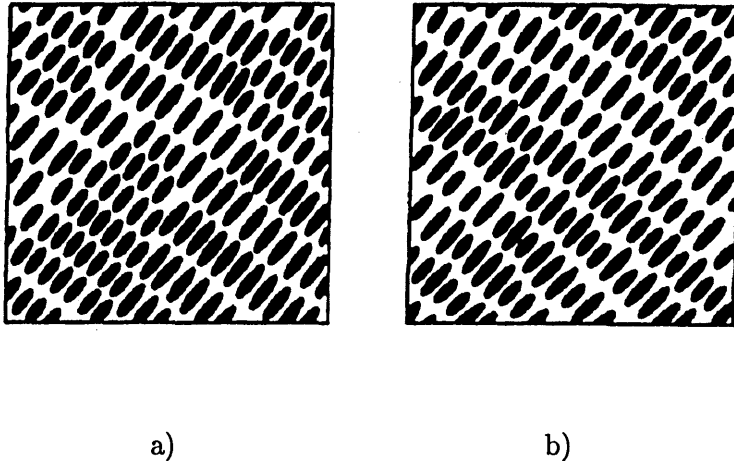


Figure 5.15: Two extreme models for the molecular arrangements in a mixed smectic phase [30] Model a) segregated into domains of like molecules. Model b) randomly mixed smectic layers.

5.3.6 Induced *SmA* Phase for $\chi_A = 0.25$ simulation

One of the most intriguing phenomena reported experimentally [122, 123] and predicted theoretically [124] for the binary mixture of liquid crystals is the *induced* (or injected) smectic phase. According to Kyu *et al* [124], the question of whether or not an induced smectic phase occurs in a nematic mixture can be considered via the temperature dependency of the coupling terms involving the cross-nematic and the cross-smectic order parameters. An induced smectic phase becomes stable when the cross-smectic order parameter, which has a similar characteristic to the McMillan smectic order parameter, becomes significant with respect to the homogeneous mesogens. The stability of the induced *SmA* phase at $\chi_A = 0.25$ was determined by analysis of reduced potential energy fluctuations (Figure 5.17). These fluctuations diminished near to the *N-SmA* transition temperature

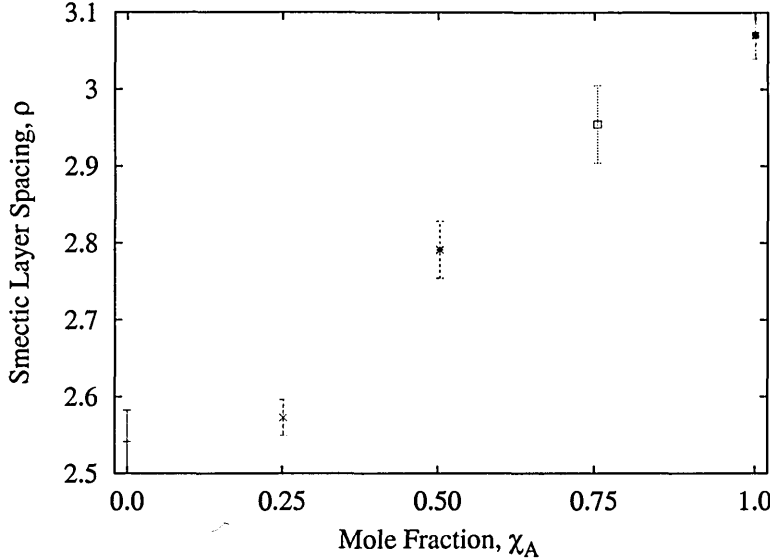


Figure 5.16: Concentration dependencies of smectic layer spacing at mole fractions $\chi_A = 0, 0.25, \dots, 1$ and reduced pressure of $\langle P^* \rangle = 5.0$ immediately proceeding *SmB* transition.

of $\langle T^* \rangle = 1.63 \pm 0.03$. The possibility that the induced *SmA* phase is metastable cannot be ruled out. Just below T_{N-SmA} the behaviour of $g_1^{all}(r^*)$ showed no significant growth of transverse positional correlation and remained liquid like (refer to Figure 5.18). Whereas, strong density waves parallel to the director were established. However, clearer indication is apparent in the six-fold in-plane bond correlation function $g_6^{all}(r^*)$ which approached zero at large distances identifying a *SmA* phase at $\langle T^* \rangle = 1.58 \pm 0.03$, $\langle P^* \rangle = 4.99 \pm 0.01$, $\langle \rho^* \rangle = 0.312 \pm 0.001$ and $\langle U^* \rangle = -6.61 \pm 0.08$. The presence of an induced *SmA* phase also gives rise to the existence of two *N-SmA-SmB* triple points either side of $\chi_A = 0.25$, although the size of the induced *SmA* island is not resolved. This does open up future studies employing, say, a binary mixture of 3:1 and 4:1 molecular elongation in an attempt to locate a stable induced *SmA* island over a greater temperature range.

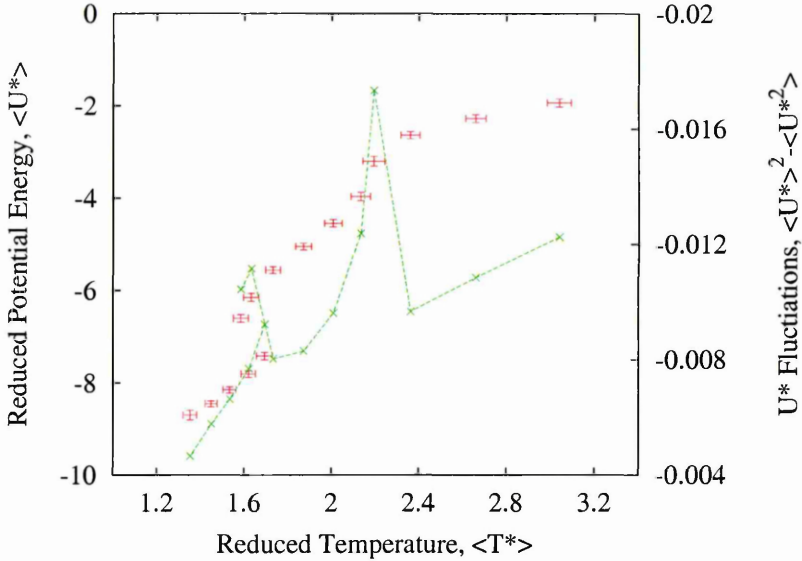


Figure 5.17: Temperature dependencies of reduced potential energy (+) and fluctuations analysis of reduced potential energy (x) for $\chi_A = 0.25$.

5.3.7 Extended Nematic Range

The combination of two or more “off the shelf” mesogens of varying chemical composition, geometric size and shape to attain novel properties or phases unobtainable in either pure systems has long been exploited by experimental chemists. For example, extending the temperature range over which the nematic phase is stable increases the utility of the device. The concentration dependency on the nematic range is shown on Figure 5.19. An extended nematic range is clearly evident at approximately $\chi_A \simeq 0.75$ *i.e.* the nematic range is greater than that of the homogeneous system of either molecules. It is believed that this is the first reported simulation of an extended nematic as a consequence of concentration. The McMillan relationship of T_{N-Sm}/T_{L-N} (Figure 5.20) reveals that concentration

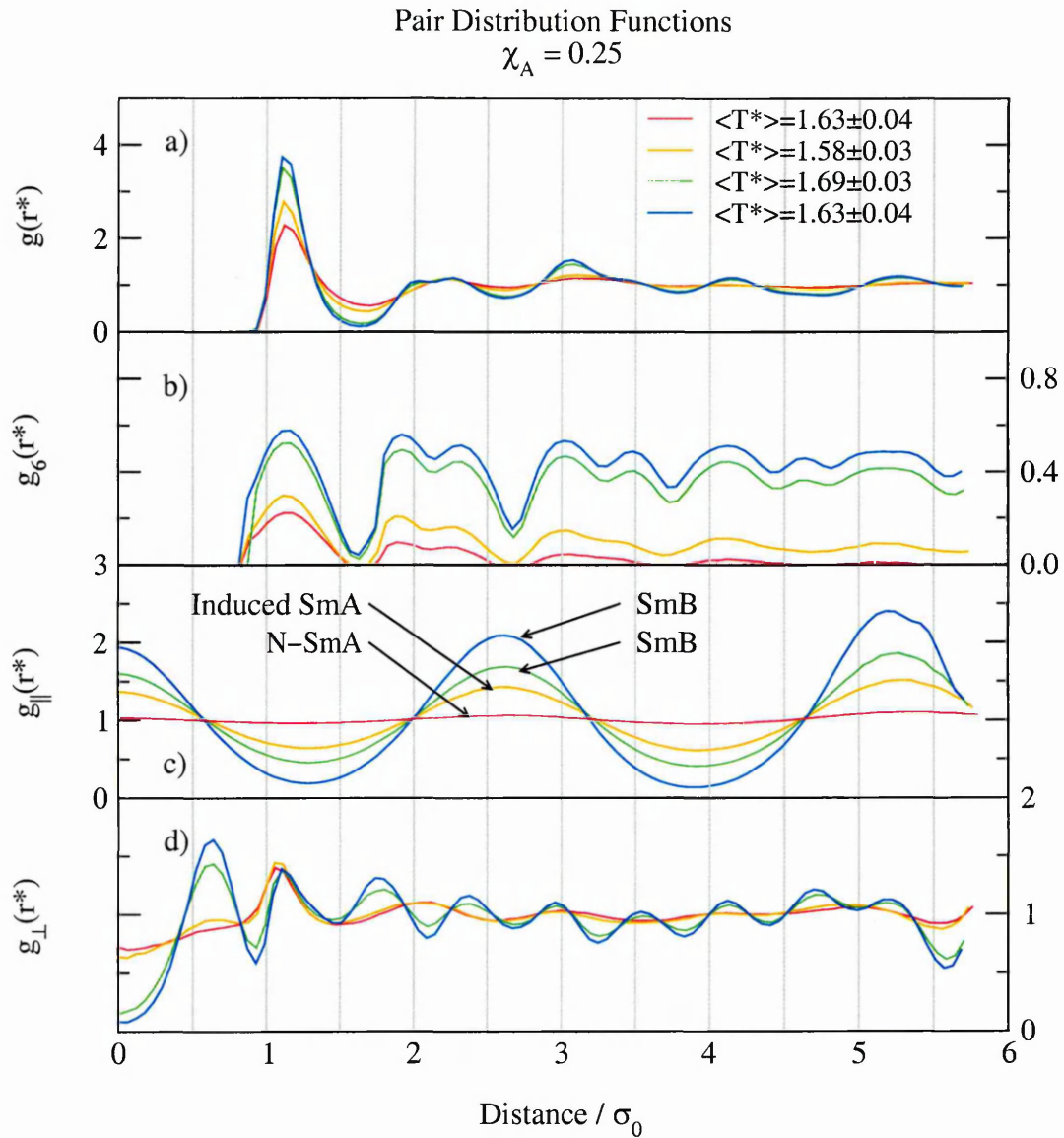


Figure 5.18: Identification of smectic-A and smectic-B phases. a) pair distribution functions, b) in-plane six-fold bond orientation functions, c) and d) pair distribution functions resolved parallel and perpendicular to the director respectively at concentration $\chi_A = 0.25$.

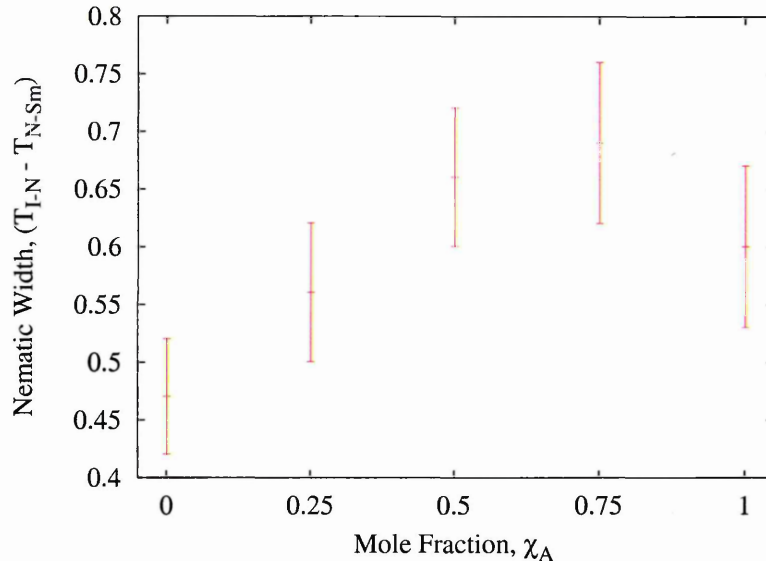


Figure 5.19: Concentration dependence of nematic range defined at $T_{I-N} - T_{N-Sm}$. The nematic range at $\chi_A \simeq 0.75$ greater than that of the homogeneous system of either molecule.

plays little role in the coupling between the nematic and smectic phase which, although rather surprising, is in agreement with experiments[125].

5.3.8 Summary

In this study a series of simulations are reported characterising the behaviour of binary mixtures over a range of concentrations $0.0 \leq \chi_A \leq 1.0$ consisting of 3.5:1 and 3:1 Generalised Gay-Berne molecules at a fixed pressure $\langle P^* \rangle = 5.0$ within the constant-*NPH* ensemble. The binary mixture exhibits isotropic, nematic, smectic-A, induced smectic-A and smectic-B phases depending on the choice of concentration. The $\chi_A = 1.0$ simulation (3.5:1 molecules) indicates the presence of a narrow stable *SmA* phase consistent with recent understanding that the *SmA* phase just becomes stable as the molecular elongation

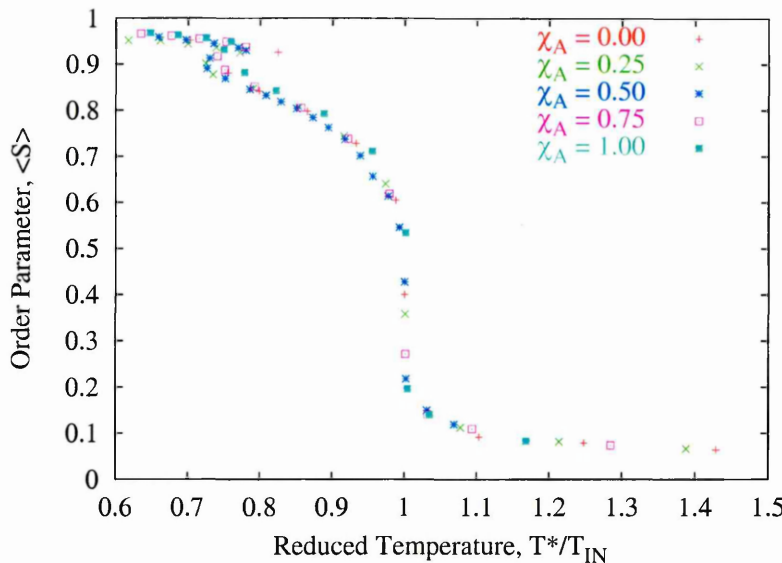


Figure 5.20: Concentration dependence of the McMillan ratio.

is greater or equal to 3.4:1 length to breadth ratio. More intriguing is the existence of a narrow induced *SmA* phase at $\chi_A = 0.25$. This is believed to be the first simulation to report an induced *SmA* phase in a binary mixture of liquid crystals.

The concentration dependency phase diagram of the transition temperatures is presented. The *I-N* transition temperature portrays the upper limit of the coexisting envelope. The postponement of the *N-Sm* transition to higher densities reflects the fact that molecules of different lengths will interfere with the natural layering of the homogeneous smectic phases thus destabilising them with respect to the nematic phase. The following conjecture is offered; the postponement of the smectic phase to higher densities is achieved by increasing the molecular dispersity or by decreasing the mole fraction of the longer molecule. At no concentration is the *SmB* layer spacing greater or less than that of the

either homogeneous systems.

An extended nematic range is clearly evident at approximately $\chi_A \simeq 0.75$ where the nematic range is greater than that of the homogeneous system of either molecules thereby successfully demonstrating the acquisition of a property unobtainable in either pure systems. The McMillan relationship of T_{N-Sm}/T_{I-N} reveals that concentration plays little role in the coupling between the nematic and smectic phase.

5.4 Concluding Remarks

The main difficulties arising from these studies are associated with the increased computational inefficiency of the constant-*NPH* ensemble with respect to the constant-*NVE* ensemble. The onset of phase transitions were signified by sizeable time-scale fluctuations of the order parameter, reduced density and reduced potential energy requiring extended equilibration periods of typically 600,000 simulation time-steps. However, it was not uncommon for equilibration periods too extended to over 1,000,000 simulation time-steps where the system sampled both sides of the transition. In addition, the absence of a temperature constraint of the ensemble resulted in van der Waals heating in the vicinity of the *N-Sm* transitions. Although at first unwelcome, the physical interpretation was appreciated and did not detract attention from either study.

The conclusions gained from both studies advanced the understanding of the phase behaviour of binary liquid crystal mixtures. It is reassuring to obtain an extended nematic

CHAPTER 5. CONCENTRATION AND PRESSURE STUDY

range greater than that of the homogeneous system of either molecules. Moreover, it was heartening to gather evidence of an induced smectic-A phase in the concentration phase diagram.

Clearly more work has to be undertaken to complete the picture of phase behaviour and structural properties of binary liquid crystal mixtures. Thus, the following items are offered:

- Perform future studies in the constant-*NPT* ensemble in order to remove van de Waals heating or alternatively increase the system size to minimise the heating effect.
- A judicious choice of constituent molecules leading to increased smectic-A stability, columnar phases and/or smectic layer spacing greater than of the homogeneous system of either molecules.
- Determination of the *SmA–SmB* transitions order via specific heat calculations.

Chapter 6

Conclusions and Future Work

Liquid crystal mixtures are not only of physical interest but also play an important role in many applications. The current study allowed the investigation of bidisperse liquid crystals on such properties as the effect of length dispersity, concentration and pressure. Despite the relative simplicity of the model, the results are in good agreement with experimental and theoretical predictions. These results go some way to improving the understanding of this field.

6.1 Concluding remarks

The constant-*NVE* simulation of a 50:50 mixture presented in Chapter 4 exhibits isotropic, nematic and smectic phases with the *I-N* phase boundary not clearly defined. Pre-smectic ordering precedes the *N-Sm* phase transition for a considerable temperature range, which is attributed to competition between two different density waves of the same

CHAPTER 6. CONCLUSIONS AND FUTURE WORK

wavelength but different phases. Measurements of $g_{\parallel}(r^*)$ resolved for the individual species supports this hypothesis. The smectic phase is randomly mixed and fully commensurate in spite of the different local ordering observed for the two molecular species. The $\langle S \rangle$ order parameter is consistently higher for the longer of the molecule types throughout the ordered phases. The difference is greatest in the nematic region and then decreases with decrease in temperature. The results demonstrate that the Generalised Gay-Berne intermolecular potential offers a computationally efficient potential, and appears, therefore, to be a viable route for studying multicomponent and polydisperse systems.

Chapter 5 aimed to achieve greater understanding of the effect of pressure and concentration of liquid crystal mixtures. The binary mixtures exhibit isotropic, nematic, smectic-A, *induced* smectic-A and smectic-B phases depending on the choice of pressure and concentration. Phase diagrams are presented for both studies.

In a binary mixture, the results presented in Chapter 5 indicate that the temperature range over which the nematic phase is stable can be extended by elevating the system pressure and/or by choice of concentration. The latter method is of significant technological importance since a nematic range can be obtained which is greater than that of the homogeneous system of either molecules thereby acquiring a property unobtainable in either pure system.

The smectic-A phase appears in both the $\langle T^* \rangle$ vs. $\langle P^* \rangle$ (section 5.2) and $\langle T^* \rangle$ vs. χ_A (section 5.3) phase diagrams. The $\chi_A = 1.0$ simulation (3.5:1 molecules) indicates the

CHAPTER 6. CONCLUSIONS AND FUTURE WORK

presence of a narrow stable *SmA* phase consistent with recent understanding that the *SmA* phase just becomes stable as the molecular elongation is greater or equal to 3.4:1 length to breadth ratio. This work advances current understanding by successfully demonstrating that a stable smectic-A *island* exists for $\chi_A = 0.50$ simulations depending on the choice of pressure. More intriguing is the existence of a narrow induced *SmA* phase at $\chi_A = 0.25$. The question of whether or not an induced smectic phase occurs in a nematic mixture can be considered via the temperature dependence of the coupling terms involving the cross-nematic and the cross-smectic order parameters. This is believed to be the first simulation to report an induced *SmA* phase in a binary mixture of liquid crystals.

6.2 Final Remarks and Future work

When considering the thesis as a whole it has been shown that a relatively simple model of liquid crystal mixtures can reveal a rich number of phases and properties unobtainable in either pure system. In terms of future work, two separate studies could be immediately performed. Firstly, changing the degree of length dispersity could yield interesting results. Future work could consider mixtures of non-nematic mesogens or non-nematic and smectic-A mesogens. Secondly, the use of different Generalised Gay-Berne exponents which do not favour the side-by-side configurations in comparison to the cross and tee configurations may have an profound effect on the smectic-A island and induced smectic-A phase reported in this study.

CHAPTER 6. CONCLUSIONS AND FUTURE WORK

There are also numerous modification which can be applied to the model. First of all, the absence of a temperature constraint of the ensemble resulted in van der Waals heating. Clearly, performing these studies within the constant-*NPT* ensemble would be beneficial in locating temperature transitions. Secondly, it is proposed that replacement of the current mechanical change in simulation volume with a stochastic volume change would hopefully aid movement through phase space.

References

- [1] EA Poe. *The Narrative of Arthur Gordon Pym*. Harper and Brothers, New York, 1838.
- [2] H Kelker. *Molecular Crystals and Liquid Crystals*, 21(1), 1973.
- [3] R Virchow. *Virchow's Archive*, 6:571, 1854.
- [4] O Lehmann. *Z. Physikal Chemie*, 4:462, 1889.
- [5] P Planer. *Liebigs Annals Chemie*, 118:513, 1861.
- [6] W Löbisch. *Ber dt Chem*, 5:513, 1872.
- [7] B Raymann. *Bull Soc Chim*, 47:898, 1887.
- [8] F Reinitzer. *Monatshefte Chemie*, 9:421, 1888.
- [9] G Friedel. *Ann Physique*, 18:273, 1922.
- [10] S Chandrasekhar. *Liquid Crystals*. Cambridge University Press, 2 edition, 1977.

REFERENCES

- [11] GR Luckhurst and GW Gray. *The Molecular Physics of Liquid Crystals*. Academic Press, London, 1979.
- [12] L Gattermann and A Ritschke. *Ber Duet Chem Ges*, 23:1738, 1890.
- [13] S Chandrasekhar et al. *Pramana*, 9:47, 1977.
- [14] HP Hinov. *Molecular Crystals and Liquid Crystals*, 13(6):221, 1986.
- [15] MP Allen and DJ Tildesley. *Computer Simulations of Liquids*. Clarendon Press, Oxford, 1993.
- [16] JG Gay and BJ Berne. *Journal of Chemical Physics*, 74(6):3316, 1981.
- [17] DJ Cleaver, CM Care, MP Allen, and MP Neal. *Physical Review E*, 54:559, 1996.
- [18] PE Cladis. *Physical Review Letters*, 35:48, 1975.
- [19] PE Cladis, RK Bogardus, WB Daniels, and GN Taylor. *Physical Review Letters*, 39:720, 1977.
- [20] G Sigaud, F Hardouin, MF Achard, and H Gasparoux, 1979.
- [21] LJ Yu and A Saupe. *Physical Review Letters*, 45:1000, 1980.
- [22] EP Raynes. *IEEE Transactions of Electronic Devices*, 26:1116, 1979.
- [23] B Sturgeon. *Phil. Transactions*, 309:231, 1983.
- [24] CS Oh. *Molecular Crystals and Liquid Crystals*, 42:1, 1977.

REFERENCES

- [25] H Gruler. *Z. Naturforsch*, 28a:474, 1973.
- [26] MJ Bradshaw and EP Raynes. *Molecular Crystals and Liquid Crystals*, 11:107, 1983.
- [27] MJ Bradshaw, EP Raynes, I Fedak, and AJ Leadbetter. *Journal de Physique (Paris)*, 45:157, 1984.
- [28] MJ Bradshaw and EP Raynes. *Molecular Crystals and Liquid Crystals*, 138:307, 1986.
- [29] BW van der Meer, F Postma, AJ Dekker, and WH de Jeu. *Molecular Physics*, 45:1227, 1982.
- [30] JE Lydon and CJ Coakley. *Journal de Physique*, 36(3), 1975.
- [31] R Shashidhar and BR Ratna. *Liquid Crystals*, 5(2):421, 1989.
- [32] VN Raja, R Shashidhar, BR Ratna, G Heppke, and Ch Bahr. *Physical Review A*, 37(1):303, 1988.
- [33] K Ema, G Nounesis, CW Garland, and R Shashidhar. *Physical Review A*, 39(5):2599, 1989.
- [34] G Nounesis, S Kumar, S Pfeiffer, R Shashidhar, and CW Garland. *Physical Review Letters*, 73(4):565, 1994.
- [35] F Hardouin, MF Achard, NH Tinh, and G Sigaud. *Molecular Crystals and Liquid Crystals Letters*, 3:7, 1986.
- [36] S Pfeiffer. PhD thesis, Technical University of Berlin, 1989.

REFERENCES

- [37] S Pfeiffer, G Heppke, and R Shashidha. *46(10):R6166*, 1992.
- [38] J Prost and J Toner. *Physical Review A*, 36:5008, 1987.
- [39] RP Sear and G Jackson. *Physical Review Letters*, 74(21):4261, 1995.
- [40] L Wu, CW Garland, and S Pfeiffer. *Physical Review A*, 46(2):973, 1992.
- [41] G Heppke, S Pfeiffer, A Ranft, and R Shashidha. *Molecular Crystals and Liquid Crystals*, 206:31, 1991.
- [42] G Heppke, H-S Kitzrow, D Ltzsche, and Ch Papenfub. *Liquid Crystals*, 8(3):407, 1990.
- [43] G Sigaud, HT Nguyen, MF Achard, and RJ Twieg. *Physical Review Letters*, 65(22):2796, 1990.
- [44] F Hardouin, AM Levelut, MF Achard, and G Sigaud. *Journal of Chemical Physics*, 80(53), 1983.
- [45] F Brochard, J Jouffroy, and P Levinson. *Journal de Physique (Paris)*, 45:1125, 1984.
- [46] RJ Baxter. *Exactly Solved Models in Statistical Mechanics*. Academic Press, London, 1982.
- [47] PG De Gennes and J Prost. *The Physics of Liquid Crystals*. Calendon Press, Oxford, 1994.
- [48] L Onsager. *Ann NY Acad Sci*, 51:627, 1949.

REFERENCES

- [49] B Tjipto-Margo and GT Evans. *Journal of Chemical Physics*, 93(6):4254, 1990.
- [50] W Maier and A Saupe. *Z. Naturforsch*, 13:564, 1958.
- [51] R Alben. *Journal of Chemical Physics*, 59:4299, 1973.
- [52] A Stroobants and HNW Lekkerkerker. *Physical Chemistry*, 88(16):3669, 1984.
- [53] P Palfy-Muhoray, JR de Bruyn, and DA Dunmur. *Journal of Chemical Physics*, 82(11):5294, 1985.
- [54] JM Goetz and GL Hoatson. *Liquid Crystals*, 17:31, 1994.
- [55] HNW Lekkerkerker, Ph Coulon, Van Der Haegen R, and R Deblieck. *Journal of Chemical Physics*, 80(7):3427, 1984.
- [56] T Odijk and HNW Lekkerkerker. *Physical Chemistry*, 89:2090, 1985.
- [57] GJ Vroege and HNW Lekkerkerker. *Physical Chemistry*, 97:3601, 1993.
- [58] TM Birshstein, BI Kolegov, and VA Pryamitsyn. *Vysokomol Soyed*, 30:348, 1988.
- [59] R van Roij and B Mulder. *Journal of Chemical Physics*, 105(24):11237, 1996.
- [60] B Mulder. *Physical Review A*, 35:3095, 1987.
- [61] TJ Sluckin. *Liquid Crystals*, 6(1):111, 1989.
- [62] R Hashim, GR Luckhurst, and S Romano. *Molecular Physics*, 53(6):1535, 1984.
- [63] R Hashim, GR Luckhurst, F Prata, and S Romano. *Liquid Crystals*, 15(3):283, 1993.

REFERENCES

- [64] R Hashim, GR Luckhurst, and S Romano. *Liquid Crystals*, 1(2):133, 1986.
- [65] RL Humphries, PG James, and GR Luckhurst. *Symposium of the Faraday Society*, 5:107, 1971.
- [66] A Stroobants. *Physical Review Letters*, 69(16):2388, 1992.
- [67] A Stroobants. *Journal of Physics: Condense Matter*, 6:A285, 1994.
- [68] WE Palke, JW Emsley, and DJ Tildesley. *Molecular Physics*, 82(1):177, 1994.
- [69] R Luckač and FJ Vesely. *Molecular Crystals and Liquid Crystals*, 262:533, 1995.
- [70] PJ Camp and MP Allen. *Physica A*, 229:410, 1996.
- [71] PJ Camp, MP Allen, PG Bolhuis, and D Frenkel. *Journal of Chemical Physics*, 106(22):9270, 1997.
- [72] PG Bolhuis. PhD thesis, FOM Institute for Atomic and Molecular Physics, 1996.
- [73] JA Barker. *Molecular Physics*, 21:187, 1971.
- [74] H Goldstein. *Classical Mechanics*. Addison-Wesley, 2nd edition, 1980.
- [75] L Verlet. *Physical Review*, 159:98, 1967.
- [76] GD Harp and BJ Berne. *Journal of Chemical Physics*, 49:1249, 1968.
- [77] GD Harp and BJ Berne. *Physical Review*, A2:975, 1970.
- [78] BJ Berne and GD Harp. *Advances in Chemical Physics*, 56:4213, 1970.

REFERENCES

- [79] JB Berne and P Pechukas. *Journal of Chemical Physics*, 56(8):4213, 1972.
- [80] K Singer. *Molecular Physics*, 33:1757, 1977.
- [81] HC Anderson. *Journal of Chemical Physics*, 72(4):2384, 1980.
- [82] JM Haile and HW Graben. *Journal of Chemical Physics*, 73(5):2412, 1980.
- [83] D Brown and JHR Clarke. *Molecular Physics*, 51(5):1243, 1984.
- [84] IS Gradshteyn and IM Ryzhik. *Tables of Integrals”, Series and Productions*. Academic Press, 1994.
- [85] GR Luckhurst, RA Stephens, and RW Phippen. *Liquid Crystals*, 8(4):451, 1990.
- [86] S-M Cui and ZY Chen. *Physical Review E*, 50:3747, 1994.
- [87] GJ Vroege and HNW Lekkerkerker. *Rep Prog Phys*, 55:1241, 1992.
- [88] R Hashim, GR Luckhurst, and S Romano. *Molecular Physics*, 56:1217, 1985.
- [89] D Frenkel. *Journal of Physics: Condence Matter*, 6:A71, 1994.
- [90] E De Miguel, LF Rull, MK Chalam, and KE Gubbins. *Molecular Physics*, 72(3):593, 1991.
- [91] SJ Mills and DJ Cleaver. Gibbs ensemble simulation of nematic-istropic coexistence in a liquid crystal mixture. *Physical Review E* (accepted).
- [92] R Hashim, GR Luckhurst, and S Romano. *Chem Soc Faraday Tran*, 19(4):214, 1995.

REFERENCES

- [93] MA Bates and GR Luckhurst. *Journal of Chemical Physics*, 110(14):7087, 1999.
- [94] JT Brown, MP Allen, E Martin del Rio, and E De Miguel. *Physical Review E*, 57(6):6685, 1998.
- [95] E De Miguel, LF Rull, MK Chalam, and KE Gubbins. *Molecular Physics*, 74(2):405, 1991.
- [96] MSS Challa, DP Landau, and K Binder. *Physical Review B*, 34(3):1841, 1986.
- [97] R Berardi, APJ Emerson, and C Zannoni. *J Chem Soc Faraday Trans*, 89:4069, 1993.
- [98] WL McMillan. *Physical Review A*, 4:1238, 1971.
- [99] A Zywocinski. *Physical Chemistry*, 103(16):3087, 1999.
- [100] BI Halperin, TC Lubensky, and SK Ma. *Physical Review Letters*, 32:292, 1974.
- [101] B Nandi, M Saha, and PK Mukherjee. *Modern Physics B*, 12(2):207, 1998.
- [102] PE Caldis. *Molecular Crystals and Liquid Crystals*, 67:177, 1981.
- [103] RJ Birgeneau, CW Garland, GB Kasting, and BM Ocko. *Physical Review A*, 24(5):2624, 1981.
- [104] C Chiang and CW Garland. *Molecular Crystals and Liquid Crystals*, 122(1-4):25, 1985.
- [105] ME Huster, KJ Stine, and CW Garland. *Physical Review A*, 36(5):2364, 1987.

REFERENCES

- [106] D Frenkel, HNW Lekkerkerker, and A Stroobants. *Nature*, 332(6167):822, 1988.
- [107] JAC Veerman and D Frenkel. *Physical Review A*, 45:5632, 1990.
- [108] SC McGrother, DC Williamson, and G Jackson. *Journal of Chemical Physics*, 104(17):6755, 1996.
- [109] P Bolhuis and D Frenkel. *Journal of Chemical Physics*, 106(2):666, 1997.
- [110] JM Polson and D Frenkel. *Physical Review E*, 56(6):R6260, 1997.
- [111] CY Chao, CF Chou, JT Ho, SW Hui, AJ Jin, and CC Huang. *Physical Review Letters*, 77(13):2750, 1996.
- [112] Giroud-Godquin AM and Billard J. *Molecular Crystals and Liquid Crystals*, 66:147, 1981.
- [113] R van Roij, B Mulder, and M Dijkstra. *Physica A*, 261(3-4):374, 1998.
- [114] R van Roij and B Mulder. *Physical Review E*, 54(6):6430, 1996.
- [115] M Dijkstra, R van Roij, and R Evans. *Physical Review Letters*, 81(11):2268, 1998.
- [116] RP Sear and Mulder BM. *Journal of Chemical Physics*, 105(17):7727, 1996.
- [117] RP Sear and G Jackson. *Molecular Physics*, 82(5):1033, 1994.
- [118] M Dijkstra and R van Roij. *Physical Review E*, 56(5B):5594, 1997.
- [119] FA Escobedo and JJ de Pablo. *Journal of Chemical Physics*, 106(23):9858, 1997.

REFERENCES

- [120] CJ Adkins. *Equilibrium Thermodynamics*. Cambridge University Press, Cambridge, 3rd edition, 1994.
- [121] SC McGrother, RP Sear, and G Jackson. *Journal of Chemical Physics*, 106(17):7315, 1997.
- [122] JC Hwang, H Kikuchi, and T Kajiyama. *Polymers*, 33(9):1822, 1992.
- [123] EP Sakolova. *Russian Journal of Applied Physics*, 67:798, 1994.
- [124] T Kyu, HW Chiu, and T Kajiyama. *Physical Review E*, 55(6):7105, 1997.
- [125] G Nounesis, CW Garland, and R Shashidhar. *Physical Review A*, 43(4):1849, 1991.

Appendix A

Appendix of Section 5.2 of Chapter 5

APPENDIX A. APPENDIX OF SECTION 5.2 OF CHAPTER 5

A.1 $\langle P^* \rangle = 1.0$

$\langle T^* \rangle$	$\langle S^{all} \rangle$	$\langle S^A \rangle$	$\langle S^B \rangle$	$\langle S^A \rangle - \langle S^B \rangle$	$\langle P^* \rangle$	$\langle \rho^* \rangle$	$\langle U^* \rangle$
2.09(06)	0.05(02)	0.07(02)	0.06(02)	0.007(028)	1.00(10)	0.157(003)	-1.94(05)
1.83(03)	0.06(02)	0.08(02)	0.07(02)	0.008(029)	1.00(08)	0.169(002)	-2.25(05)
1.63(03)	0.07(02)	0.09(03)	0.08(02)	0.010(035)	1.00(08)	0.181(002)	-2.60(05)
1.47(03)	0.12(04)	0.14(05)	0.11(03)	0.030(057)	1.00(08)	0.192(002)	-3.02(05)
1.39(03)	0.34(05)	0.38(05)	0.30(05)	0.088(071)	1.00(09)	0.202(002)	-3.56(06)
1.38(03)	0.59(03)	0.65(03)	0.53(04)	0.115(048)	1.00(09)	0.213(002)	-4.23(07)
1.35(03)	0.72(02)	0.76(02)	0.67(02)	0.090(029)	1.00(10)	0.223(002)	-4.85(06)
1.33(03)	0.80(01)	0.84(01)	0.76(02)	0.076(023)	1.00(10)	0.233(002)	-5.55(07)
1.31(03)	0.86(01)	0.89(01)	0.83(01)	0.058(017)	1.00(11)	0.242(002)	-6.26(07)
1.28(03)	0.89(01)	0.91(01)	0.87(01)	0.039(012)	1.00(11)	0.250(002)	-6.94(06)
1.31(03)	0.92(00)	0.94(00)	0.90(01)	0.030(008)	1.00(13)	0.260(002)	-7.77(07)
1.28(03)	0.94(00)	0.95(00)	0.93(01)	0.023(006)	1.00(13)	0.270(001)	-8.49(06)
1.22(03)	0.95(00)	0.96(00)	0.94(00)	0.018(005)	1.00(14)	0.279(002)	-9.07(06)
1.16(02)	0.96(00)	0.97(00)	0.96(00)	0.014(004)	1.00(15)	0.289(001)	-9.64(05)
1.06(02)	0.97(00)	0.98(00)	0.96(00)	0.013(003)	1.00(15)	0.296(001)	-10.13(05)

Table A.1: Molecular dynamics simulation results of GGB rods with axial ratios of 3.5:1 (molecules A) and 3:1 (molecules B) at mole fraction $\chi_A = 0.5$ and reduced pressure $\langle P^* \rangle = 1.0$. Columns key: $\langle T^* \rangle$ reduced temperature, $\langle S^{all} \rangle$ order parameter resolved over all molecules, $\langle S^A \rangle$ molecules' A order parameter, $\langle S^B \rangle$ molecules' B order parameter and $\langle S^A \rangle - \langle S^B \rangle$ order parameter difference. $\langle P^* \rangle$ reduced pressure (no long range correction), $\langle \rho^* \rangle$ reduced density and $\langle U^* \rangle$ reduced potential energy per molecule (no long range correction),

A.2 $\langle P^* \rangle = 2.0$

$\langle T^* \rangle$	$\langle S^{all} \rangle$	$\langle S^A \rangle$	$\langle S^B \rangle$	$\langle S^A \rangle - \langle S^B \rangle$	$\langle P^* \rangle$	$\langle \rho^* \rangle$	$\langle U^* \rangle$
2.36(05)	0.07(02)	0.08(02)	0.07(02)	0.010(033)	2.00(15)	0.192(002)	-2.28(06)
2.10(04)	0.08(02)	0.09(03)	0.08(02)	0.013(036)	1.99(14)	0.202(002)	-2.61(06)
1.85(03)	0.11(03)	0.13(04)	0.10(03)	0.028(049)	2.00(12)	0.213(001)	-3.01(06)
1.73(04)	0.30(08)	0.34(09)	0.27(08)	0.071(118)	2.00(12)	0.223(001)	-3.53(08)
1.70(04)	0.60(03)	0.65(03)	0.55(03)	0.098(044)	1.99(15)	0.232(002)	-4.23(07)
1.63(04)	0.71(02)	0.76(02)	0.67(03)	0.088(034)	1.99(15)	0.241(002)	-4.83(07)
1.55(03)	0.79(01)	0.83(01)	0.76(02)	0.064(022)	2.00(16)	0.250(002)	-5.45(07)
1.50(03)	0.85(01)	0.87(01)	0.82(01)	0.051(015)	2.00(14)	0.259(001)	-6.15(07)
1.46(03)	0.89(01)	0.91(01)	0.87(01)	0.034(011)	2.00(15)	0.265(001)	-6.90(07)
1.44(03)	0.91(00)	0.93(00)	0.90(01)	0.030(009)	2.00(16)	0.273(001)	-7.64(07)
1.48(03)	0.94(00)	0.95(00)	0.93(01)	0.021(006)	2.00(18)	0.283(001)	-8.47(07)
1.39(03)	0.95(00)	0.96(00)	0.94(00)	0.017(005)	2.00(18)	0.291(001)	-9.08(06)
1.29(03)	0.96(00)	0.97(00)	0.95(00)	0.015(004)	1.99(17)	0.299(001)	-9.62(06)
1.18(02)	0.97(00)	0.97(00)	0.96(00)	0.013(003)	2.00(17)	0.305(001)	-10.11(05)

Table A.2: Molecular dynamics simulation results of GGB rods with axial ratios of 3.5:1 (molecules *A*) and 3:1 (molecules *B*) at mole fraction $\chi_A = 0.5$ and reduced pressure $\langle P^* \rangle = 2.0$. Columns key: as of Table A.1

A.3 $\langle P^* \rangle = 3.0$

$\langle T^* \rangle$	$\langle S^{all} \rangle$	$\langle S^A \rangle$	$\langle S^B \rangle$	$\langle S^A \rangle - \langle S^B \rangle$	$\langle P^* \rangle$	$\langle \rho^* \rangle$	$\langle U^* \rangle$
2.26(04)	0.09(03)	0.11(03)	0.09(03)	0.018(042)	2.99(16)	0.223(001)	-2.75(07)
2.03(04)	0.19(05)	0.22(06)	0.17(05)	0.049(075)	3.00(17)	0.232(001)	-3.21(07)
1.98(04)	0.55(03)	0.60(03)	0.50(04)	0.101(049)	3.00(16)	0.242(001)	-3.97(08)
1.90(04)	0.70(02)	0.74(02)	0.66(03)	0.083(033)	3.00(18)	0.251(001)	-4.61(07)
1.78(04)	0.78(01)	0.81(01)	0.75(02)	0.066(023)	2.99(18)	0.260(001)	-5.24(07)
1.67(03)	0.83(01)	0.86(01)	0.81(01)	0.051(017)	2.99(18)	0.268(001)	-5.84(07)
1.61(03)	0.87(01)	0.89(01)	0.86(01)	0.037(013)	3.00(18)	0.275(001)	-6.55(08)
1.54(03)	0.90(01)	0.92(01)	0.89(01)	0.027(010)	2.99(18)	0.282(001)	-7.20(07)
1.56(04)	0.93(00)	0.94(00)	0.92(01)	0.021(007)	2.99(20)	0.292(001)	-8.31(08)
1.48(03)	0.94(00)	0.95(00)	0.93(01)	0.023(006)	2.99(20)	0.296(001)	-8.64(07)
1.37(03)	0.95(00)	0.96(00)	0.94(00)	0.019(005)	3.00(20)	0.303(001)	-9.21(06)
1.28(03)	0.96(00)	0.97(00)	0.95(00)	0.014(004)	2.99(19)	0.309(001)	-9.73(06)
1.18(02)	0.97(00)	0.97(00)	0.96(00)	0.011(003)	3.00(20)	0.314(001)	-10.18(05)

Table A.3: Molecular dynamics simulation results of GGB rods with axial ratios of 3.5:1 (molecules *A*) and 3:1 (molecules *B*) at mole fraction $\chi_A = 0.5$ and reduced pressure $\langle P^* \rangle = 3.0$. Columns key: as of Table A.1

A.4 $\langle P^* \rangle = 4.0$

$\langle T^* \rangle$	$\langle S^{all} \rangle$	$\langle S^A \rangle$	$\langle S^B \rangle$	$\langle S^A \rangle - \langle S^B \rangle$	$\langle P^* \rangle$	$\langle \rho^* \rangle$	$\langle U^* \rangle$
2.35(04)	0.13(03)	0.15(04)	0.12(03)	0.038(053)	4.00(19)	0.239(001)	-2.89(08)
2.26(05)	0.24(06)	0.27(07)	0.21(06)	0.060(092)	3.99(20)	0.243(001)	-3.16(09)
2.22(05)	0.42(06)	0.47(06)	0.38(06)	0.094(085)	3.99(20)	0.248(001)	-3.53(10)
2.20(04)	0.57(03)	0.62(03)	0.52(04)	0.102(048)	3.99(20)	0.252(001)	-3.94(09)
2.15(04)	0.66(02)	0.70(03)	0.61(03)	0.089(037)	3.99(20)	0.257(001)	-4.29(09)
2.08(04)	0.71(02)	0.75(02)	0.67(02)	0.081(032)	4.00(22)	0.261(001)	-4.60(09)
1.97(04)	0.78(01)	0.81(01)	0.75(02)	0.063(023)	3.99(21)	0.269(001)	-5.14(08)
1.87(04)	0.82(01)	0.84(01)	0.79(02)	0.052(019)	3.99(21)	0.274(001)	-5.53(08)
1.79(04)	0.85(01)	0.87(01)	0.82(01)	0.044(015)	3.99(21)	0.279(001)	-5.94(08)
1.73(04)	0.87(01)	0.89(01)	0.85(01)	0.038(013)	3.99(22)	0.284(001)	-6.39(09)
1.68(04)	0.89(01)	0.91(01)	0.88(01)	0.030(010)	3.99(22)	0.288(001)	-6.87(08)
1.63(04)	0.91(00)	0.92(01)	0.89(01)	0.026(009)	3.99(21)	0.292(001)	-7.34(08)
1.77(05)	0.93(00)	0.94(00)	0.92(01)	0.022(007)	3.99(24)	0.294(001)	-7.96(09)
1.73(04)	0.94(00)	0.95(00)	0.93(00)	0.019(006)	3.99(23)	0.300(001)	-8.46(07)
1.65(03)	0.95(00)	0.96(00)	0.94(00)	0.018(005)	3.99(24)	0.304(001)	-8.87(07)
1.56(03)	0.95(00)	0.96(00)	0.95(00)	0.015(005)	3.99(24)	0.309(001)	-9.24(07)

Table A.4: Molecular dynamics simulation results of GGB rods with axial ratios of 3.5:1 (molecules *A*) and 3:1 (molecules *B*) at mole fraction $\chi_A = 0.5$ and reduced pressure $\langle P^* \rangle = 4.0$. Columns key: as of Table A.1

A.5 $\langle P^* \rangle = 5.0$

$\langle T^* \rangle$	$\langle S^{all} \rangle$	$\langle S^A \rangle$	$\langle S^B \rangle$	$\langle S^A \rangle - \langle S^B \rangle$	$\langle P^* \rangle$	$\langle \rho^* \rangle$	$\langle U^* \rangle$
2.63(05)	0.12(04)	0.13(04)	0.11(03)	0.022(053)	4.99(22)	0.246(001)	-2.64(09)
2.54(05)	0.15(05)	0.17(06)	0.13(04)	0.040(072)	4.99(23)	0.249(001)	-2.80(09)
2.46(05)	0.22(07)	0.24(08)	0.19(06)	0.050(100)	4.99(23)	0.252(001)	-2.99(10)
2.46(05)	0.43(05)	0.47(06)	0.38(05)	0.090(077)	4.99(22)	0.255(001)	-3.34(10)
2.44(05)	0.54(03)	0.59(03)	0.50(03)	0.090(046)	4.98(24)	0.258(002)	-3.66(10)
2.40(05)	0.61(03)	0.66(03)	0.57(03)	0.092(043)	4.99(25)	0.261(002)	-3.93(09)
2.35(05)	0.65(02)	0.70(02)	0.61(03)	0.085(038)	4.99(23)	0.264(001)	-4.16(09)
2.31(04)	0.70(02)	0.74(02)	0.66(02)	0.084(030)	4.99(24)	0.267(001)	-4.41(09)
2.26(05)	0.73(02)	0.77(02)	0.70(02)	0.070(029)	4.99(24)	0.270(001)	-4.62(09)
2.20(05)	0.76(01)	0.79(02)	0.73(02)	0.066(025)	4.99(25)	0.273(001)	-4.83(09)
2.15(04)	0.78(01)	0.81(01)	0.75(02)	0.059(023)	4.98(25)	0.276(001)	-5.03(08)
2.09(04)	0.80(01)	0.83(01)	0.77(01)	0.054(019)	4.98(24)	0.279(001)	-5.22(08)
2.04(04)	0.82(01)	0.84(01)	0.79(01)	0.050(019)	4.99(24)	0.281(001)	-5.40(08)
1.99(04)	0.83(01)	0.85(01)	0.81(01)	0.049(017)	4.99(24)	0.284(001)	-5.58(08)
1.93(04)	0.84(01)	0.86(01)	0.82(01)	0.043(016)	4.99(25)	0.286(001)	-5.77(08)
1.85(04)	0.87(01)	0.89(01)	0.85(01)	0.038(014)	4.99(24)	0.291(001)	-6.19(09)
1.80(04)	0.89(01)	0.90(01)	0.87(01)	0.031(011)	4.99(24)	0.295(001)	-6.66(09)
1.80(06)	0.91(01)	0.92(01)	0.90(01)	0.025(010)	4.99(24)	0.298(001)	-7.31(14)
1.90(04)	0.93(00)	0.94(00)	0.92(01)	0.020(007)	4.98(26)	0.303(001)	-8.17(08)
1.92(05)	0.93(00)	0.94(00)	0.92(01)	0.020(007)	4.99(25)	0.301(001)	-7.91(10)
1.81(04)	0.94(00)	0.95(00)	0.93(00)	0.018(006)	4.99(26)	0.308(001)	-8.56(08)
1.71(03)	0.95(00)	0.96(00)	0.94(00)	0.016(005)	4.99(27)	0.312(001)	-8.95(07)
1.62(03)	0.96(00)	0.96(00)	0.95(00)	0.015(004)	4.99(27)	0.316(001)	-9.30(07)

Table A.5: Molecular dynamics simulation results of GGB rods with axial ratios of 3.5:1 (molecules *A*) and 3:1 (molecules *B*) at mole fraction $\chi_A = 0.5$ and reduced pressure $\langle P^* \rangle = 5.0$. Columns key: as of Table A.1

Appendix B

Appendix of Section 5.3 of

Chapter 5

B.1 $\chi_A = 0.0$

$\langle T^* \rangle$	$\langle S^{all} \rangle$	$\langle S^A \rangle$	$\langle S^B \rangle$	$\langle P^* \rangle$	$\langle \rho^* \rangle$	$\langle U^* \rangle$
2.80(05)	0.06(02)	0.00(00)	0.06(02)	4.99(24)	0.256(002)	-1.92(08)
2.44(04)	0.08(02)	0.00(00)	0.08(02)	4.99(22)	0.266(001)	-2.24(07)
2.16(04)	0.09(03)	0.00(00)	0.09(03)	4.99(22)	0.275(001)	-2.55(07)
1.96(04)	0.40(06)	0.00(00)	0.40(06)	4.99(21)	0.287(001)	-3.22(09)
1.93(04)	0.60(03)	0.00(00)	0.60(03)	4.99(23)	0.293(001)	-3.72(08)
1.83(04)	0.73(02)	0.00(00)	0.73(02)	4.99(24)	0.302(001)	-4.30(07)
1.69(03)	0.80(01)	0.00(00)	0.80(01)	4.99(23)	0.310(001)	-4.80(07)
1.56(03)	0.84(01)	0.00(00)	0.84(01)	5.00(23)	0.318(001)	-5.28(07)
1.48(03)	0.88(01)	0.00(00)	0.88(01)	4.99(24)	0.325(001)	-5.87(08)
1.48(04)	0.89(01)	0.00(00)	0.89(01)	5.00(23)	0.327(001)	-6.18(09)
1.62(03)	0.92(00)	0.00(00)	0.92(00)	4.99(25)	0.332(001)	-6.93(07)
1.50(03)	0.94(00)	0.00(00)	0.94(00)	4.99(25)	0.339(001)	-7.45(06)
1.38(03)	0.95(00)	0.00(00)	0.95(00)	4.99(25)	0.345(001)	-7.90(06)

Table B.1: Molecular dynamics simulation results of GGB rods with axial ratios of 3.5:1 (molecules *A*) and 3:1 (molecules *B*) at mole fraction $\chi_A = 0.0$ and reduced pressure $\langle P^* \rangle = 5.0$. Columns key: $\langle T^* \rangle$ reduced temperature, $\langle S^{all} \rangle$ order parameter resolved over all molecules, $\langle S^A \rangle$ molecules' *A* order parameter, $\langle S^B \rangle$ molecules' *B* order parameter and $\langle S^A \rangle - \langle S^B \rangle$ order parameter difference. $\langle P^* \rangle$ reduced pressure (no long range correction), $\langle \rho^* \rangle$ reduced density and $\langle U^* \rangle$ reduced potential energy per molecule (no long range correction),

B.2 $\chi_A = 0.25$

$\langle T^* \rangle$	$\langle S^{all} \rangle$	$\langle S^A \rangle$	$\langle S^B \rangle$	$\langle P^* \rangle$	$\langle \rho^* \rangle$	$\langle U^* \rangle$
3.04(05)	0.06(02)	0.10(03)	0.07(02)	4.99(25)	0.242(002)	-1.94(09)
2.66(05)	0.08(02)	0.11(03)	0.08(02)	4.99(24)	0.252(001)	-2.28(08)
2.36(04)	0.11(03)	0.15(04)	0.11(03)	4.99(22)	0.261(001)	-2.64(08)
2.19(05)	0.36(07)	0.42(08)	0.34(07)	4.99(23)	0.270(001)	-3.21(11)
2.13(04)	0.64(03)	0.71(03)	0.62(03)	4.99(23)	0.278(001)	-3.98(09)
2.00(04)	0.74(02)	0.79(02)	0.73(02)	4.99(23)	0.287(001)	-4.56(08)
1.87(04)	0.80(01)	0.84(01)	0.79(01)	4.99(23)	0.295(001)	-5.06(07)
1.73(03)	0.84(01)	0.88(01)	0.83(01)	5.00(24)	0.302(001)	-5.57(07)
1.63(04)	0.88(01)	0.90(01)	0.87(01)	4.99(23)	0.309(001)	-6.16(09)
1.58(03)	0.90(01)	0.92(01)	0.89(01)	4.99(23)	0.312(001)	-6.61(08)
1.69(04)	0.92(00)	0.94(01)	0.92(00)	4.99(26)	0.317(001)	-7.43(08)
1.62(03)	0.93(00)	0.95(01)	0.93(00)	4.99(26)	0.321(001)	-7.82(07)
1.53(03)	0.94(00)	0.96(00)	0.94(00)	4.99(25)	0.325(001)	-8.16(07)
1.45(03)	0.95(00)	0.96(00)	0.95(00)	4.99(24)	0.329(001)	-8.46(06)
1.35(03)	0.95(01)	0.96(01)	0.95(01)	4.98(27)	0.331(003)	-8.70(11)

Table B.2: Molecular dynamics simulation results of GGB rods with axial ratios of 3.5:1 (molecules *A*) and 3:1 (molecules *B*) at mole fraction $\chi_A = 0.25$ and reduced pressure $\langle P^* \rangle = 5.0$. Columns key: as Table B.1

APPENDIX B. APPENDIX OF SECTION 5.3 OF CHAPTER 5

B.3 $\chi_A = 0.5$

Please refer to Table A.5 of Appendix A

B.4 $\chi_A = 0.75$

$\langle T^* \rangle$	$\langle S^{all} \rangle$	$\langle S^A \rangle$	$\langle S^B \rangle$	$\langle P^* \rangle$	$\langle \rho^* \rangle$	$\langle U^* \rangle$
4.17(08)	0.06(02)	0.07(02)	0.08(03)	4.98(28)	0.206(002)	-1.56(11)
3.47(06)	0.07(02)	0.08(02)	0.09(03)	4.98(25)	0.219(001)	-2.04(10)
2.95(05)	0.11(03)	0.12(04)	0.11(03)	4.99(24)	0.231(001)	-2.56(10)
2.79(05)	0.15(05)	0.16(05)	0.14(04)	4.99(23)	0.235(001)	-2.81(10)
2.70(06)	0.27(09)	0.29(09)	0.24(07)	4.98(23)	0.239(001)	-3.11(12)
2.71(06)	0.34(07)	0.36(08)	0.29(07)	4.99(23)	0.240(001)	-3.23(13)
2.68(06)	0.54(04)	0.57(04)	0.47(05)	5.00(24)	0.245(001)	-3.75(11)
2.64(06)	0.62(03)	0.64(03)	0.55(04)	4.99(24)	0.248(001)	-4.05(11)
2.62(05)	0.66(02)	0.68(02)	0.59(04)	5.00(24)	0.250(001)	-4.22(10)
2.54(05)	0.72(02)	0.74(02)	0.66(03)	4.98(24)	0.254(001)	-4.61(09)
2.49(05)	0.74(02)	0.76(02)	0.68(03)	4.99(24)	0.256(001)	-4.77(09)
2.44(05)	0.76(02)	0.78(02)	0.71(03)	4.99(24)	0.259(001)	-4.95(09)
2.31(04)	0.80(01)	0.82(01)	0.76(02)	4.98(24)	0.265(001)	-5.42(09)
2.14(04)	0.85(01)	0.86(01)	0.82(02)	4.99(24)	0.272(001)	-6.07(09)
2.03(04)	0.89(01)	0.90(01)	0.86(01)	4.98(25)	0.279(001)	-6.85(11)
2.01(06)	0.92(01)	0.92(00)	0.90(01)	4.99(25)	0.284(001)	-7.82(15)
2.11(05)	0.94(00)	0.94(00)	0.92(01)	4.98(26)	0.289(001)	-8.67(11)
2.03(04)	0.95(00)	0.95(00)	0.93(01)	4.98(27)	0.294(001)	-9.21(09)
1.93(04)	0.95(00)	0.96(00)	0.94(00)	4.99(26)	0.298(001)	-9.62(08)
1.83(04)	0.96(00)	0.96(00)	0.95(00)	4.99(27)	0.302(001)	-10.01(08)
1.71(03)	0.96(00)	0.97(00)	0.95(01)	4.98(28)	0.305(002)	-10.39(09)

Table B.3: Molecular dynamics simulation results of GGB rods with axial ratios of 3.5:1 (molecules A) and 3:1 (molecules B) at mole fraction $\chi_A = 0.75$ and reduced pressure $\langle P^* \rangle = 5.0$. Columns key: as Table B.1

APPENDIX B. APPENDIX OF SECTION 5.3 OF CHAPTER 5

B.5 $\chi_A = 1.0$

$\langle T^* \rangle$	$\langle S^{all} \rangle$	$\langle S^A \rangle$	$\langle S^B \rangle$	$\langle P^* \rangle$	$\langle \rho^* \rangle$	$\langle U^* \rangle$
3.15(06)	0.08(03)	0.08(03)	0.00(00)	4.99(26)	0.214(001)	-2.08(10)
2.79(05)	0.14(04)	0.14(04)	0.00(00)	4.98(23)	0.223(001)	-2.51(09)
2.71(05)	0.20(06)	0.20(06)	0.00(00)	4.99(24)	0.226(001)	-2.70(10)
2.70(06)	0.53(04)	0.53(04)	0.00(00)	5.00(24)	0.231(001)	-3.37(11)
2.58(05)	0.71(02)	0.71(02)	0.00(00)	4.99(25)	0.240(001)	-4.17(10)
2.40(05)	0.79(01)	0.79(01)	0.00(00)	4.99(25)	0.249(001)	-4.85(09)
2.22(04)	0.84(01)	0.84(01)	0.00(00)	4.98(26)	0.257(001)	-5.50(09)
2.10(05)	0.88(01)	0.88(01)	0.00(00)	4.99(26)	0.264(001)	-6.24(10)
2.03(04)	0.91(01)	0.91(01)	0.00(00)	4.99(26)	0.269(001)	-7.01(10)
2.02(05)	0.93(00)	0.93(00)	0.00(00)	4.99(26)	0.275(001)	-8.03(11)
2.05(04)	0.95(00)	0.95(00)	0.00(00)	4.99(26)	0.280(001)	-8.76(09)
1.96(04)	0.96(00)	0.96(00)	0.00(00)	4.98(27)	0.284(001)	-9.23(08)
1.85(04)	0.96(00)	0.96(00)	0.00(00)	4.98(28)	0.289(001)	-9.65(08)
1.75(03)	0.97(00)	0.97(00)	0.00(00)	4.98(28)	0.292(001)	-10.03(07)

Table B.4: Molecular dynamics simulation results of GGB rods with axial ratios of 3.5:1 (molecules *A*) and 3:1 (molecules *B*) at mole fraction $\chi_A = 1.0$ and reduced pressure $\langle P^* \rangle = 5.0$. Columns key: as Table B.1